INFORMATION TO USERS

This was produced from a copy of a document sent to us for microfilming. While the most advanced technological means to photograph and reproduce this document have been used, the quality is heavily dependent upon the quality of the material submitted.

The following explanation of techniques is provided to help you understand markings or notations which may appear on this reproduction.

1. The sign or "target" for pages apparently lacking from the document photographed is "Missing Page(s)". If it was possible to obtain the missing page(s) or section, they are spliced into the film along with adjacent pages. This may have necessitated cutting through an image and duplicating adjacent pages to assure you of complete continuity.

2. When an image on the film is obliterated with a round black mark it is an indication that the film inspector noticed either blurred copy because of movement during exposure, or duplicate copy. Unless we meant to delete copyrighted materials that should not have been filmed, you will find a good image of the page in the adjacent frame.

3. When a map, drawing or chart, etc., is part of the material being photographed the photographer has followed a definite method in "sectioning" the material. It is customary to begin filming at the upper left hand corner of a large sheet and to continue from left to right in equal sections with small overlaps. If necessary, sectioning is continued again—beginning below the first row and continuing on until complete.

4. For any illustrations that cannot be reproduced satisfactorily by xerography, photographic prints can be purchased at additional cost and tipped into your xerographic copy. Requests can be made to our Dissertations Customer Services Department.

5. Some pages in any document may have indistinct print. In all cases we have filmed the best available copy.

8106060

STEENHOEK, LARRY EUGENE

NEW TECHNIQUES IN ATOMIC AND MOLECULAR LASER SPECTROSCOPY

Iowa State University   PH.D.   1980

University
Microfilms
International 300 N. Zeeb Road, Ann Arbor, MI 48106

PLEASE NOTE:

In all cases this material has been filmed in the best possible way from the available copy. Problems encountered with this document have been identified here with a check mark ✓.

1. Glossy photographs _____

2. Colored illustrations _____

3. Photographs with dark background _____

4. Illustrations are poor copy _____

5. Print shows through as there is text on both sides of page _____

6. Indistinct, broken or small print on several pages _____

7. Tightly bound copy with print lost in spine _____

8. Computer printout pages with indistinct print ___✓___

9. Page(s) _____ lacking when material received, and not available from school or author

10. Page(s) _____ seem to be missing in numbering only as text follows

11. Poor carbon copy _____

12. Not original copy, several pages with blurred type _____

13. Appendix pages are poor copy _____

14. Original copy with light type _____

15. Curling and wrinkled pages _____

16. Other _____

New techniques in atomic and molecular

laser spectroscopy

by

Larry Eugene Steenhoek

A Dissertation Submitted to the

Graduate Faculty in Partial Fulfillment of the

Requirements for the Degree of

DOCTOR OF PHILOSOPHY

Department: Chemistry
Major: Analytical Chemistry

Approved:

In Charge of Major Work

For the Major Department

For the Graduate College

Iowa State University
Ames, Iowa

1980

TABLE OF CONTENTS

PREFACE

Over the last two decades, there has been tremendous development in the field of laser technology leading to major advances in the fields of atomic and molecular spectroscopy. This is evidenced by the large number of books and review papers that have been written to document this development.

The laser as a light source has been a boon to the spectroscopist for at least three different reasons. The first of these is the increase in resolution attainable in conventional spectroscopy. The laser presents itself as a more powerful source of monochromatic light than conventional light sources and monochromators. The second reason that the laser has shown itself to be such a powerful spectroscopic tool is that laser light can be generated in extremely short pulses which enables one to study very rapid transient states. Finally, the laser has facilitated the development of a series of spectroscopic methods which include transition schemes that can be probed because of the high power that the laser presents.

The main goal of the research presented in this dissertation is the development of new laser-based spectroscopic techniques which utilize some of these valuable properties. This dissertation is divided into two parts which reflect the two basic areas of my research. Part I describes the development of a number of new nonlinear spectroscopic techniques. The techniques described include examples of two- and three-photon absorption as well as inverse Raman spectroscopy. Part II is devoted to

a study of spatial mapping of spectral sources. This work couples the use of a laser with digital-image processing technology. Described will be examples which include the mapping of atomic and molecular species in flames as well as atomic species in laser-generated vapor plumes.

PART I. NEW TECHNIQUES IN NONLINEAR SPECTROSCOPY

INTRODUCTION TO NONLINEAR SPECTROSCOPY

The advent of the laser as a light source has led to the development of new spectroscopic techniques based on transition schemes that can be probed due to the high power of the laser. Under low light level conditions, light and matter interact with each other in a linear fashion. As the light level increases, however, nonlinearities which result from the simultaneous interaction of the medium with more than one photon from the incident field(s) become significant. These nonlinearities arise because of the nonlinear terms of the electric susceptibility expansion.

Shen [1] has divided the development of nonlinear optics into three periods. During the first period (1961-1965), new nonlinear techniques were being discovered at a rapid rate. Some new nonlinear techniques were still being discovered during the second period (1965-1969), but the emphasis was on better understanding these phenomenon. The third period (post 1969) represents the maturity of nonlinear optics. During this time period, the main emphasis has been on the use of nonlinear techniques rather than on the discovery of new nonlinear phenomenon.

There are a number of good reviews on nonlinear spectroscopy [1,2, 3,4] which go into more detail than is warranted here. More details will be given about the specific techniques presented in this dissertation as they are discussed in later sections.

As will be shown, much information can be gained about atomic and molecular systems from the spectroscopy of their nonlinear behavior. Many atomic and molecular states that are difficult to probe with conventional

linear spectroscopy because of weak interaction with the field due to a series of selection rules can be probed with nonlinear techniques. In addition, ultraviolet and infrared transitions may be probed using readily available tunable visible lasers, thus eliminating some of the practical problems of doing spectroscopy in these regions.

DOPPLER-FREE TWO-PHOTON SPECTROSCOPY OF NAPHTHALENE

Theory and Review of Related Work

Two-photon theory was originally developed by Goeppert-Mayer (5) in 1931. It was not until 1961, however, that this effect was experimentally verified by Kaiser and Garrett (6) who observed blue fluorescence from Eu^{2+} impurities in CaF_2 crystals when irradiated with light at 694.3 nm from a ruby laser. The only mechanism by which this phenomenon could be explained was two-photon absorption (TPA). TPA is usually described in terms of second order pertubation theory, however for our purposes a simple quantum explanation will suffice. Suppose that two photon fields at frequencies ω_1 and ω_2 are incident upon a medium. Either of these two fields alone will produce only small nonresonant oscillations in the medium. If, however, the photon fields are present simultaneously, they can induce oscillations in the medium which are described by the sum or difference of their frequencies. If $\omega_1 + \omega_2$ is at resonance with the medium then the resultant oscillation may result in the absorption of both photons, leaving the atom (molecule) in a different quantum level. The TPA process operates by selection rules which are different from those governing one-photon processes. Quantum theory states that for a one-photon transition to be allowed from an initial state (o) to a final state (f) that the integral

$$M = \int \psi_f^* (r) \, \psi_0 \, d\tau \qquad (1)$$

must not vanish. Considering the symmetry of the operator (r) and the molecular state involved, for centrosymmetric molecules only transitions between states of opposite parity are allowed. If the same treatment is applied for a two-photon transition, the opposite selection rule is obtained and only transitions between states of equal parity are allowed (7). If a molecule has no center of symmetry, then the transition may be both one and two-photon allowed.

The two-photon absorption strength δ is expressed as:

$$- P_1 = - P_2 = P_1 P_2 \delta C \ell A^{-1} \qquad (2)$$

where P_1 and P_2 are the optical powers at ω_1 and ω_2, respectively, expressed in photons sec^{-1}. C is the sample concentration in molecules cm^{-3}, ℓ is the path length in cm, and A is the beam area in cm^2 (8). Typical values for δ are on the order of 10^{-50} cm^4 sec $photon^{-1}$ $molecule^{-1}$. One can see from this that the TPA effect is quadratically dependent on laser power and the small values for δ indicate that TPA is indeed a very weak effect. Low absorption levels make TPA difficult to measure directly. Other more sensitive techniques are therefore used to detect the occurrence of TPA. Some of these include fluorescence (9), thermal lensing (10), photoacoustics (11), two-photon ionization (12,13), and optogalvanic spectroscopy (14).

Since its somewhat slow beginnings, TPA has been more fully developed and applied to solid, liquid, and vapor phase samples. TPA is the topic of a number of good review articles to which the reader is referred for a more rigorous treatment of two-photon theory and for the details of its development (7,15,16). The rest of this chapter will deal

with one of the more recent developments in TPA, Doppler-free two-photon absorption (DFTPA).

The width of a spectral line is determined by three main contributors: the natural linewidth, pressure broadening, and Doppler broadening. The natural linewidth is limited by the spontaneous emission lifetime of the excited state and has a corresponding half-width on the order of 10^{-5} cm^{-1} in the visible region. Pressure broadening arises from binary collisions which terminate the life of an excited state. At atmospheric pressure this broadening mechanism accounts for a half-width of approximately 10^{-2} cm^{-1}. This undesirable limit on resolution can easily be eliminated by making the spectroscopic measurement at low pressures. The final contributor to the measured linewidth is Doppler broadening. Doppler broadening results from the relative motion of the molecule with respect to the radiation field. Typical Doppler half-widths are on the order of 10^{-2} cm^{-1}. In this case it can be seen that no matter how monochromatic the light source is, Doppler broadening will limit the resolution of the spectra to about 10^{-2} cm^{-1}. For high resolution work, this limit is not acceptable.

A series of spectroscopic techniques have been developed which are capable of probing inside the Doppler width of a transition. These include saturation spectroscopy (17,18), Doppler-free two-photon spectroscopy (19,20,21), optical double resonance (22), optical Ramsey fringes (23,24), polarization spectroscopy (25), polarization labeling (26), and coherent four-wave mixing (27). Each of these techniques has its own advantages and disadvantages.

The application of TPA in Doppler-free spectroscopy was suggested by Vasilenko et al. (28), Roberts and Fortson (29), and Kelley et al. (30). The theory of this experimental technique can be easily explained with the aid of Figure 1a. Consider an atom (molecule) in a standing photon field. This atom is moving at velocity v. In the rest frame of the atom, the apparent frequencies of the photons traveling in opposite directions become $\omega_1(1\pm v_x/C)$, where C is the speed of light. For a two-photon process between energy levels with a separation of ΔE, if both photons are absorbed traveling in the same direction, resonance will occur when:

$$\Delta E = 2\hbar\omega_1(1\pm v_x/C) \qquad (3)$$

This expression is clearly velocity dependent and only a small fraction of the molecules will be in resonance. If, however, one photon is absorbed from each of the two counterpropagating photon fields, then the two-photon resonance condition is described by:

$$\Delta E/\hbar = 2\omega_1 = \omega_0 \qquad (4)$$

Equation 4 is velocity independent and all atoms are at resonance. As one scans the region around 1/2 ω_0, one will trace out the usual broad Doppler profile. This signal will be very weak due to the fact that so few atoms are in resonance. As one scans through 1/2 ω_0, however, all atoms are at resonance and a high intensity profile of the natural lineshape is obtained. This idea is shown schematically in Figure 1b.

The first experimental observations of DFTPA were made simu-taneously by several groups. Baraben et al. (31) and Levenson and Bloembergen (32) observed 3S-5S DFTPA in sodium vapor using pulsed dye

Figure 1. Doppler-free two-photon absorption

        a. Molecular velocity diagram

        b. TPA signal as a function of laser frequency

TPA SIGNAL

$\Delta E/\hbar = \omega_0$

$2\omega_1$

b.

a.

ω_1

V_y

V

V_x

ω_1

Y

Z

X
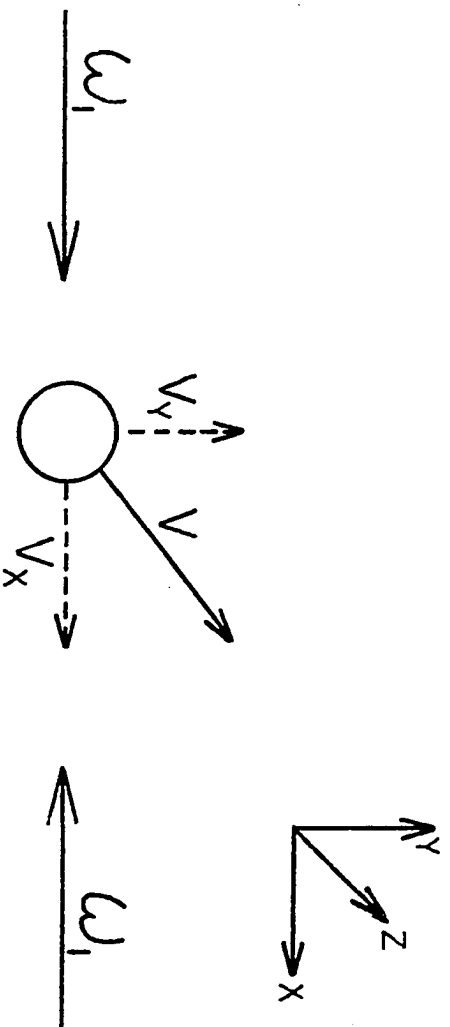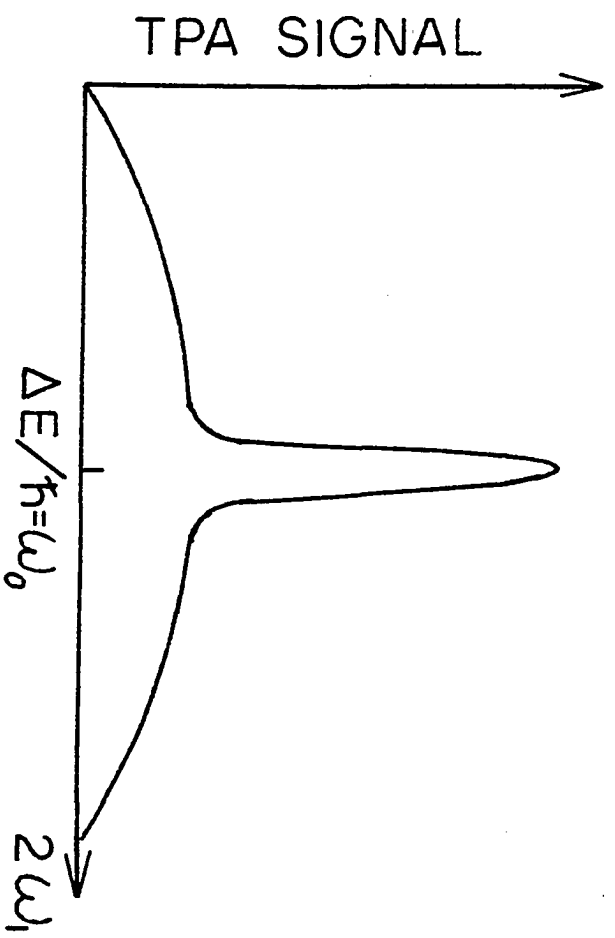
lasers. Hänsch et al. (33) observed 3S-4D DFTPA in sodium vapor using a continuous wave (cw) single frequency dye laser. Later DFTPA studies of atomic systems include: Bjorkholm and Liao (34) who studied resonance-enhanced DFTPA in sodium vapor, Flusberg et al. (35) who measured hyperfine splitting in thallium, Hänsch et al. (36) who observed DFTPA in hydrogen, and Kowalski et al. (37) who measured hyperfine splitting in lithium. A good review of DFTPA in atomic systems is given by Bloembergen and Levenson (38).

Oscillator strengths of atomic systems are distributed unevenly in a few levels and the fluorescence quantum yields in these systems are close to one. The distribution of oscillator strengths among numerous rovibronic levels and low-fluorescence quantum yields (due to radiationless decay) in molecular systems are not so favorable for two-photon studies.

The first DFTPA studies on molecular systems were done by Bischel et al. (39,40) who studied CH_3F and NH_3 in the infrared region. Woerdman (41) has reported DFTPA in Na_2, Gelbwachs et al. (42) in nitric oxide and benzene, and Bernheim et al. in CO (43). Of the many TPA studies done on vapor phase molecular systems, most have enjoyed high peak power-pulsed lasers. It has been shown in atomic TPA studies, however, that only when one uses a cw single-frequency dye laser that the ultimate resolution can be obtained.

Since molecular systems are more difficult to study by TPA than are atomic systems, the power available from a cw single frequency laser will most likely be inadequate to generate any significant TPA signal. One

way in which this power can be significantly increased is by moving the sample cell inside the laser cavity where the available power is on the order of one hundred times greater than the available extracavity power. Since TPA is a function of power squared, this gain in power should correspond to a 10^4 increase in TPA signal. If the sample exhibits very weak absorption, its presence should not introduce any loss of laser gain and corresponding drop in laser power. In addition, by placing the cell inside the laser cavity, the colinearity of the counterpropagating beams is guaranteed by lasing.

The use of intracavity absorption has been developed independently by two groups (44,45) in an attempt to better the resolution attainable with pulsed laser systems. This chapter reports our work in the development of this technique as it is demonstrated with the DFTPA spectrum of naphthalene. Gelbwachs and Wessel (42) using a system similar to the one described here have obtained DFTPA spectra of nitric oxide and benzene.

<center>Experimental</center>

The heart of our Doppler-free two-photon spectrometer was a Spectra-Physics Model 580-A electronically tunable single-frequency dye laser with a passive stability of 50 MHz. The dye laser was pumped by a Control Laser Model 553A Ar^+ laser operating at 6 W all lines. The dye laser was modified in order to accommodate the intracavity gas cell. This was done by removing the front mirror from the faceplate of the dye laser and mounting it on a movable Gimbal mount in front of the dye

laser. In addition, the normal front mirror of the dye laser was replaced with a highly reflecting mirror (99.9%) in order to increase the effective power.

The aluminum gas cell shown in Figure 2 had two 11 mm diameter, 15 mm focal length, anti-reflection coated lenses as windows. A 4 cm diameter, f/1 fused silica collection lens was mounted perpendicular to the two focusing lenses. The beam waist inside the gas cell was estimated to be 8 μm. The gas cell could be evacuated to 1×10^{-6} torr. For alignment purposes, the gas cell was mounted on an X-Y translational stage and a Gimbal mount.

To obtain optimum power and mode structure, the gas cell was placed inside the focused fluorescence spot formed by the rear concave mirror of the dye laser. The position of the front mirror relative to the gas cell was found to be quite critical and was optimized by monitoring the output power of the dye laser. Once the laser was tuned to lase, the gas cell and laser mirrors were carefully aligned to give a TEM_{00} mode laser output. If the laser output had higher axial modes, the fluorescence signal was reduced by one or two orders of magnitude. This is due to the poor focusing properties of higher-order laser beams.

A schematic diagram of the experimental apparatus is shown in Figure 3. To monitor the power, wavelength, and mode structure of the laser, the output beam was split into a thermopile, a Bausch and Lomb 1/4 m double monochromator, and a Spectra-Physics Model 470 spectrum analyzer with an 8 GHz free-spectral range. In single mode operation using the standard scanning electronics of the 580A system, we were
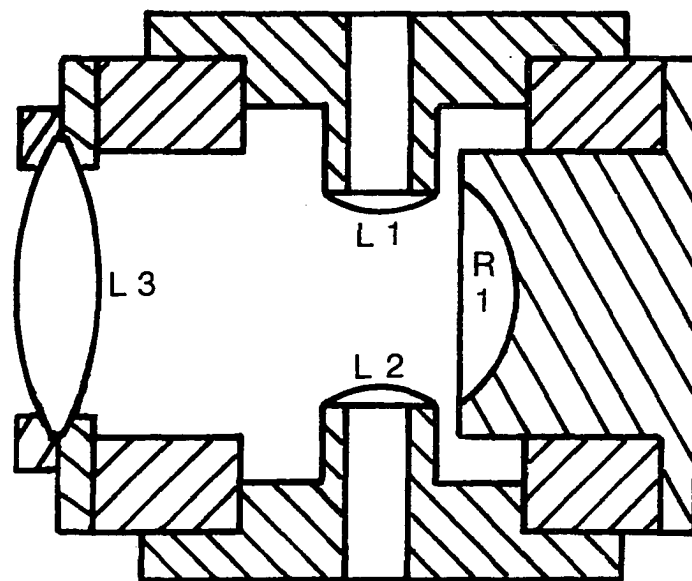
Figure 2. Aluminum gas cell (cross section). L1 and L2 are focusing lenses, L3 is the fluorescence collection lens, and R1 is a concave aluminum mirror

Figure 3. Experimental arrangement of a cw intracavity two-photon
absorption laser system

TO PZT ETALON

X-Y
RECORDER

PZ SCANNING
RAMP GENERATOR

D-A
CONVERTER

H.V.

AMP &
DISCRIMINATOR

COUNTER

PMT

FILTER

FROM Ar⁺ LASER

BEAM
SPLITTER

TUNING
WEDGE

DYE STREAM

TO POWER
METER or
SPECTROMETER

PZT
MIRROR

GAS
CELL

ETALON

PZT
ETALON

RAMP GENERATOR

OSCILLOSCOPE

CONFOCAL
FABRY-PEROT
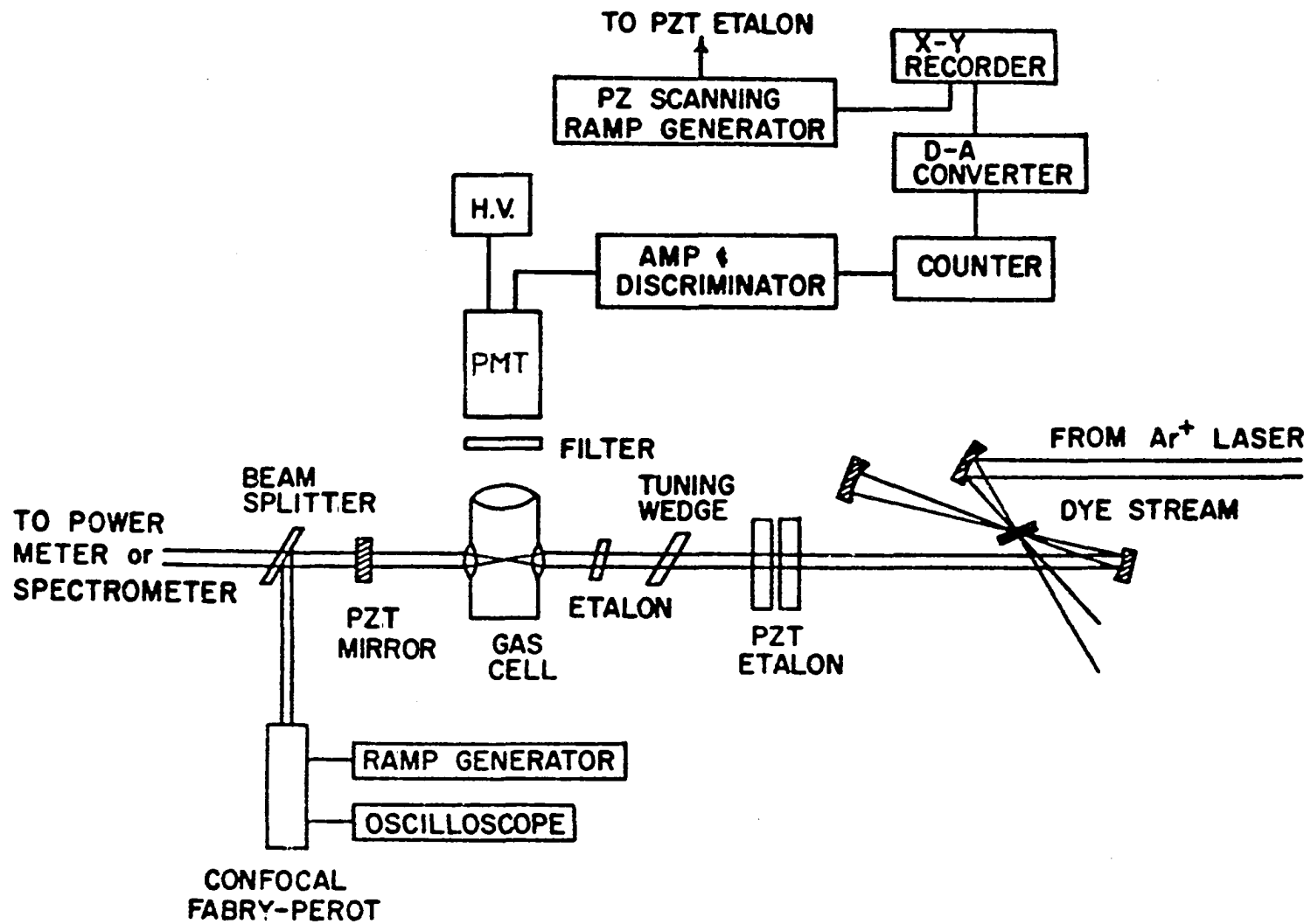
able to scan the laser over several GHz without mode-hopping. This was essential to obtaining meaningful spectra.

The fluorescence collected by the f/1 lens was detected by a Dry-Ice cooled Amperex 56DVP photomultiplier tube operated at 2200 V. Two Corion SB-1 filters were placed in front of the photomultiplier to block any scattered laser light. The fluorescence signal was monitored using standard photon-counting techniques using an Ortec Model 9315 photon counter. The analog output of the photon counter provided the Y-input to an X-Y recorder. The X-input representing the laser frequency scale was driven by the horizontal output of the ramp generator of the 481A laser scanning electronics.

The naphthalene (Merck & Co.) sample used in this work was zone refined and introduced into the sample cell by standard vacuum techniques. The vapor pressure of naphthalene at room temperature is about 70 mtorr. In order to increase the number density of the naphthalene sample and thus enhance the signal-to-noise of the DFTPA spectrum, the gas cell was heated to 35°C with heating tape raising the vapor pressure to 200 mtorr.

Results and Discussion

The reliability of our two-photon spectrometer may be evaluated by our studies on gaseous naphthalene. A low resolution two-photon excitation spectrum of naphthalene is shown in Figure 4. This spectrum was obtained by removing the electronic scanning etalon from the dye laser and stepping the laser frequency manually at 20 cm^{-1} intervals

Figure 4. Low resolution (2 Å) two-photon excitation spectrum of naphthalene at 25°C

NORMALIZED RELATIVE FLUORSCENCE INTENSITY

FREQUENCY (10³ cm⁻¹)
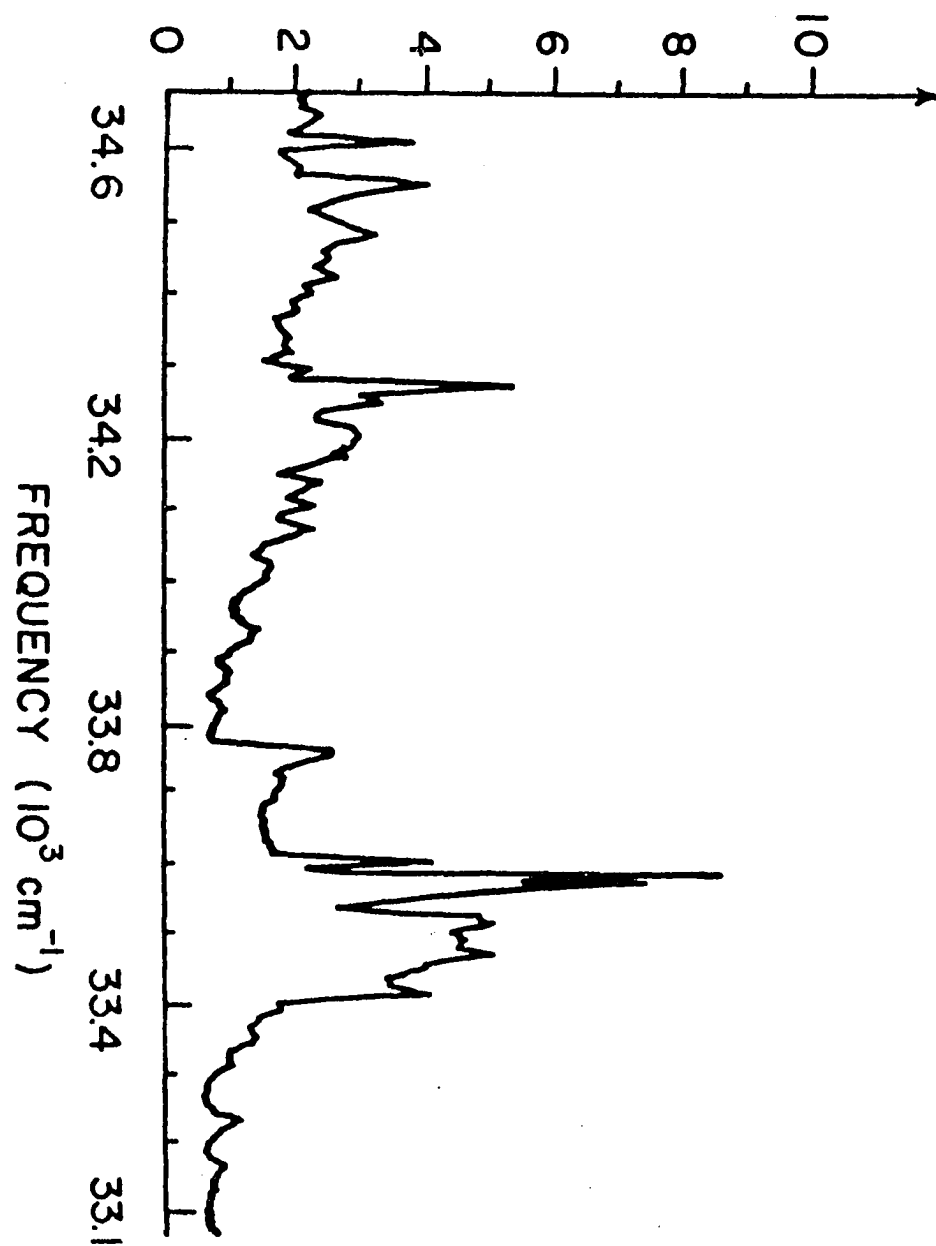
after each count period of 50 sec. The variation of laser power
(fluctuations in the Hz range) was found to be on the order of 1%.
Figure 4 represents the properly normalized (with respect to laser power
squared) spectrum of the two-photon $S_1 \leftarrow S_0$ transition of naphthalene.
The signal-to-noise ratio was better than 50 for most of the features.
This is superior to that in the spectrum obtained by Bosel et al. (46)
who studied the same system using an extracavity pulsed dye laser
system. Further comparison of the two spectra shows excellent agreement
in the position and shape of the major spectral features.

The Doppler-free two-photon excitation of naphthalene at 35°C is
shown in Figure 5. The transition frequency was around 33,500 cm^{-1} and
the total scanning range was 11 GHz, with a scan rate of 14 MHz sec^{-1}.
The fluorescence signals were counted for 10 seconds to improve the
signal-to-noise ratio. Each data point thus spans 140 MHz. Four
successive scans were taken over the same spectral region and the
computer averaged spectrum is shown in Figure 5. Judging from the
position of the major feature of the successive scans, the reproduc-
ibility of this system appears to be excellent. The spectrum in Figure 5
has not been normalized since the power fluctuations over this narrow of
a spectral region are extremely small.

The full-width-at-half-maximum (FWHM) of the distinctive features in
our spectrum were on the order of 300 MHz; this is less than the 2 GHz
Doppler width. The lifetime of naphthalene under collision-free
conditions has been measured to be 250 nsec (47). The lifetime-limited
natural linewidth of naphthalene is thus about 3 MHz. The combined

Figure 5. Doppler-free two-photon excitation spectrum of naphthalene
at 33,580 cm^{-1}

RELATIVE FLUORESCENCE INTENSITY

LASER FREQUENCY →

1 GHz
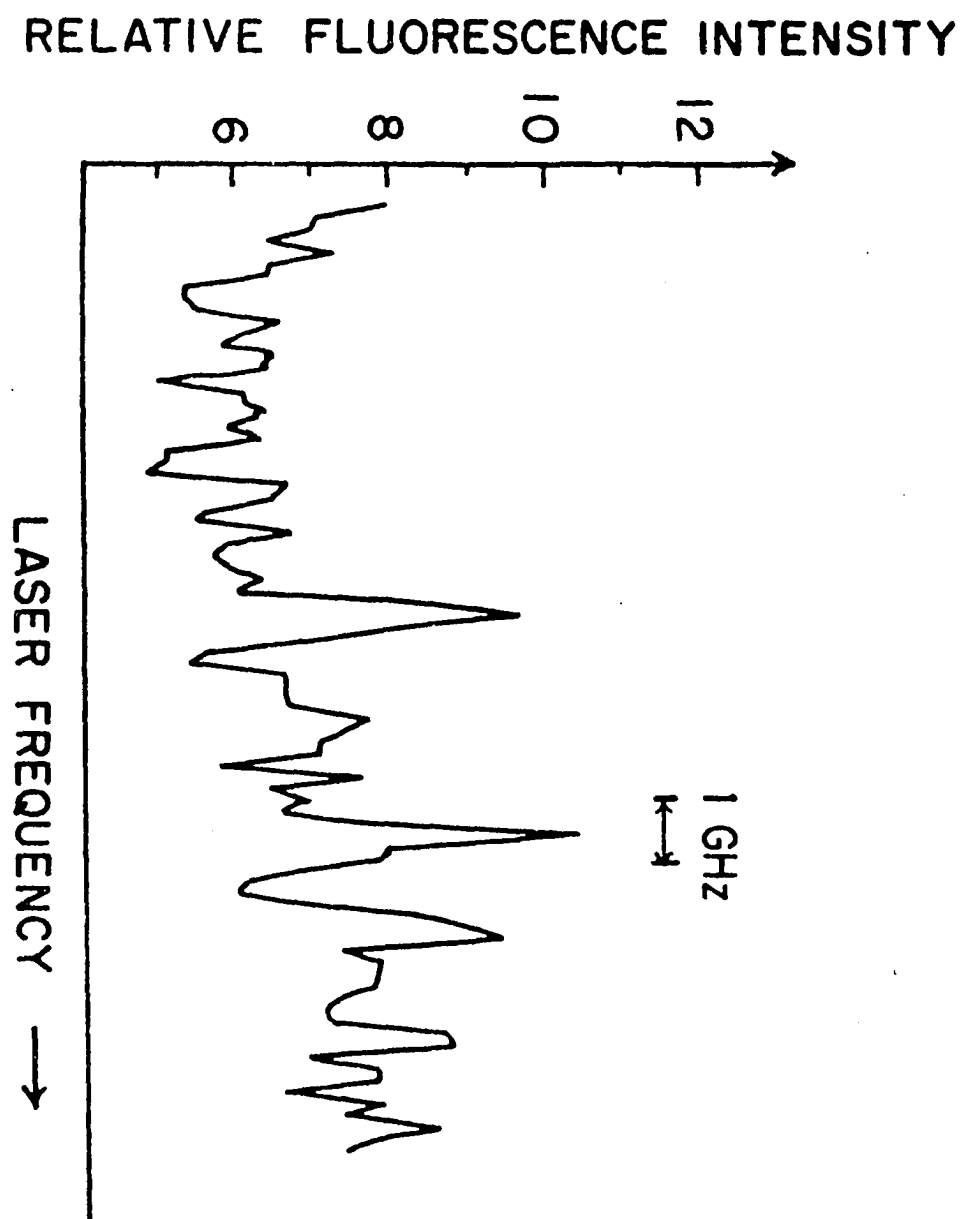
effects of laser width, frequency scan rate, and high density of states prevented us from resolving individual rovibronic lines.

In order to compare the efficiencies of cw and pulsed laser systems, it is interesting to give an order-of-magnitude estimate of the relative number of fluorescence photons detected using the two laser systems. If one considers only peak power, the pulsed systems would certainly have an edge over cw systems. This does not imply, however, that cw systems cannot be used to study TPA in molecular systems. One must also take into account duty cycle when making any comparison. A typical high-resolution nitrogen-pumped dye laser system has a peak power of 50 kW, pulse width of 10 nsec, and repetition rate of 10 Hz. Our intracavity cw dye laser system has 5 W continuous power inside the cavity. If one inserts these values into the expression for two-photon signal strength, the efficiency of the cw system comes within an order of magnitude of that of the pulsed system. Some additional advantage to the cw system results from the higher beam quality in the cw system which allows for better focusing.

The experimental configuration described here in no way represents the optimum case. Several modifications can be incorporated into the system which would increase its utility. These modifications include frequency stabilization (to a few MHz) of the dye laser by locking it to an external Fabry-Perot interferometer, wavelength calibration with a digital wavemeter to an uncertainty of one part in 10^7, and if necessary, reduction of transient time broadening by increasing the size of the beam waist and improving the collection optics.

Conclusion

We have demonstrated the first DFTPA in a large aromatic molecule -- naphthalene. The technique of intracavity cw DFTPA developed here displays adequate sensitivity for studies of low pressure gases. Elimination of beam overlap problems and use of a cw laser allow for higher resolution than attainable with pulsed laser systems. Even under low resolution conditions, the higher signal-to-noise ratios and each of normalization make the use of a cw laser system desirable. Features in Figure 5 show a width that is narrower than the Doppler width but wider than the lifetime or laser scan rate limited width. This shows that even for a large molecule DFTPA can lead to better upper state spectroscopic constants from the rotational contours obtained.

DETERMINATION OF ABSOLUTE RAMAN CROSS SECTIONS
USING THE INVERSE RAMAN EFFECT

Theory and Review of Related Work

Inverse Raman spectroscopy is another of the nonlinear spectroscopic techniques that have become feasible because of the laser. The inverse Raman process can perhaps be best explained by comparing it to other types of Raman processes. Figure 6 depicts the events which occur in Raleigh scattering (Fig. 6a), conventional Raman scattering (Fig. 6b), stimulated Raman scattering (Fig. 6c), and inverse Raman scattering (Fig. 6d).

The initial $|a>$, and final $|b>$ states represent real vibrational energy states of the molecule. They are separated by energy E_v.

When the system is irradiated by a photon field at ν_L, the system may abstract a photon from the field and move to an intermediate level $|c>$; this level may be real as in the case of resonance Raman scattering or it may be a virtual level. Once excited, the molecule may scatter a photon in one of two different manners. It may either scatter a photon of the same energy as the abstracted photon and return to its original level (Fig. 6a), or it may scatter a photon of different energy and move to a different energy level (Fig. 6b). The first case is known as Raleigh scattering and is the predominant process. The second case is referred to as Raman scattering. In the Raman case, the scattered photon will have the following relationship with abstracted photon:

$$h\nu_S = h\nu_L \pm E_v \tag{5}$$

Figure 6. Molecular processes taking place in (a) Raleigh scattering,
(b) conventional Stokes Raman scattering, (c) stimulated
Raman scattering, (d) inverse Raman scattering

Excitation

Spontaneous Scattering

Stimulated Scattering
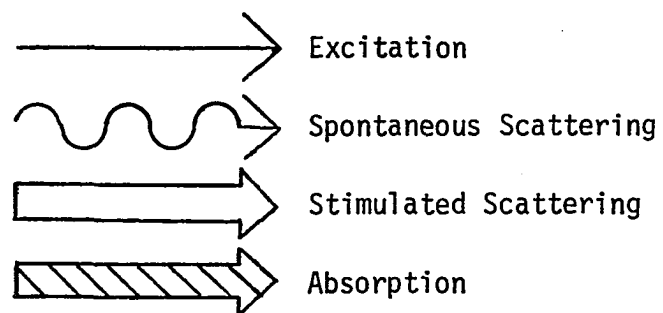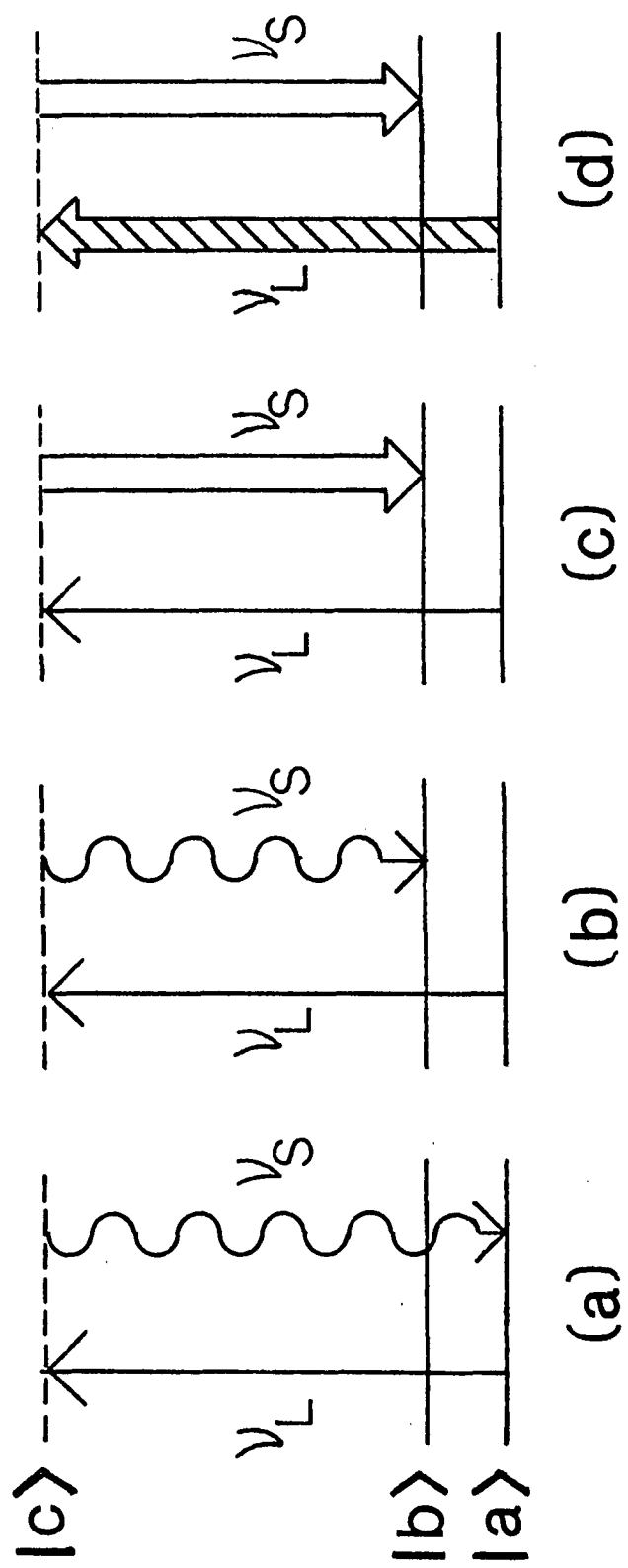
Absorption

The scattered light is historically referred to as Stokes scattering if it is at lower energy than ν_L and as anti-Stokes scattering if at higher energy than ν_L.

It should be pointed out at this time that the absorption and the scattering processes are not sequential in nature but are temporally inseparable.

As the intensity of the photon field at ν_L is increased, the scattering at ν_S may become intense enough to cause stimulated scattering at ν_S. This process is known as stimulated Raman scattering and is shown schematically in Figure 6c. Stimulated Raman scattering exhibits threshold behavior and only the strongest Raman transitions will undergo stimulated scattering.

The inverse Raman process is shown in Figure 6d. It differs from both conventional and stimulated Raman processes in that two photon fields at ν_S and ν_L are used to irradiate the sample instead of a single field at ν_L. ν_L may be supplied either as a spectral continuum or as a sharp laser line; ν_S is always a sharp line. These two fields must be coincident in space and time. The presence of a large field at ν_S guarantees the stimulated condition and for each photon created by scattering at ν_S, a photon at ν_L is annihilated. In this way, one may measure the absorption at ν_L rather than the scattering at ν_S. The length-dependent intensity of the probe laser at ν_L is described by (48):

$$I_L(\ell) = I_L(0)\exp\{-g\ell\} \tag{6}$$

where ℓ is the length of the sample and g (49) is the quantity:

$$g = \frac{10^7 P_S \omega_L N(d\sigma/d\Omega)}{3hc^2 \Delta\omega \omega_S^4 n_S^2} \tag{7}$$

ω_L and ω_S are the frequencies (in cm^{-1}) of the probe and exciting lasers, P_S is the power density (W/cm^2) of the exciting laser, N is the number density (molecules/cm^3) of the sample, $d\sigma/d\Omega$ is the Raman cross-section (cm^2/sr), $\Delta\omega$ is the width of the Raman line, n_S is the refractive index of the sample at ω_L, and h and c are Plank's constant and the speed of light in cgs units.

It may not be obvious at this point why one would choose to do inverse Raman spectroscopy rather than conventional Raman but inverse Raman does offer some advantages over conventional Raman. Perhaps the largest problem associated with conventional Raman spectroscopy is that it is a very weak effect. Only on the order of 10^{-8} of the incident intensity is Raman-scattered. In conventional Raman studies the collection optics are placed at 90° to the excitation field and can collect only a small portion of the already weak signal. Increasing the inter-action path length in an attempt to increase signal strength is only of marginal use since the efficiency of the collection optics decreases rapidly as one tries to collect signal from a larger area. Inverse Raman on the other hand is an absorption process and the signal increases linearly with increased path length. Since the absorption is occurring from a spatially well-defined laser beam, there is no problem with the collection optics.

It can be seen in Figure 6b that conventional Stokes Raman scattered photons are at a lower energy level than the excitation photons. This is also the case with fluorescence. As stated before, the Raman process is very weak; fluorescence, on the other hand, can be an extremely strong effect. For compounds that exhibit even weak fluorescence, the signal due to Raman scattering will be completely obscured. This may be a difficult problem since many interesting systems for Raman studies fluoresce strongly. Raman lines are typically quite sharp relative to fluorescence bands and can sometimes be discriminated from fluorescence in this manner. If not, it may be necessary to resort to wavelength modulation (50) or gated detection (51) to remove fluorescence interference. In the inverse Raman technique, the probe beam is at higher energy than the fluorescence so that no interference from fluorescence should be encountered with the possible exception of hot-band fluorescence. Even so, the small solid angle required to collect the entire laser beam at ν_S allows for a high degree of spatial filtering of whatever hot-band fluorescence there may be.

Another advantage of the inverse Raman technique is that an entire spectrum may be taken in the time span of a single laser shot. This can be particularly advantageous for the study of rapidly transient species.

In most of the early inverse Raman studies, ν_L was generated as a continuum. The first reported inverse Raman spectrum was obtained by Jones and Stoicheff (52). They made use of a high-power ruby laser and stimulated Raman scattering from toluene on the anti-Stokes side of the ruby as the two sources of photons. They were able to observe inverse Raman absorption for the benzene 992 cm^{-1} line, the pyridine 990 cm^{-1} line

and the nitromethane 918 cm^{-1} line. Duardo et al. (53) used the same

liquid, acetonitrile, both to generate anti-Stokes scattering at

$\omega_L + 2940$ cm^{-1} and as an absorber at $\omega_L + 2250$ cm^{-1}. Two different liquids

have even been placed in the same cell, one to generate the continuum and

the other to act as the absorber (54). Other continuum sources include

fluorescence from organic dyes (55,56), self-phase modulation of intense

laser pulses in liquids and solids (57). Most of these techniques provide

a rather weak continuum and may require several shots to achieve

sufficient exposure for photographic detection.

Yeung (48) has developed a system which provides a strong continuum

source. In this arrangement, the second harmonic of a ruby laser is used

to pump a broad-band dye laser. The output from the dye laser is then

combined with the ruby fundamental to provide the two sources of photons.

One of the main criteria by which any technique is judged is its

sensitivity. There have been several attempts to detect minor components

in a mixture using inverse Raman scattering. Gadow et al. (54) found

little improvement over stimulated Raman. After a number of modifications

to their technique, however, they were able to detect components in the

concentration range of from 5×10^{-3} mole/liter for pyridine to

1.0 mole/liter for aniline and acetophenone. There have been several

attempts to increase the sensitivity of the inverse Raman process through

resonance enhancement (54,58,59). These studies were plagued by a number

of problems associated with the resonance condition; however, it is

estimated (58) that with the use of resonance enhancement and

photoelectric detection, a detection limit on the order of 10^{-6} mole/ liter will be possible.

As was stated earlier, inverse Raman spectroscopy can be a powerful took for obtaining Raman spectra from highly fluorescent species. This application is demonstrated in a study done by Werncke et al. (58). In this study they obtained inverse Raman spectra of a series of motor oils which were too highly fluorescent to study by conventional Raman techniques. Caution must be exercised when taking the inverse Raman spectra of fluorescing materials since the presence of fluorescence indicates an absorption mechanism other than inverse Raman absorption which may complicate spectral analysis. Other studies using the inverse Raman technique include those of Strizhevskii and Kondilenko (60) who studied polarization effects in inverse Raman scattering, and VonHolle (61) who used inverse Raman scattering to monitor the spontaneous decomposition of a liquid propellent.

All of the inverse Raman studies mentioned to this point were done with both ν_L and ν_S supplied by pulsed sources. It may, however, be convenient to use a cw source for these photons since cw sources tend to be more stable than pulsed sources and would afford better signal-to-noise ratios. The main problem with using two cw sources is in the achieving of sufficient power density at ν_L to create a measurable absorption. Stone (62) has observed Raman scattering from several liquids by continuous generation in optical fibers using two cw sources. This particular experimental arrangement has the advantage of a log interaction length between the photon fields. Other techniques which may allow the use of

two cw sources measure the inverse Raman absorption indirectly. In this way it is possible to measure a small signal in the presence of essentially no background rather than measuring a small change in a large signal. These techniques include photoacoustic detection (63) and Raman-induced Kerr effect spectroscopy (RIKES) (64).

A reasonable compromise between using two pulsed sources or two cw sources seems to be the use of a pulsed source to provide the high power necessary at v_L and a more stable cw source to provide the field at v_S. This approach has been adopted by at least two groups (65,66).

The determination of absolute Raman cross-sections has long been of interest to conventional spectroscopists. In addition to its obvious application in Raman spectroscopy, Raman cross-sections have found use in predicting stimulated Raman gain coefficients (67), absolute two-photon absorption cross-sections (68), and intensities in coherent anti-Stokes Raman scattering (69).

During the pre-laser era, only relative scattering intensities could be obtained due to ill-defined excitation intensities and uncertainties in the interaction volume. Still some absolute intensity standards were suggested to overcome these problems. Brandmuller and Schrotter (70) have suggested using Raman to Raleigh intensity ratios as a possibility, but this is not reliable due to small-range order of the molecules in liquids and intermolecular forces. The H_2 J=1 to J=3 transition has been suggested by Udagawa et al. (71) because of the availability of theoretical predictions, but this standard cannot be used for liquids. Even laser Raman measurements (72,73) are not free from problems, the

major ones being (i) calibration of detector response; (ii) efficiency of the spectrometer; (iii) definition of the angle of collection; (iv) neglect of the angular dependence of the scattering process; and (v) the temperature dependence of the Raman intensity. Several attempts have been made to determine accurate cross-sections by conventional Raman scattering with perhaps the best to date being that of Kato and Takuma (74). The heart of their system was two identical optical systems separated by a rotating section mirror. This mirror would alternately project 1:1 images of the interaction volume and a slit opening of a blackbody source onto the entrance slit of a double monochromator. The laser was then attenuated until a balance between the intensities was achieved. The cross-section could then be calculated by using a formula derived by these authors. This experimental arrangement eliminates the sources of error (i), (ii), and (iii) of those previously noted, but does not help with respect to problems (iv), and (v). The large discrepancies in reported cross-sections from various laboratories indicate that good precision may not prove the reliability of the method in absolute terms.

The potential of inverse Raman spectroscopy for the determination of absolute Raman cross-sections has been pointed out by Yeung (48). This work made use of two pulsed sources and photographic detection. The use of photographic plates made calibration of the absorption difficult. The determination of peak laser powers and uncertainty about temporal overlap leads to uncertainties in the results. In the following section, an alternate experimental arrangement free from the limitation mentioned above is presented.

Experimental

The experimental arrangement used in this study is shown in Figure 7 and is similar in many ways to those used to measure two-photon absorption (75) or Stokes Raman gain (76). A laboratory-constructed, passively Q-switched, ruby laser (R) provided the photon field at ν_L. The output of the ruby laser was directed by a dichroic beam splitter (M2) first through a 10 cm liquid cell (C) containing nitrobenzene and then into a factory-calibrated Hardron ballistic thermopile (B). The thermopile measured the energy of each ruby pulse and recorded it on a stripchart recorder.

The field at ν_S was provided by a Spectra-Physics model 581 cw dye laser (D). This cw laser was gated by an intracavity Pockels cell (PC). The output of the dye laser was expanded 10X by an Oriel B-34-40 beam expander to match more closely the diameter of the ruby laser output. After passing through a 15 meter optical delay line, the expanded dye laser beam was combined with the ruby field by M1 making sure that there was complete overlap of the two beams while passing through the liquid cell. The output of the dye laser was then focused into a Bausch and Lomb 1/4 meter double monochromator (S) with a spectral slit width of 2.0 nm centered about the dye laser wavelength.

The dye laser intensity was monitored with an Amperex 56TVP photomultiplier tube (P) with high current base and displayed on a Tektronix 7904 oscilloscope (O) using a 7A19 vertical amplifier and a 7B92 time base. The photomultiplier tube was capable of operating linearly at output currents up to 300 ma for a few microseconds. As mentioned before,

Figure 7. Experimental arrangement used to measure the absolute Raman
scattering cross section of nitrobenzene. Ruby laser (R);
Pockels cell (PC); Ballistic thermopile (B); Sample cell (C);
Monochromator (S); Photomultiplier tube (P); Oscilloscope (0);
Trigger Generator (T); High voltage amplifier (A)

M1

M2

M2

M1

C

S

P

R

B

ODL

D

PC

A

T

O
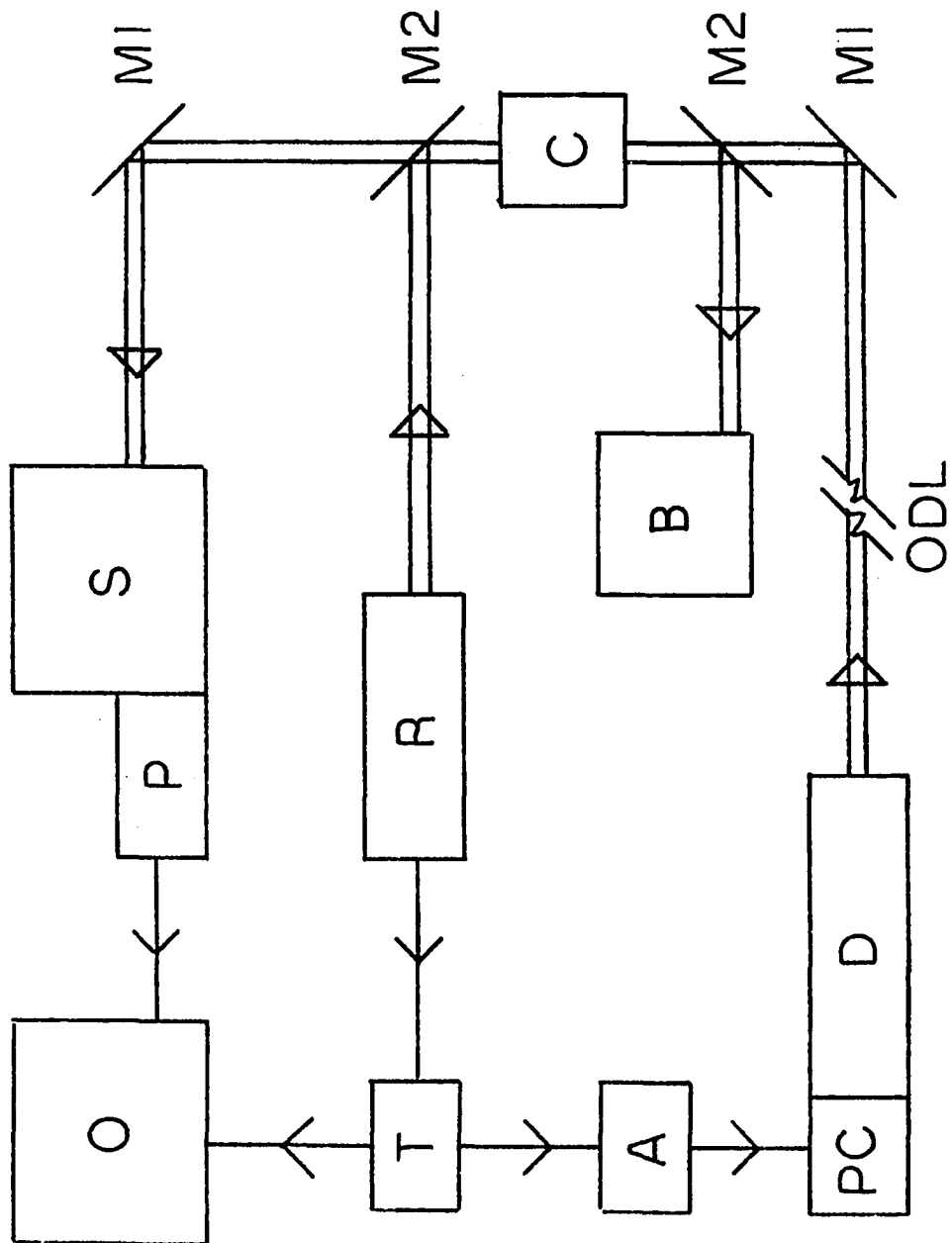
the dye laser was gated by a Pockels cell; this was necessary in order to center a "pulse" from the cw laser around the pulse from the ruby laser. If the dye laser were not gaged, the performance of the photomultiplier tube would degrade rapidly under such high illumination. By placing the Pockels cell inside the dye laser cavity, lasing was quenched by introducing high loss at the polarization of lasing when a high voltage DC field was applied to the Pockels cell from a Burleigh PZ-70 high voltage operational amplifier (A). When the ruby laser was fired, the delay generator (T) would clamp the output of the high voltage operational amplifier to ground for a few microseconds, gating out a "pulse" from the dye laser. The time of the delay generator was such that the dye laser was gated on several μsec before the ruby laser was fired, and gated off well after the ruby pulse.

Results and Discussion

A problem was encountered very early in this work. While monitoring the dye laser power as the ruby laser was fired, it was found that the dye laser output was quenched by a small amount of the ruby field which was being fed back into the dye laser cavity. This quenching masked any inverse Raman absorption that may have been present. To alleviate this problem, an optical delay line was placed in the path of the dye laser. The additional time required for the ruby field to reach the dye laser provided an unperturbed window in the dye laser output which bracketed the ruby pulse in the time domain.

Once this problem was solved, it appeared that inverse Raman absorption was very easy to obtain as the first oscilloscope traces showed an attenuation of the dye laser that was synchronous with the arrival of the ruby field in the liquid cell. However, as the dye laser was tuned off the Raman resonance, the attenuation did not disappear as would be expected. The observed behavior was a result of dielectric breakdown of the sample (77). This problem was eliminated by extensive filtering of the sample to remove suspended particulates.

After tuning the dye laser in the region of Raman resonance, an unambiguous inverse Raman absorption was finally monitored. This was confirmed by the fact that the absorption disappeared when the dye laser was tuned off resonance or if the ruby field was blocked before entering the sample cell.

Figure 8 shows a typical oscilloscope trace. The horizontal axis represents time (50 nsec/div.) and the vertical axis represents dye laser intensity increasing from top to bottom. The dot in the upper left represents zero-intensity output from the dye laser. The dye laser was gated on several microseconds before the beginning of the trace to allow it to stabilize at the intensity value at the beginning of the trace. The first drop in laser intensity is coincident with the arrival of the ruby field at the sample cell and represents inverse Raman absorption. The second drop in intensity represents the quenching of the dye laser by the ruby field and is the reason for the addition of the optical delay line.

Figure 8. Oscilloscope trace of inverse Raman absorption
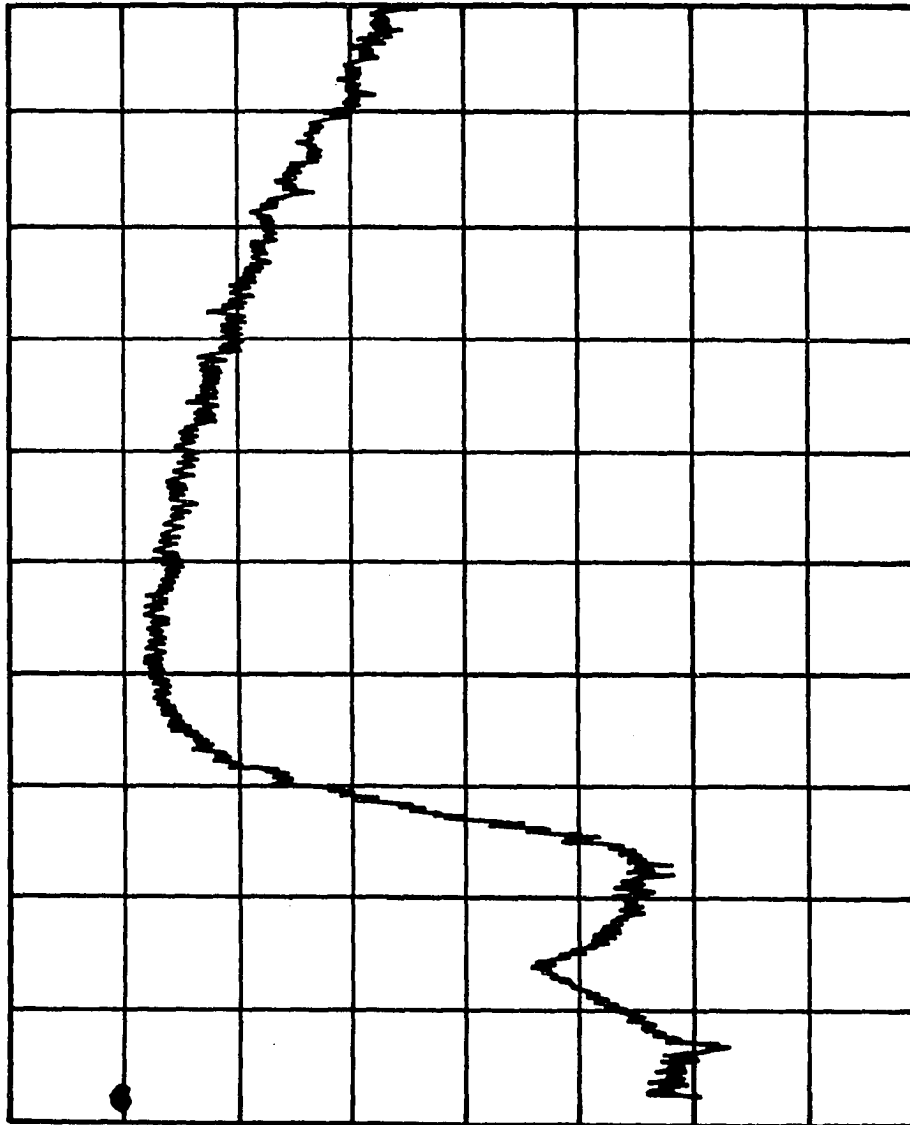
The data analysis is as follows. In order to determine a value for the absolute Raman cross-section, it is first necessary to measure the inverse Raman absorption g in equation 6. Values for $I_L(\ell)$ and $I_L(0)$ can be measured directly from the oscilloscope traces. By rearranging equation 7, one arrives at the following equation to describe the absolute Raman cross-section:

$$d\sigma/d\Omega = \frac{3hc^2 g\Delta\omega\omega_s{}^4 n_s{}^2}{10^7 P_s \omega_L N} \qquad (8)$$

In this work, ω_s is 14402 cm^{-1} as determined by the ruby laser output. For the nitrobenzene line at 1345 cm^{-1} ω_L is 15747 cm^{-1}. From published conventional Raman studies, $\Delta\omega$ has a value of 6.6 cm^{-1} (78). The number density N is calculated from density data to be 5.86×10^{21} molecules cm^{-3} and the refractive index n_s is taken to be 1.55 (79). The length of the sample cell throughout this work was 10 cm. The final value which is needed to complete this calculation is the power density of the ruby field at the absorption peak. The ballistic thermopile records only the total energy of the pulse and must be divided by the full-width-at-half-maximum of the absorption peak as measured from the oscilloscope trace. Using equation 8 and correcting for a nonzero depolarization ratio of 0.15 (80), the results of our effort for a total of 65 trials yield an absolute Raman cross-section of $(2.37 \pm 0.51) \times 10^{-29}$ cm^2 sr^{-1} for the 1345 cm^{-1} line of nitrobenzene.

This result is to be compared to the published values for nitrobenzene cross-sections of 1.56×10^{-29} cm^2 sr^{-1} (80) and 1.93×10^{-29} cm^2 sr^{-1} (67). Since no estimates of accuracy were given for these

values, there appears to be agreement between our value and theirs. When compared to typical reported Raman cross-sections, our reported uncertainty is quite high. This is because relatively high precision can be obtained by conventional techniques but the accuracy of such measurements may not have been realistically estimated. In any case, improvements in the present uncertainty limit can be expected with refinements in our experimental technique. The most valuable of these refinements may be the addition of a second oscilloscope to monitor the peak shape of the ruby laser pulse, making the determination of laser power density more reliable.

We now need to show that our method is in fact more reliable than the other methods for the determination of absolute Raman cross-sections by considering in detail the various sources of inaccuracy.

The calibration of detector response and the efficiency of the spectrometer are not of concern when using the inverse Raman technique since we are measuring absorbance which is a relative measurement rather than measuring an absolute signal as in conventional Raman studies.

The angular dependence of the scattering process has been properly taken care of. The two lasers have beam divergence of less than 5 mrad and are aligned to be propagating at $180° \pm 1°$. This is far better than the collection cone of a typical Raman spectrometer.

Because of the short pulse duration and the larger cross-sectional areas of the laser beams in our method, the extent of heating of the sample is minimized relative to typical laser Raman methods. This minimizes the temperature effects on scattering intensity.

Both of the lasers used in our study are of sufficient resolution (less than 1 cm^{-1}) to be centered at the peak of the nitrobenzene line, which has a width of 6.6 cm^{-1}. Tuning of the dye laser to maximum inverse Raman absorption removes any inaccuracy in the absolute frequencies of the lasers due to such things as temperature shift of the ruby laser frequency.

Complete spatial and temporal overlap of the two lasers is assured in our optical arrangement. The ruby has a diameter of 0.9 cm^{-1} and the dye laser has a diameter of 0.5 cm^{-1}. This means that the entire probe laser can be covered by the pump laser, even if the two lasers are slightly misaligned. Time coincidence of the two lasers is assured since one of the two lasers is a continuous wave laser. This eliminates many of the synchronization problems encountered in earlier studies (48).

Conclusion

We have demonstrated that inverse Raman spectroscopy can be a valuable technique for the determination of absolute Raman cross-sections. Our experimental arrangement which couples a giant-pulse ruby laser with a cw dye laser eliminates many of the sources of inaccuracy associated with conventional as well as other inverse Raman cross-section determination methods.

RESONANCE ENHANCED THREE-PHOTON ABSORPTION
OF MOLECULAR IODINE

Theory and Review of Related Work

Recently, several nonlinear spectroscopic techniques have been developed to study high-lying and Rydberg states of gaseous molecules. As discussed previously, these nonlinear effects are usually weak and require very high laser power to measure any appreciable signal. The information that can be gained about these molecular systems via these techniques is, however, of great importance since it is often unattainable by other means.

Among the molecular systems studied to date, a simple molecule, iodine, is often chosen by authors to demonstrate their technique. This choice is made for a number of reasons. First among these is the fact that being a homonuclear diatomic molecule, the spectrum of iodine is relatively easy to model theoretically when compared to heteronuclear polyatomic species. The spectrum of iodine is also reasonably simple which facilitates spectral analysis. Secondly, since iodine has been so extensively studied over the years, a tremendous amount of spectral data has been compiled which is useful for both predictive and confirmative purposes. The real advantage of the iodine system to the nonlinear spectroscopist is that resonance enhanced absorption through the low lying B state of iodine reduces the high power requirements for multiphoton processes.

To avoid confusion, we must at this point carefully define the two different types of multiphoton absorption that will be discussed in this section. Those multiphoton processes which pass through a resonant intermediate state will be referred to as sequential multiphoton processes and those whose intermediate state is a virtual level will be referred to as simultaneous multiphoton processes.

To better understand this resonance enhancement, it is helpful to look at it from a theoretical viewpoint. For the purpose of this description, we will discuss two-photon absorption; however, the same arguments will hold for higher order processes. The two-photon absorption cross-section depends on the square modulus of a sum over all molecular ("intermediate") states (2):

$$\left| \sum_i \left[\frac{(e_1 \cdot M_{oi})(M_{if} \cdot e_2)}{\omega_{oi} - \omega_1} + \frac{(e_2 \cdot M_{oi})(M_{if} \cdot e_1)}{\omega_{oi} - \omega_2} \right] \right|^2 \qquad (9)$$

where e_1 and e_2 are the polarizations of the photon vectors, M_{if} the transition moment between states o and i, M_{of} the transition moment between states i and f, ω_{oi} the transition frequency between states o and i, and ω_1 and ω_2 the photon frequencies. This expansion diverges as ω_{oi} approaches ω_1 or ω_2. The approach to resonance has been discussed by Bonch-Bruevich and Khodovoi (80). In the nonresonance case, the molecule has no energy level at $E_o \pm \hbar\omega_1$ or $E_o \pm \hbar\omega_2$. After the molecule absorbs the first photon at $\hbar\omega_1$ inducing the $o \rightarrow i$ transition, it must absorb a second photon at $\hbar\omega_2$ within the same constraint of the Heisenberg uncertainty principle:

$$\Delta t = \mid \omega_{oi} - \omega_1 \mid^{-1} \qquad (10)$$

The small value of Δt can be thought of as the limiting factor which makes two-photon absorption in the absence of resonance an extremely weak effect. If the intermediate state is a real state, then $\omega_{oi} - \omega_1 < \gamma_i$, where γ_i is the width of the intermediate level. At this point, the two transitions $o \rightarrow i$ and $i \rightarrow f$ can be thought of as separate one-photon processes. Under these conditions, the rate of the sequential two-photon process is described by:

$$\Gamma_{of} = \Gamma_{oi} (\gamma_i)^{-1} \Gamma_{if} \qquad (11)$$

where $(\gamma_i)^{-1}$ is the natural lifetime of the intermediate state and Γ is the absorption rate of the designated process.

Even though resonance enhancement lowers the high power requirement for multiphoton processes, it does not change the power dependence of the signal or the selection rules which govern the absorption process.

As stated earlier, the iodine molecule has been the subject of much spectroscopic research over the years. The spectroscopy of iodine is discussed in an excellent paper by Mulliken (81) in which he critically reviews the research done on iodine before 1970. Since that time, there have been a number of laser spectroscopic studies done on iodine which take advantage of resonance enhancement in one way or another.
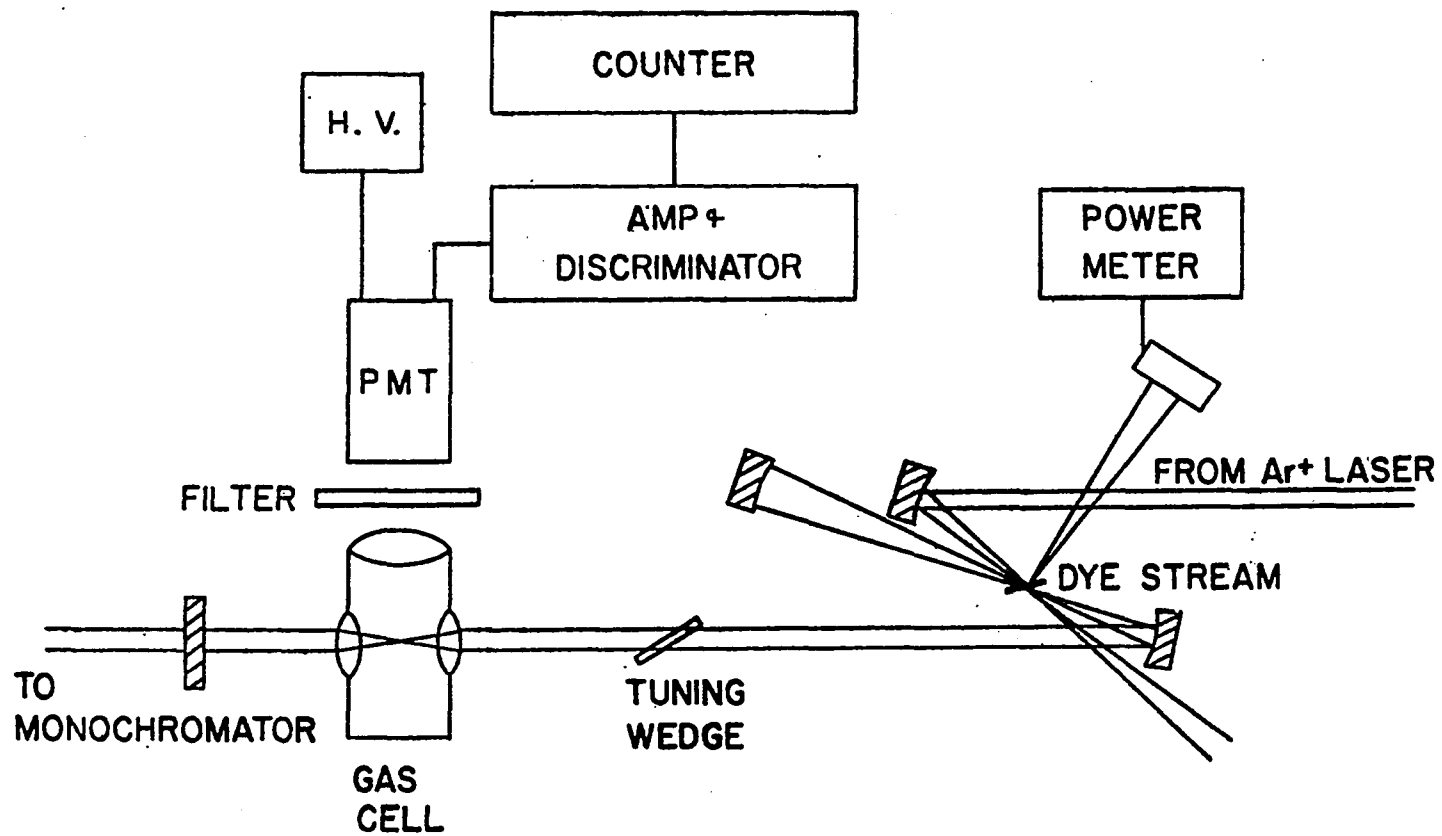
Rousseau and Williams (82) have used a sequential two-photon technique to study the E state of molecular iodine via a resonant B state intermediate. Similar techniques employing two independently tunable dye lasers have been developed by Danyluk and King (83) and Williamson (84).

Sander and Wilson (85) have applied the photofragment spectroscopic technique to study the repulsive states of iodine after population by resonance enhanced two-photon absorption. Resonance-enhanced photoionization of iodine has been reported by Petty et al. (86), Dalby et al. (87) and Zandee et al. (88). In this chapter we report the first observation of $D \leftarrow X$ resonanced three-photon absorption in iodine.

Experimental

The experimental arrangement for this study is essentially the same as that used in the Doppler-free two-photon absorption study described earlier in this dissertation. We have, however, made several modifications on the laser system. A schematic diagram of the experimental apparatus is shown in Figure 9. The Spectra-Physics Model 580A continuous-wave dye laser was modified to incorporate the intracavity gas cell. The dye laser was pumped by a Control Laser Model 553A Ar^+ laser operating at 5 W all lines. The intracavity gas cell shown in Figure 2 was retrofitted with two Melles Criot 10 mm diameter, 20 mm focal length, broadband anti-reflection coated, "best form" quartz lenses. These lenses were of higher quality than those used in the naphthalene experiment. This has the effect of reducing cavity losses and increasing the available intracavity power. A typical power inside the dye laser cavity was about 3.5 W. The dye laser power was monitored by an Eppley thermopile from the reflected light off the dye jet. A Bausch & Lomb 1/4 m double-grating monochromator with 2 Å resolution was used to monitor the wavelength of the dye laser output. The fluorescence collected by the f/1 fused silica

Figure 9. Experimental apparatus of a cw intracavity absorption laser system

COUNTER

H. V.

AMP +
DISCRIMINATOR

POWER
METER

PMT

FROM Ar+ LASER

FILTER

DYE STREAM

TO
MONOCHROMATOR

TUNING
WEDGE

GAS
CELL

collection lens was monitored by a Dry-Ice cooled Amperex 56DUVP photo-multiplier tube. Two Corion SB-1 solar blind filters were used to block the scattered laser light and dye fluorescence. The signal from the photomultiplier tube was monitored by an Ortec Model 9315 photon counter. The background signal due to dark current and scattered light was about 2 counts sec^{-1}.

The iodine sample was vacuum sublimed and introduced into the gas cell by standard vacuum techniques. The vapor pressure of I_2 is about 0.25 torr at room temperature. After tuning the laser to a strong feature, the alignment of the laser and the gas cell was adjusted to provide a clean TEM_{00} mode dye laser output. It was necessary to preserve this mode structure throughout the entire tuning range of the dye laser. Spectra of I_2 were obtained by manually tuning the dye laser at 2 Å intervals and counting the fluorescence for fifty seconds to improve the signal-to-noise ratio. The highest counting rate (before normalization) was more than 500 counts sec^{-1}. Spectra were obtained over the tuning ranges of Rh 6G and Rh 640 laser dyes.

For experiments measuring the pressure dependence of the signal, the gas cell was fitted with a temperature controlled side arm and a MKS Baratron manometer to measure the pressure of the I_2 vapor. Power dependency experiments were done by changing the power of the pump laser which resulted in a change in the dye laser power. Care was taken that the mode structure of the dye laser did not change with the changing pump laser power.

Results and Discussion

In order to determine the source of the observed fluorescence signal, one of the first experiments that must be done is a power dependence study. Such a study done on several of the strong spectral features indicates that a three-photon process is responsible for the observed fluorescence. Although a power dependence study provides a good indication of the type of process being observed, one should be careful when interpreting the experimental results. This is of particular importance when studying a rotationally resolved molecular system with a multimode laser. If the system under investigation has homogeneously broadened spectral widths larger than the bandwidth of the laser, e.g., solid or liquid samples, the n-th power dependence of the signal on laser power should be strictly followed up to saturation. For a gaseous sample, the expected power dependence can be observed if one is using a single-frequency laser. For a multimode laser, the observed power dependence will be lower than that expected. This is a result of the fact that not all of the laser output will be participating in the excitation process. In our particular experimental arrangement, we have additional problems due to intracavity one-photon absorption. The laser modes that are strongly absorbed will be completely quenched if the pumping power cannot compensate for the loss.

Our studies indicate a $(power)^{2.8}$ dependence of the fluorescence signal in the Rh 640 region and a $(power)^{3.5}$ dependence in the Rh 6G region. Figure 10 shows a power dependence plot for one of the strong features in the Rh 6G region. Since I_2 absorbs weakly in the Rh 640

Figure 10. Power dependence plot of fluorescence signal in the
Rh 6G region
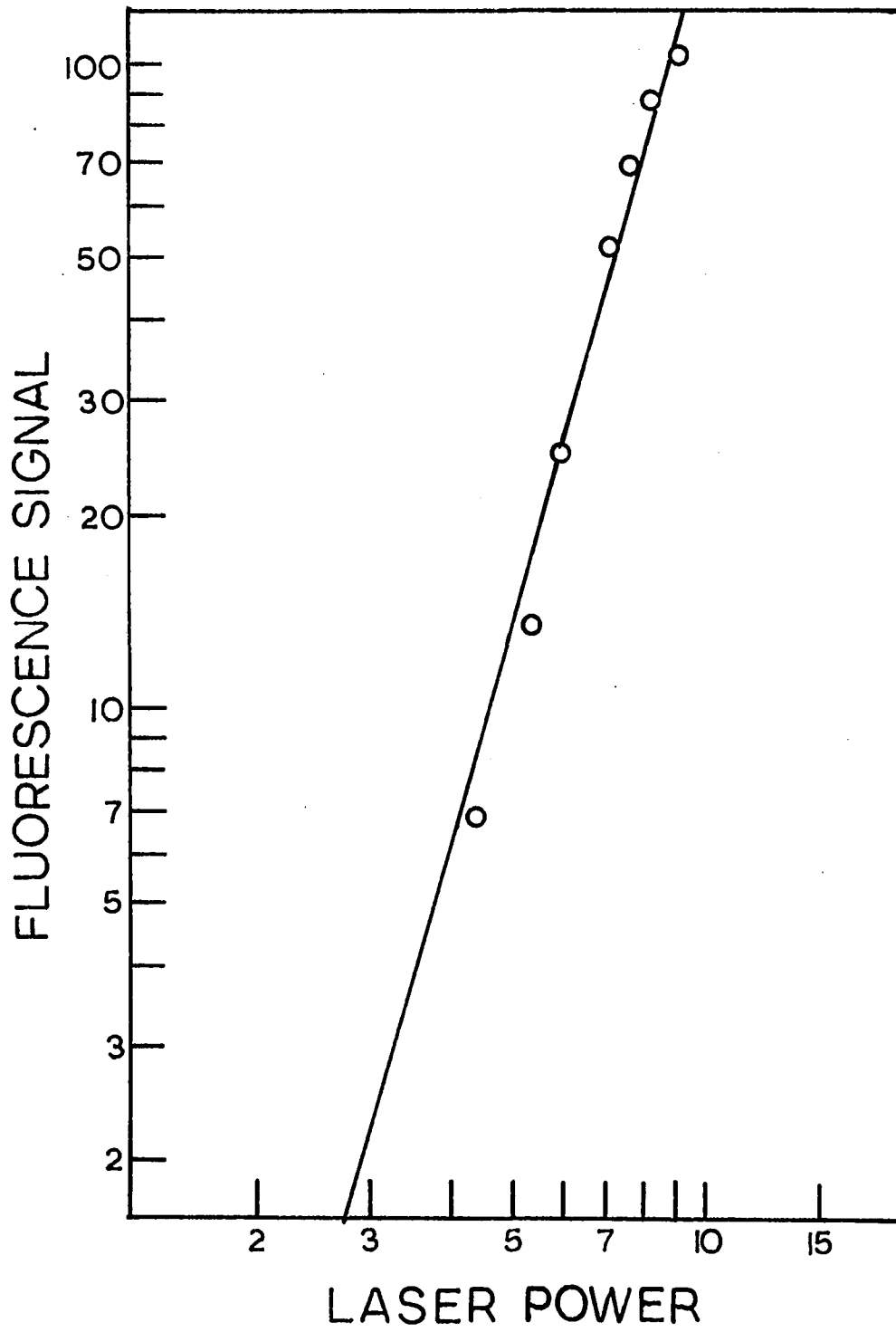
region, the quenching effect is not as prominent there as in the Rh 6G region where, under weak pumping conditions, the dye laser will not lase at those modes which are strongly absorbed. Thus, we expect a larger power dependence in the regions which are strongly absorbed and vice versa.

A pressure dependence study shows that the fluorescence signal is a linear function of iodine pressure up to 0.1 torr. At higher iodine pressures, self-quenching of the fluorescence signal becomes apparent. This quenching probably takes place via a mechanism proposed by Callear and Metcalfe (89).

If the observed fluorescence results from two-photon excitation, the parity selection rule requires that a collisionally-induced curve crossing occur for the molecule to reach a fluorescing u state. Under these conditions, a larger-than-linear power dependence would be expected. The nearest u state is the D state which is at too high an energy for collisions to be effective, particularly towards the low-frequency end of the spectrum. In light of this evidence, a two-photon mechanism can be ruled out.

By placing additional cut-off filters in front of the photomultiplier tube, we were able to identify the peak wavelength of the fluorescence to be around 3200 Å. Although no attempt was made to further characterize the fluorescence spectrum, its peak is consistent with reported $D \rightarrow X$ fluorescence (90). The parity selection rule for a three-photon process allows only transitions to states of opposite parity. This condition is satisfied by a three-photon $D \leftarrow X$ excitation mechanism.

The three-photon excitation spectra of I_2 in the Rh 640 and Rh 6G regions are shown in Figures 11 and 12, respectively. The fluorescence intensities shown are normalized with respect to laser power cubed. The fluorescence intensities in Figures 11 and 12 have not been normalized with respect to each other since changing the laser dye also requires changing the dye laser mirrors. This changes the mode properties of the laser making normalization impossible.

Three-photon absorption from rhodamine family dye lasers excites high into the vibrational manifold of the D state of I_2. Even though the available dye laser power is only a few watts, the resonance enhancement through the B state greatly reduces the power necessary to generate an observable three-photon absorption signal. One should also note that there may also be some resonance enhancement of the second absorption via the C state of I_2 (81, 85).

Tables 1 and 2 list the transition frequencies and vibrational assignments for the D ← X three-photon absorption in the Rh 640 and Rh 6G spectral regions, respectively. Least squares fitting of the strongest features was employed to arrive at the following set of spectroscopic constants for the D states: $\nu_{00} = 40{,}998$ cm^{-1}, $\omega_0' = 113$ cm^{-1}, and $\omega_0' X_0' = 0.045$ cm^{-1}. These values can be compared to values of ν_{00} 41,200 cm^{-1} (81, 90), and $\omega_0' = 104$ cm^{-1}, $\omega_0' X_0' = 0.2$ cm^{-1} (91). The deviation of the theoretically calculated transition frequencies (Q Branch) are within the resolution (2 Å) of the wavelength measurement for the majority of the spectral features. Since a three-photon

Figure 11. Low resolution (2 Å) three-photon excitation spectrum of I_2 in the Rh 640 dye spectral region
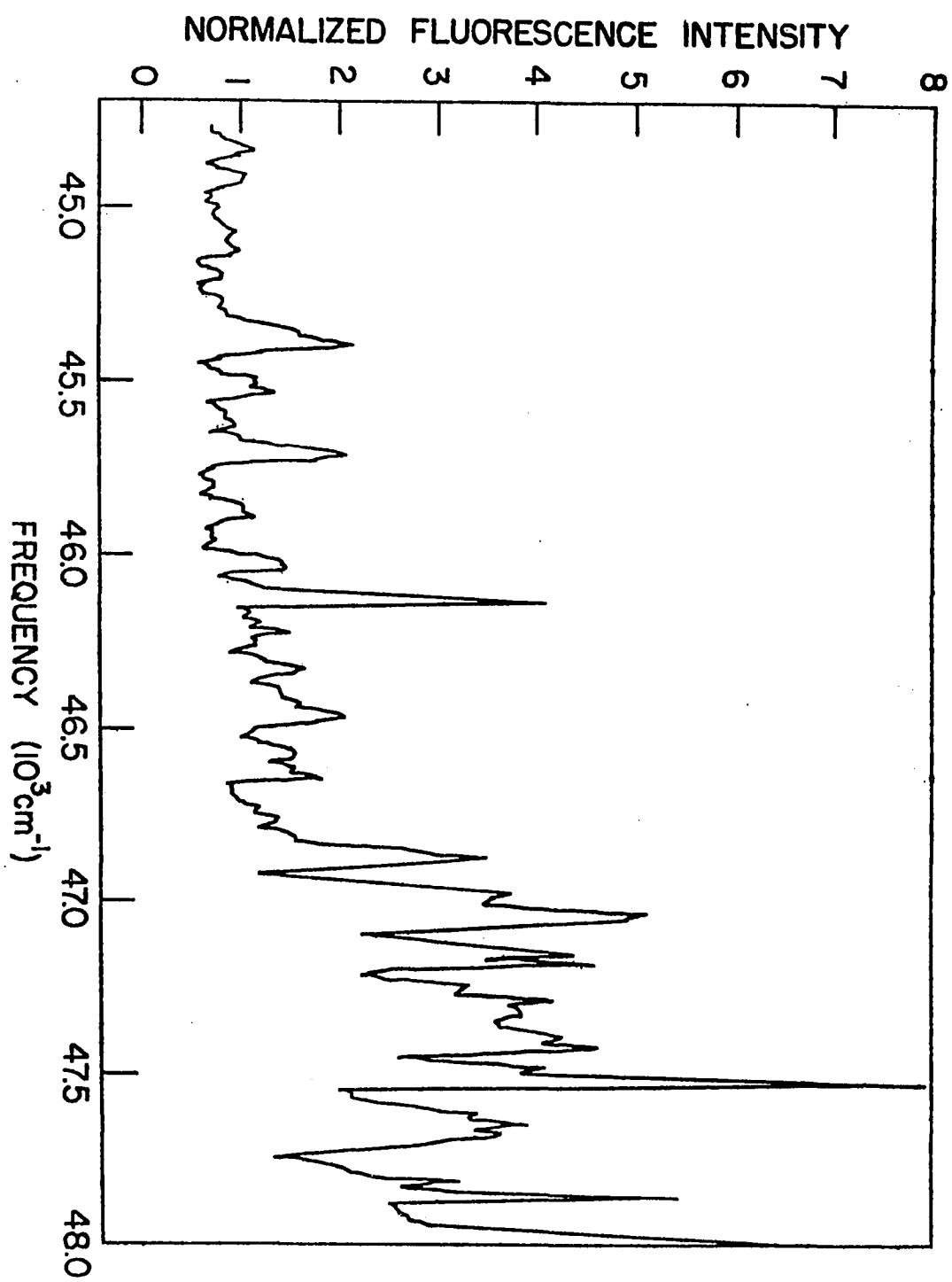
Figure 12. Low resolution (2 Å) three-photon excitation spectrum of I_2 in the Rh 6G dye spectral region
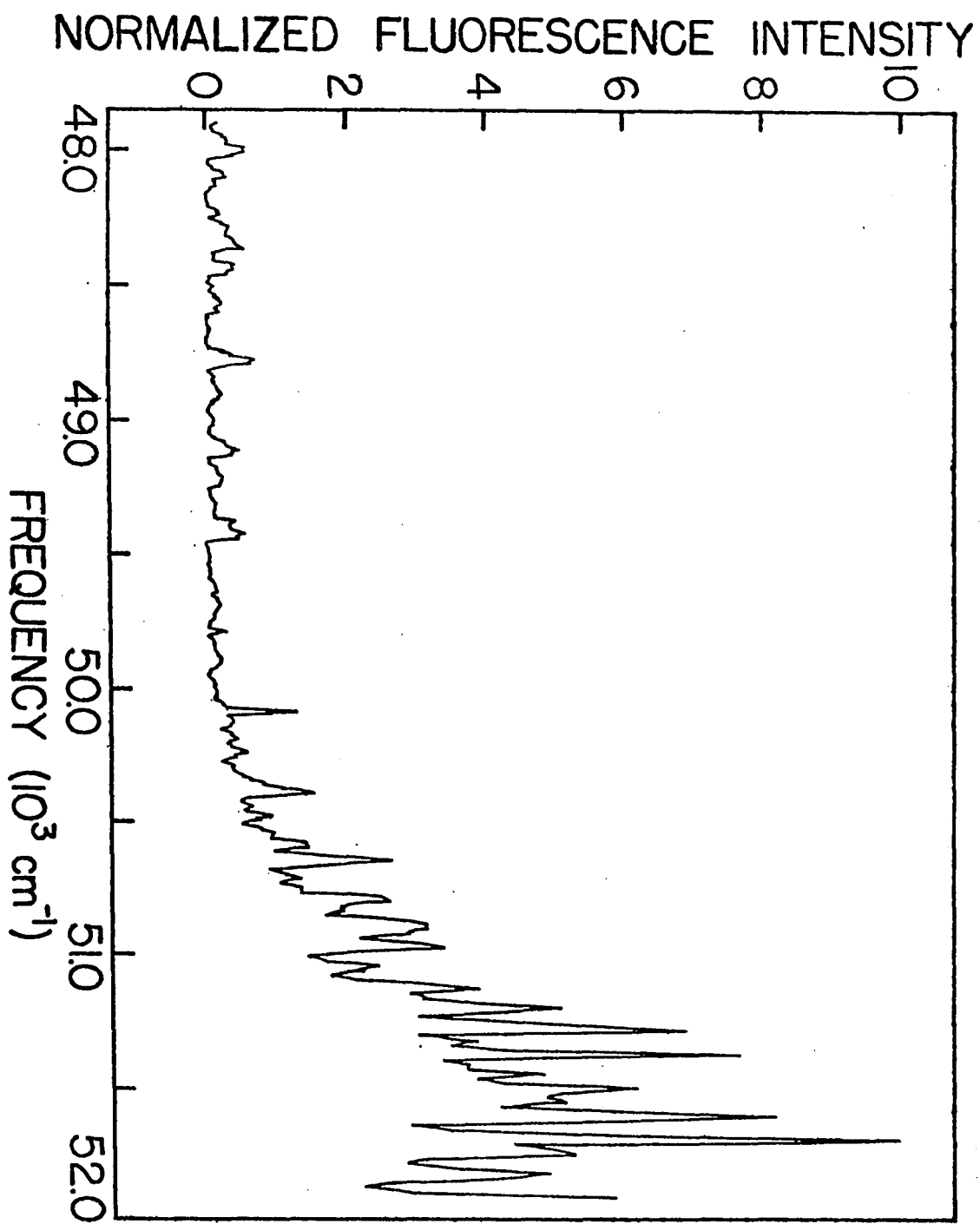
Table 1. Vibrational assignments of I_2 D X three-photon transitions in the Rh 640 spectral region

Frequencies (cm^{-1})	Vibrational quantum numbers			Intensities
	D state	B state	X state	
44813	44	2	5	14
44880	46	4	6	13
45042	44	1	4	12
45096	48	5	6	13
45164	47	4	5	10
45246	50	5	6	10
45370	47	2	4	27
45480	50	4	5	15
45507	52	6	6	17
45604	49	3	4	12
45688	48	1	3	26
45772	51	3	4	9
45870	48	0	2	14
46011	51	2	3	19
46110	54	4	4	52
46166	58	8	6	15
46195	57	6	5	19
46295	52	1	2	21
46438	55	3	3	26
46539	52	0	1	20
46583	60	7	5	20
46612	55	2	2	23
46845	61	6	4	44
46948	56	1	1	47
47007	58	3	2	65

Table 1. (Continued)

Frequencies (cm^{-1})	Vibrational quantum numbers			Intensities
	D state	B state	X state	
47125	61	5	3	55
47155	64	7	4	58
47214	56	0	0	42
47259	66	9	5	52
47304	69	11	6	49
47363	60	2	1	54
47393	62	4	2	58
47453	65	6	3	51
47499	67	8	4	100
47589	60	1	0	42
47619	70	10	5	49
47650	66	7	3	46
47786	65	5	2	40
47832	68	7	3	68

Table 2. Vibrational assignments of I_2 D X three-photon transitions in the Rh 6G spectral region

Frequencies (cm^{-1})	Vibrational quantum numbers			Intensities
	D state	B state	X state	
48001	66	4	1	7
48093	76	14	6	4
48124	71	8	3	3
48233	76	12	5	3
48279	66	3	0	4
48357	69	5	1	7
48420	74	9	3	5
48561	79	13	5	3
48671	70	4	0	2
48766	79	12	4	8
48990	73	5	0	2
49102	80	11	3	6
49215	87	18	6	4
49312	78	8	1	2
49361	76	6	0	5
49410	81	10	2	6
49491	86	14	4	2
49622	91	19	6	3
49672	89	17	5	3
49771	84	11	2	4
49887	93	20	6	3
50070	87	12	2	14
50171	96	21	6	5
50221	95	19	5	7

Table 2. (Continued)

Frequencies (cm^{-1})	Vibrational quantum numbers			Intensities
	D state	B state	X state	
50373	88	11	1	16
50458	87	9	0	10
50526	98	20	5	10
50577	94	16	3	16
50629	88	10	0	27
50697	93	14	2	14
50783	100	21	5	27
50886	99	19	4	32
50956	94	12	1	35
51025	92	11	0	25
51112	95	13	1	40
51182	100	18	3	51
51270	99	16	2	69
51357	97	14	1	77
51428	102	19	3	49
51481	105	21	4	62
51534	101	17	2	52
51587	108	24	5	82
51676	106	22	4	100
51730	105	20	3	53
51801	104	18	2	50

absorption has seven rotational branches (92), the present vibrational assignments are satisfactory.

Since the completion of this work, single frequency ring dye lasers have become available with sufficient power to perhaps allow this experiment to be conducted outside of the laser cavity. This technique would eliminate the problems associated with laser quenching as well as allow for a high resolution study which can resolve rotational structure of the spectrum. Such an experiment can provide better spectroscopic constants and added information on the potential surface of the D state.

Conclusion

In this chapter we have demonstrated the first observation of $D \leftarrow X$ resonance enhanced three-photon absorption of molecular iodine. Three-photon excitation spectra of iodine were presented and vibrational assignments made for all of the major features. With this information, we were able to refine some of the spectroscopic constants for the D state of the iodine molecule. Information of this type could help in the development of new iodine lasers.

PART II. APPLICATION OF DIGITAL IMAGE PROCESSING TECHNIQUES

TO SPATIALLY RESOLVED ABSORPTION SPECTROSCOPY

APPLICATION OF DIGITAL IMAGE PROCESSING TECHNIQUES
TO SPATIALLY RESOLVED ABSORPTION SPECTROSCOPY

Introduction

The ability to make real time species concentration measurements
with good spatial resolution is of fundamental importance to understanding
the dynamics of many physical systems. Optical spectroscopic techniques
of various types are often employed to make these measurements. To this
end, techniques such as atomic and molecular emission (93,94),
absorption (95), fluorescence (96), and scattering (97) have been applied
to study a wide range of systems and problems. These techniques provide
an excellent means for making actual concentration measurements, but their
implementation to systems which require spatial resolution is often quite
tedious. To date, nearly all spatial information is obtained one point at
a time by some sort of rastering mechanism. Aside from being a slow
process, this type of technique is probably fine for studies on systems
which exhibit steady state behavior or, if dynamic in nature, are very
reproducible. If, however, the system under study is not reproducible,
point by point measurements may be of little utility. Such measurements
may provide an average picture of the systems behavior, but this average
may bear little resemblance to individual events.

From this, one can see that it would be useful to have some
diagnostic system that is capable of instantaneous spatial mapping. To
accomplish this, some sort of multidimensional detection device coupled
with an imaging system is required. Devices of this type have been

available for many years in the form of photographic emulsions. Although photographic detection provides simultaneous detection, is low cost, and is available in a number of format sizes, it suffers from a number of problems. Low sensitivity, the requirement of frequent emulsion calibrations and tedious two-dimensional densitometry severely limit its practicality.

Over the last decade, there has been much interest in TV-type multichannel imaging detectors. The primary advantage of the imaging detectors is that they can be readily interfaced to digital computers providing not only simultaneous detection, but also rapid data manipulation. The primary disadvantage of these devices are their limited format size, integration time, and dynamic range. The question which must now be addressed is which of the spectroscopic techniques is most compatible with this type of detector for spatially resolved measurements. Emission is a possibility, but in order to get sufficient depth of field for measurements made on thick systems, high f-number collection optics must be used. This has the effect of greatly reducing the strength of the available signal. Fluorescence and Raman scattering are probably also poor choices since it is difficult to supply sufficient excitation photon flux over a large imaged area to provide a significant signal. Absorption seems to be the best of the available choices, particularly if one uses a tunable dye laser as the primary light source. As an expanded laser beam passes through the system under study, the laser will be absorbed by the species of interest. If one measures the intensity distribution of the laser in the presence and absence of absorbing species, one can determine the

species distribution in the system. The collimated nature of the laser beam not only preserves spatial integrity, but also allows the imaging device to be moved far away from the system under study minimizing the problems associated with stray light. In addition, since we are measuring absorption, there are no stringent requirements on laser power as would be the case for fluorescence or Raman scattering-type measurements.

In this chapter, we will explore the possibility of using a TV-type imaging detector coupled with absorption techniques for making spatially resolved species distribution measurements in a variety of systems. We will give examples of this technique as applied to the mapping of atomic and molecular species in flames as well as atomic species in laser-generated vapor plumes. We will also discuss the applicability of this technique to systems not studied in this work.

Review

Any digital image processor consists of five basic elements: a sampling aperture, scanner, transducer, analog-to-digital converter, and some type of output medium (98). Image processors are divided into two basic categories, scan-in and scan-out. Scan-in processors illuminate only one picture element (pixel) at a time and all of the light is collected for the transducer. Since only one pixel is illuminated at a time, this type of imaging is analogous to obtaining spatial maps by a rastering mechanism. No simultaneous detection is possible with this type of system and it will be discussed no further.

In a scan-out processor, the entire image is illuminated simultaneously and the transducer is allowed to "see" only one pixel at a time. Scan-out processors can be further divided into two categories. The first category includes devices that have no image storage capability and thus cannot be used for simultaneous detection. The various types of image dissector tubes fall into this category. Devices in the second category have image storage capabilities and it is these detectors in which we have the most interest. Included in this category are such devices as vidicons, image isocons and orthocons, and numerous solid-state imaging devices. The choice of which particular device is best suited for a particular application must depend on a number of factors including sensitivity, dynamic range, signal-to-noise ratio, resolution, spectral response and cost. An excellent review of the theory of operation and capabilities of these devices has been presented by Talmi (99) to which the reader is referred for a more complete review. The imaging device used in this study will be a silicon-target vidicon camera.

Digital image processing techniques have been developed to deal with problems in three major categories (100): image digitization and coding, image enhancement and restoration, and image segmentation and description. Over the last few years much has been written about the various aspects of digital image processing. The main emphasis in these publications has been on the mathematical treatment associated with image enhancement and segmentation. These subjects are reviewed in a number of excellent books (98,100,101,102).

Real world applications of digital image processing techniques are widely varied. One area which has received much attention is the field of biomedical image processing. Successful application in this area include white blood cell analysis (103), ultrasound imaging (104), and CAT scanning (105). LANDSTAT type satellites (106) which relay information to earth about such things as land-use, mineral resources, and weather patterns are another useful application of digital image processing technology. Other successful applications include document reproduction (107) and industrial automation (108).

Digital image processing has also found use in spectroscopic applications. One-dimensional image processors have been successfully applied to astronomical studies (109), flame multielement atomic emission (110,111,112) and absorption (113), molecular absorption (114), and picosecond flash photolysis (115). Two-dimensional processors have been coupled with Eschell spectrometers for multielemental analysis (116,117) and with fluorometers for obtaining simultaneous excitation and emission spectra (118).

The first system on which we will demonstrate our diagnostic technique is the laminar flow slot burner common to many atomic absorption instruments. The need for species distribution maps of both natural flame products and species introduced into the flame has been well established in the literature. This information can provide valuable insight into the mechanics of the combustion process as well as the behavior of foreign species introduced into a combustion environment. Papers by Rann and Hambly (119), Chakrabarti et al. (120), and Fassel et al. (121,122)

provide excellent examples of the use of absorption techniques to study the distribution of atomic and molecular species in this type of flame. All of these studies were done using some sort of rastering mechanism to move either the flame or the light source; a tedious process, the need for which we hope to eliminate with our technique.

The second system on which we will demonstrate our diagnostic technique is vapor plumes generated by laser evaporation. When focused on the surface of a sample, absorbed laser radiation will cause the vaporization of a small amount of material. This material has found utility as an analytical sample source. The vapor cloud has been analyzed by a number of different techniques, some of which include emission (93,123,124,125), direct absorption (95,126,127,128), absorption after being swept into a secondary flame source (129), fluorescence (130), and mass spectral analysis (131). The transient nature of these vapor plumes complicates fundamental studies on their formation and decay. We hope that the large amount of data that can be gathered simultaneously by our diagnostic technique may aid in these types of studies.

Experimental

Digital image processor

The digital image processor is made up of three basic elements, the vidicon camera, the image conversion interface (ICI) and the computer. Figure 13 is a schematic diagram of the digital image processor. For this study, we utilized a Cohu Model 4415-200 vidicon camera. This camera has a 525 line/frame, 30 frame/sec, 2:1 interlaced scanning format controlled

Figure 13. Block diagram of the digital image processor
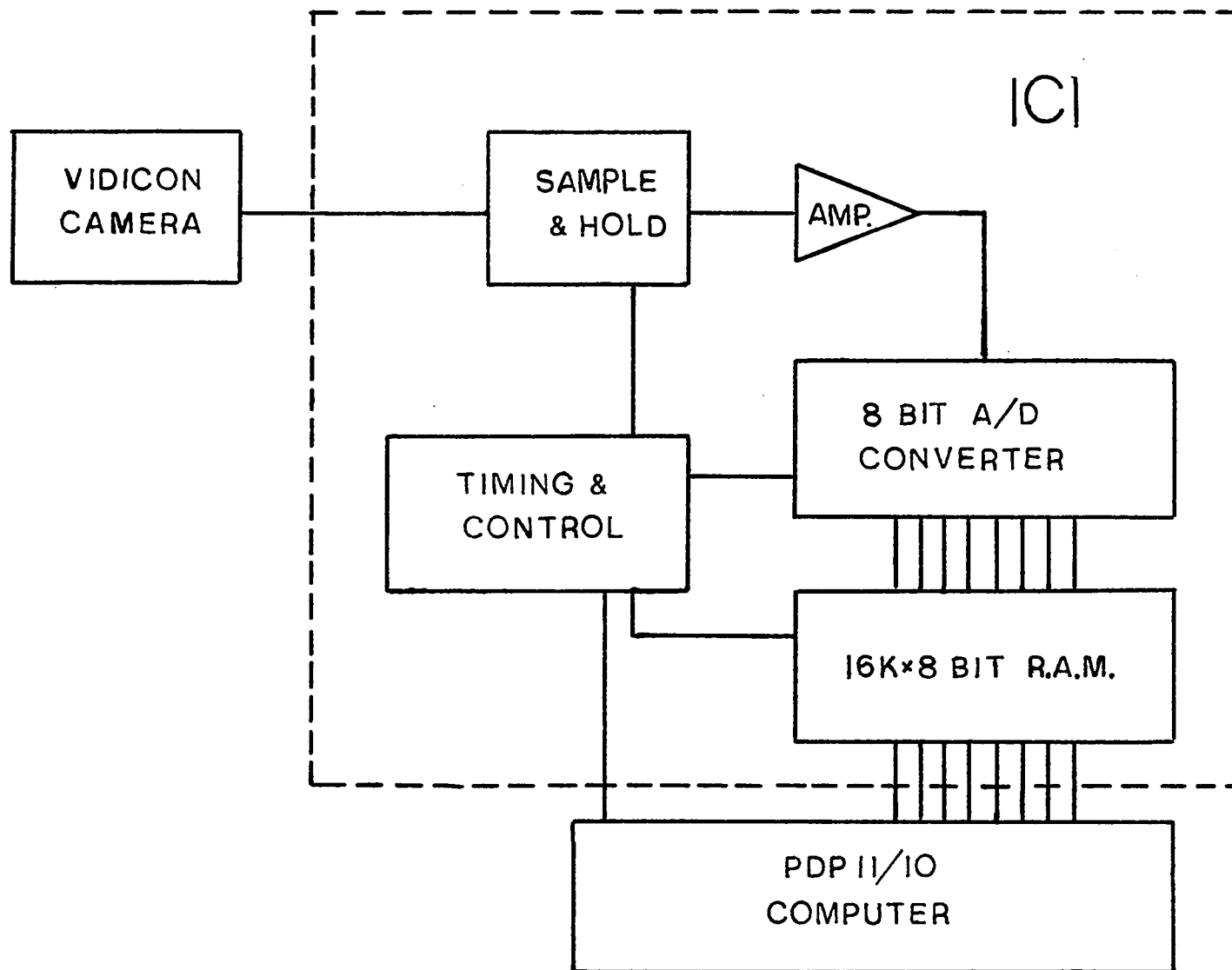
by an internal sync generator. The jumper-selectable automatic sensitivity and black level controls were disabled to prevent these functions from interfering with our measurements. The camera was equipped with an RCA Model 4522H 25 mm silicon-diode array vidicon tube. This high sensitivity vidicon tube is useful from 380-1100 nm and has high resistance to blooming and image burn-in. The active area of the tube measures 10 x 13 mm.

Since the vidicon camera provides an analog output signal, it is necessary to have some means of sampling and digitizing this signal for image storage and processing. This is the function of the ICI. The ICI was designed and constructed in the laboratory in order to provide the versatility required for this work. The timing and control portion of the ICI is responsible for recognizing the beginning of a new frame of data, control over which parts of the frame are to be digitized, and timing of all portions of the circuit. The signal conversion portion consists of three primary devices, a sample and hold to sample the analog video signal, an amplifier to condition the signal, and an analog-to-digital converter to change the analog signal to digital form. In addition, the ICI contains 16K x 8 bits of static random access memory which forms a storage buffer for the image as it is digitized. This buffer is necessary because the computer is not able to store the data as fast as it is digitized by the ICI. Once digitized, the image is transferred to the computer for storage or manipulation.

The computer used in this work was a PDP 11/10 with 28K of memory, laboratory peripheral interface, and dual floppy-disk drive. The image

processor can digitize a 120 x 120 pixel image with gray scale resolution of 256 levels in 16 msec. Transfer of this image to the computer takes approximately 0.5 sec. Since the vidicon camera is an integrating device, all image data are recorded simultaneously. The vidicon may be illuminated continuously if one wishes to make time averaged measurements, or in a pulsed fashion if time resolution of the image is required. The only limit on the time resolution attainable is the width of the light pulse.

A complete description of the digital image processor is given in Appendix A. This appendix contains detailed circuit and timing diagrams as well as a description of the operation of each portion of the image processor.

Diagnostics of laminar flow slot burners

In order to test the operation of our digital image processor, the first system that we studied was a premixed slot burner of the type common to many atomic absorption instruments. Besides offering a long absorption path, this type of burner has simple geometry and a non-turbulent flame which makes it an ideal demonstration case.

The experimental apparatus used for this study is shown schmatically in Figure 14. A Control Model 554A Ar^+ laser was used to pump a Spectra Physics Model 375 continuous wave tunable dye laser. The output of the dye laser was passed through a 15 cm focal length lens L1. The dye laser beam was directed by mirrors M1 and M2 to a 2 mm pin hole which blocked all but the central portion of the diverging dye laser beam. The portion of the dye laser beam which passed through the pin hole was then expanded to a diameter of 25 mm by lenses L2 and L3 after which it passed along

Figure 14. Experimental arrangement used for flame diagnostics
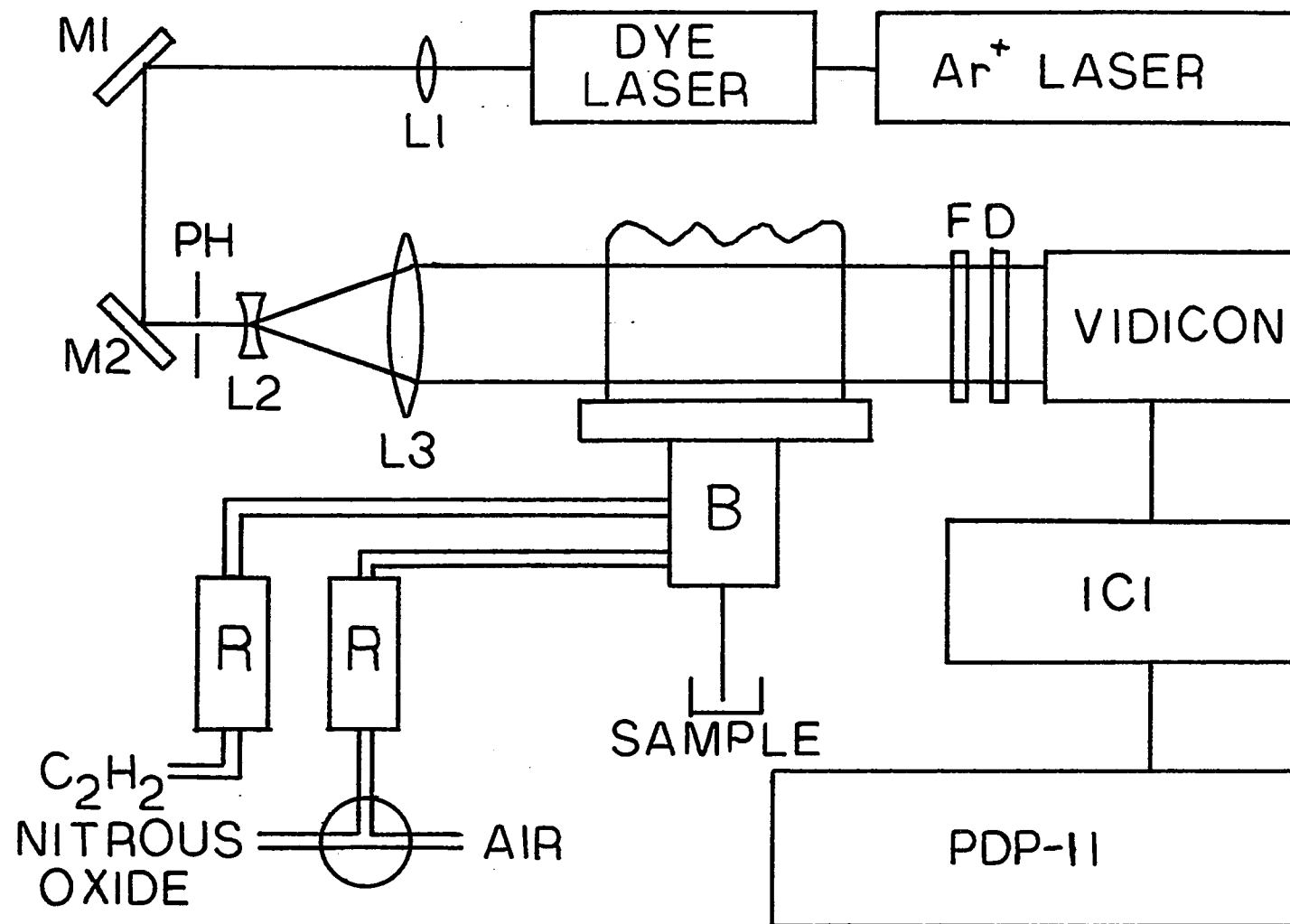
the surface of the burner parallel to the long axis of the burner. The laser beam then passed through a filter (F) which served to block background radiation from the flame and struck an opal glass diffuser (D). The lens of the vidicon camera collected the light scattered by the diffuser and created a 1:1 image of the diffuser on the surface of the vidicon tube. The diffuser was placed in front of the vidicon to destroy the coherence of the laser beam. This helps to eliminate interference effects which can occur when narrow band coherent light shines on an imaging tube. The slot burner used was a Varian Techtron burner with burner heads for both nitrous oxide-acetylene and air-acetylene flames. Rotameter type flow meters were used to measure the flow rates of both fuel and oxidant.

Flame maps were obtained in the following manner. First, the slot burner was ignited with whatever fuel mixture was to be used for the particular experiment. The analyte solution was then aspirated into the flame and the dye laser was tuned to resonance with the particular atomic or molecular absorption line to be studied. This was easily done by monitoring the output of the vidicon camera on an oscilloscope; a decrease in signal strength indicates an absorption. Once the laser was tuned on resonance with the absorption line of interest, the computer program PTAKE was used to digitize as many frames of data as desired (usually 50 frames for these flame studies). The analyte was then removed from the flame and the burner rinsed with distilled water. A sample blank was then aspirated into the flame and the same number of frames were again digitized, this time in the absence of the absorbing species. The

computer program FCON was used to convert the two data files representing

I and I_0, respectively, to a file containing the absorption image of the

flame. The program PSMO was used to smooth the absorbance file when

desired. Programs PSPOT and PGRPH were used to generate absorbance contour

plots for display on an oscilloscope or X-Y recorder, respectively.

Appendix B contains listings of all the source programs used in these

experiments along with an explanation of all the interactive responses

required for their operation.

Diagnostics of laser generated vapor plumes

Vapor plumes generated by laser vaporization represent an excellent

test of the applicability of our diagnostic technique to the study of

rapidly transient species. The experimental apparatus used for this

experiment is shown schematically in Figure 15. The laser used for vapor-

ization of the sample was a Phase-R Model DL-2100C coaxial flashlamp pumped

dye laser. The dye solution used was 6×10^{-5} M Rh 640 in absolute ethanol.

The maximum energy for the 800 nsec output pulse was 0.1 J. The laser

pulse was reflected by mirror M3 and focused on to the surface of the

sample by lens L3 which has a focal length of 5 cm. The sample cell was

constructed from an aluminum block with dimensions of 2.5 x 2.5 x 3.0 in.

The focusing lens was mounted on one end of the cell and the sample was

introduced from the other end of the cell on a 0.75 in diameter rod which

could be rotated to expose a new sample surface for vaporization. Two

1.0 in diameter antireflection coated windows were mounted on opposite

Figure 15. Experimental arrangement for laser generated vapor

plume diagnostics
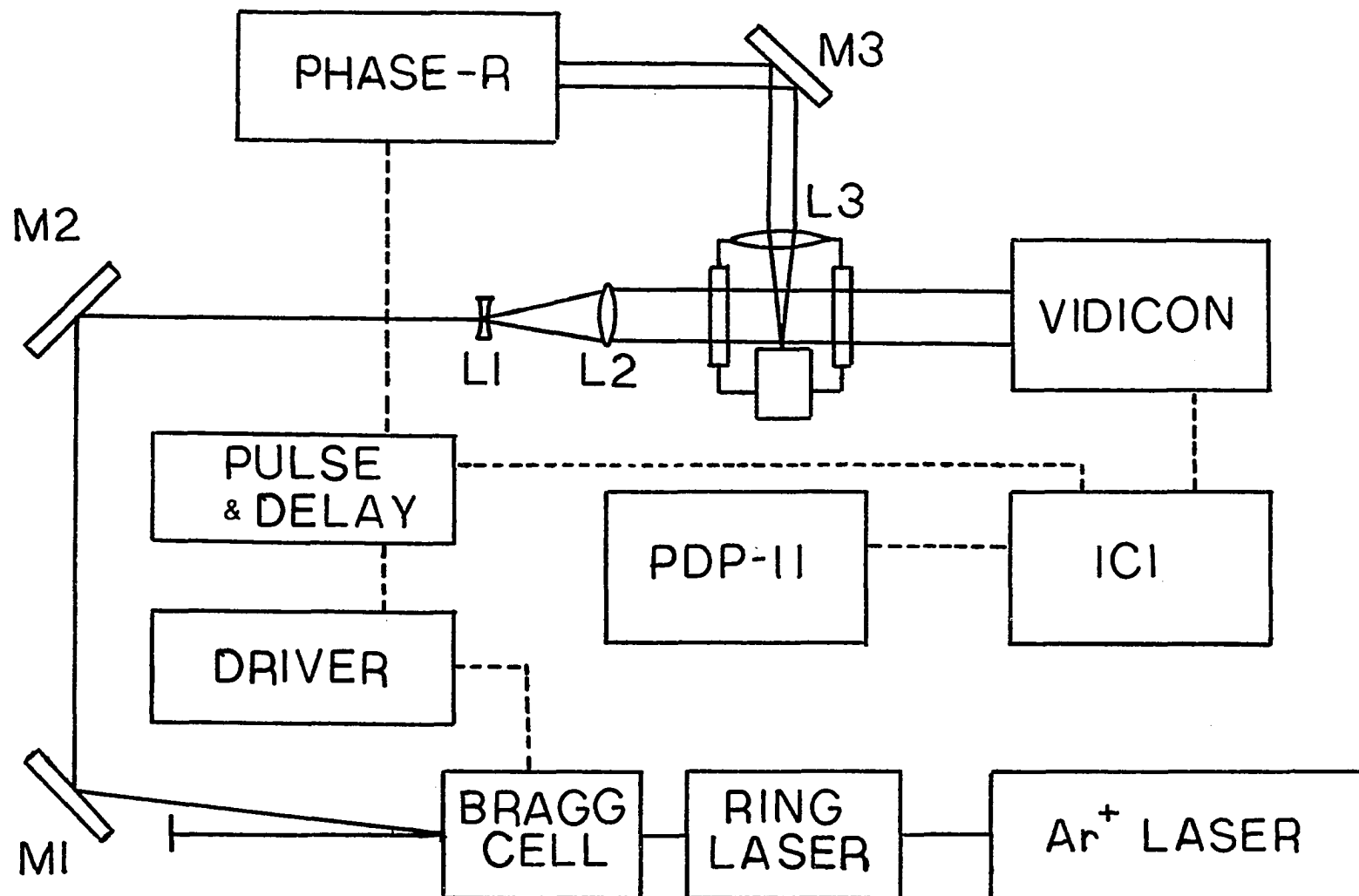
sides of the cell block perpendicular to the sample surface. The entire cell could be evacuated to 10^{-3} torr.

Since the vapor plume generated by the pulsed laser was a transient species, it was necessary to pulse the probe laser to obtain space-time profiles of these plumes. The probe laser was a Spectra-Physics Model 580A single frequency ring dye laser pumped by a Control Model 554A Ar^+ laser. This dye laser was capable of output powers on the order of 500 mW using 4 W of pump laser power. The probe laser had frequency stability of 40 MHz peak-to-peak. The output of this probe dye laser was gated on and off by a Coherent Associates Model 304 Bragg cell and Model 305D Bragg cell driver. When gated off, all of the radiation from the ring laser was diffracted into zeroth order by the Bragg cell and blocked by a beam catcher. When gated on, the Bragg cell diffracted approximately 70% of the output radiation into first order which was then directed to the rest of the experiment by mirrors M1 and M2. After being expanded to a diameter of 50 mm by lenses L1 and L2, the output of the ring laser passed through the sample cell across the surface of the sample. After passing out of the sample cell, the laser passed through a filter used to block stray light and onto the surface of the vidicon tube.

A laboratory constructed pulse and delay generator was used to control the pulse width of the probe laser as well as the delay between the vaporization pulse and the probe pulse. The width of the probe laser pulse was adjustable from 0 to 140 μsec, and the delay from 0 to 1.2 msec.

Appendix A contains construction details and calibration curves for the pulse and delay generator.

Vapor plume maps were obtained in the following manner. First, the sample is attached to the end of the sample holder rod with double-sided adhesive tape and inserted into the sample cell. The probe laser was tuned to absorption resonance by aspirating a solution of the analyte species into a flame placed in the probe beam and tuning the laser until visible laser excited fluorescence was observed in the flame. The power of the probe laser and width of the probe pulse were then adjusted to expose the vidicon tube to near saturation over the entire surface of the tube. After setting the desired delay, two frames of data are digitized, one with the production of a vapor plume and one without. These frames of data represent I and I_0, respectively. The computer program PCON is used to convert these two frames of data to an absorbance image of the vapor plume at the specified time delay. The computer program PSMO was used to smooth the absorbance file when desired. Programs PSPOT and PGRPH were used to generate absorbance contour maps for display on an oscilloscope or X-Y recorder, respectively.

Results and Discussion

In order to properly evaluate the utility of a new diagnostic technique, it is necessary to measure important performance parameters of the diagnostic instrument itself. One problem associated with vidicon cameras is limited dynamic range. This problem can be particularly troublesome when applied to emission experiments where signals can vary

over several orders of magnitude. Since our diagnostic system measures absorbance, the vidicon need not have a dynamic range of much over ten for most applications. Figure 16 shows an absorbance linearity curve for our digital image processor. This linearity curve was obtained by inserting calibrated neutral density filters in front of the vidicon camera. Figure 16 shows excellent linearity up to absorbance values of 1.5. Such linearity should be sufficient for studies on all but the most optically dense systems.

Conventional absorption instruments contain lock-in detection systems which enable them to discriminate against flame background. Lock-in detection is not possible with our detection system, so it might be expected that flame background would be a problem. The collimated nature of the laser allows the vidicon camera to be moved far away from the flame source, thus greatly reducing the amount of flame background radiation that reaches the camera. In addition, the high intensity of the laser allows the camera aperature to be nearly closed, further reducing the amount of collected stray light. It was found that by simply placing a narrow-line filter in front of the camera, the flame background from even the most luminous flames was undetectable by the vidicon camera. In light of these results, flame background radiation is not considered as great a problem as might have been expected.

A vidicon camera with an uncooled tube provides an inherently noisy output signal. This noise propagates through the data treatment to the final absorbance maps. Figure 17 shows four flame contour maps. The raw data absorbance map shows a considerable amount of noise. The other

Figure 16. Absorbance linearity curve for the digital image
processor
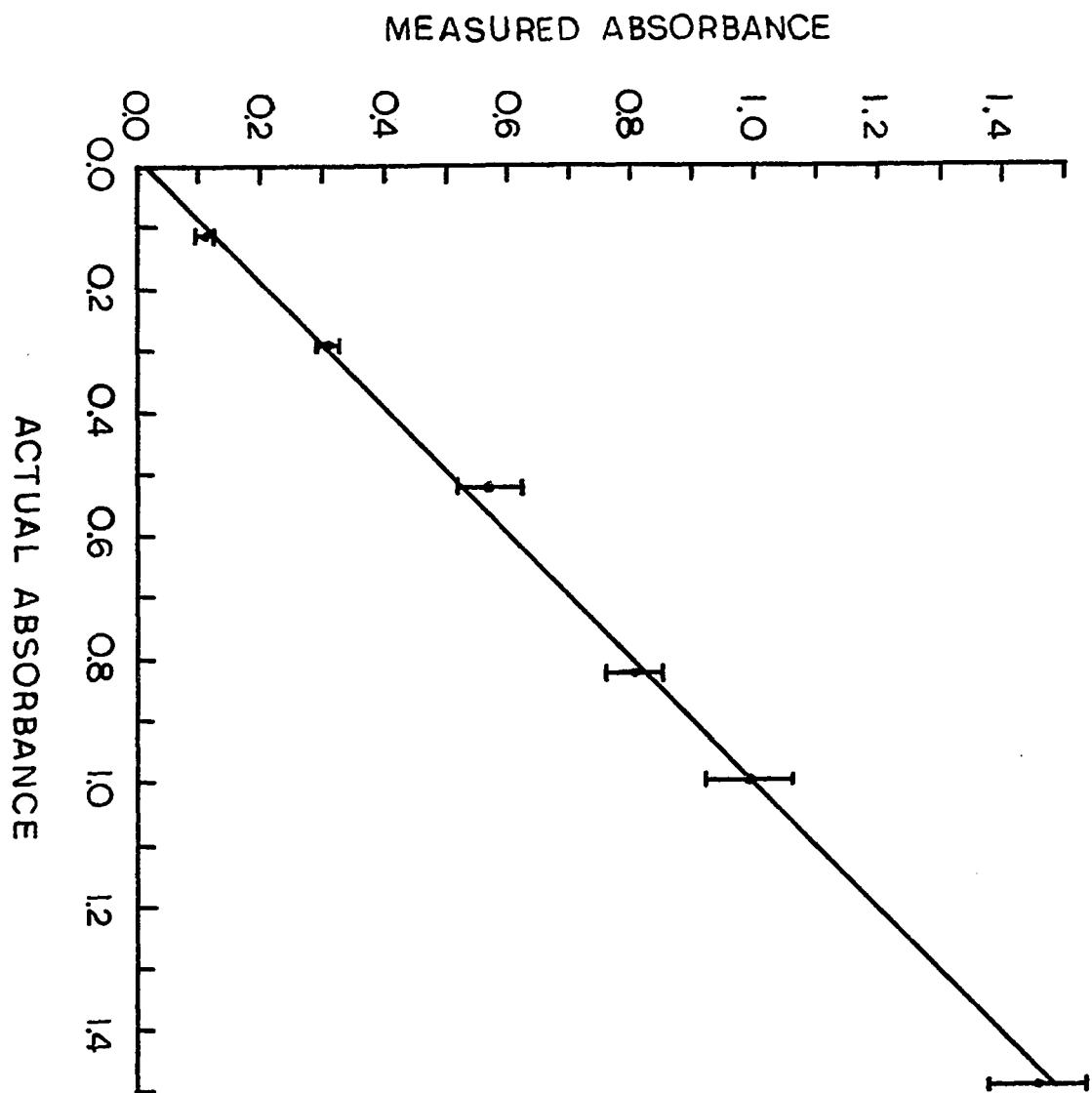
three absorbance maps were generated after smoothing the raw absorbance data with the computer program PSMO. Examples of 5, 7, and 9 point data smooths are shown. As can be seen in Figure 17, the most dramatic improvement in noise level is between the raw absorbance map and the 5 point smoothed map. The 7 and 9 point smoothed maps provide little improvement over the 5 point smoothed map. It can also be seen that the smoothing routine, while doing an excellent job in removing noise spikes, does not change the shape of the actual absorbance contours. All the absorbance contours shown in this chapter have been treated with a 5 point data smooth to provide better definition.

The first system on which we demonstrated the utility of our diagnostic technique was the laminar flow slot burner. Due to wavelength constraints imposed by the dye laser, we were unable to do any species distribution studies on natural products of the flame. Our studies were therefore directed toward obtaining absorbance maps of atomic and molecular species in salted flames. Our first experiments involved measurement of the distribution of two stable monoxide species, YO and ScO, in flames under a variety of conditions. The absorption spectra of these species in flames was first reported by Fiorino et al. (132). Yttrium, scandium, and many other elements have been shown to form very stable monoxide species in flames. The formation of these species is known to be very dependent upon the stoichiometry of the flame (121). We, therefore, thought that these systems would be an excellent choice with which to demonstrate our diagnostic technique.

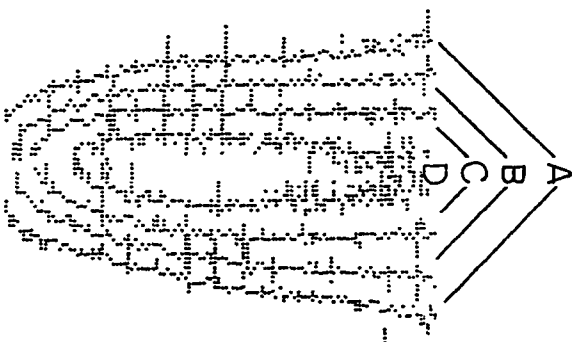Figure 17. Effect of smoothing function on flame contour maps

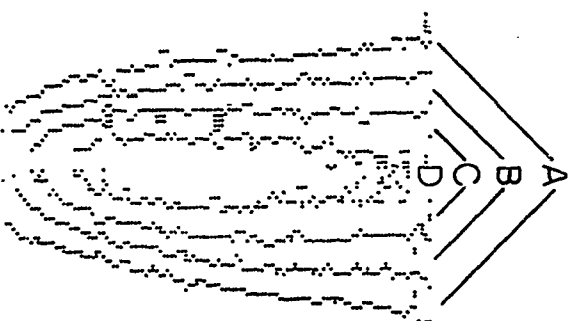   A -- 0.1 absorbance units

                    B -- 0.2 absorbance units
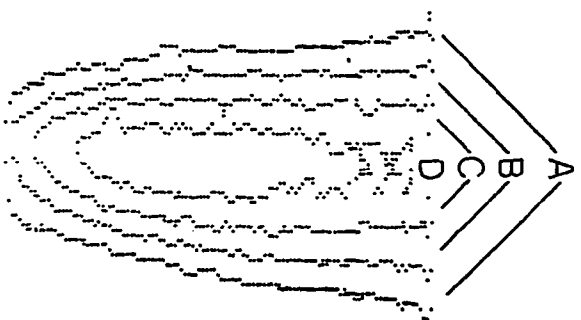
                    C -- 0.3 absorbance units

                    D -- 0.4 absorbance units

raw data

7 pt.

5 pt.

9 pt.

Figure 18 shows absorbance contour maps of ScO and YO at 6036.2Å

and 5972.2Å, respectively, in a nitrous oxide-acetylene flame. Comparing

the contours of the fuel-rich and fuel-lean flames, it is apparent that

the fuel-lean environment is much more conducive to metal monoxide

formation than is the fuel-rich environment. This effect has been

attributed to two mechanisms operating in the flame. First, in a fuel-

rich environment, the excess carbon containing radicals and hydrogen

scavenge the available oxygen in the system because their reaction is

exothermic. This reduces the oxygen available for metal monoxide

formation. Secondly, direct chemical reduction of the metal monoxide by

the excess carbon available in a fuel-rich environment reduces the

concentration of metal monoxide (121).

If the first of these two mechanisms is valid, then the introduction

of any species into the flame that will act as an oxygen scavenger will

tend to lower the concentration of metal monoxide in the flame. To test

this hypothesis, we once again obtained absorbance maps of ScO and YO in

fuel-lean nitrous oxide-acetylene flames, after which each of the sample

solutions was doped with an equal amount of the other element. Absor-

bance maps were then obtained while aspirating the doped solutions into

the flame. If the hypothesis is to hold, one would expect to see a

reduction in metal monoxide absorption at the appropriate wavelengths due

to competition for the available oxygen by the dopant species. Figure 19

shows the results of this experiment. The top two flame maps indicate YO

absorption and the bottom two indicate ScO absorption. In the maps on

left, only the species being measured was aspirated into the flame, on

Figure 18. Effect of flame stoichiometry on flame absorbance maps
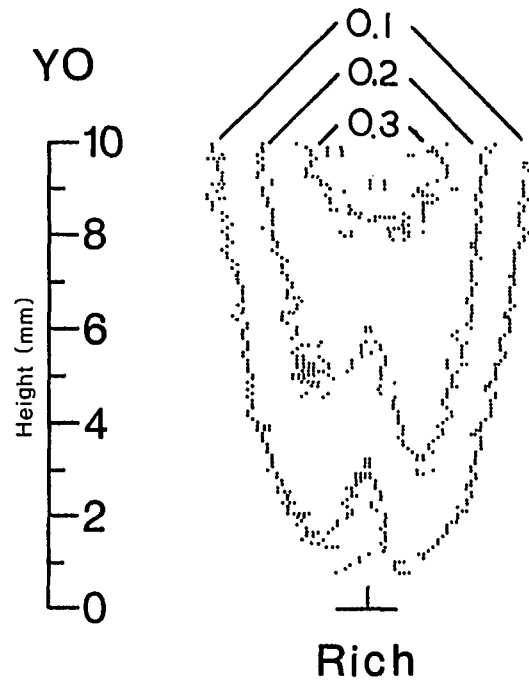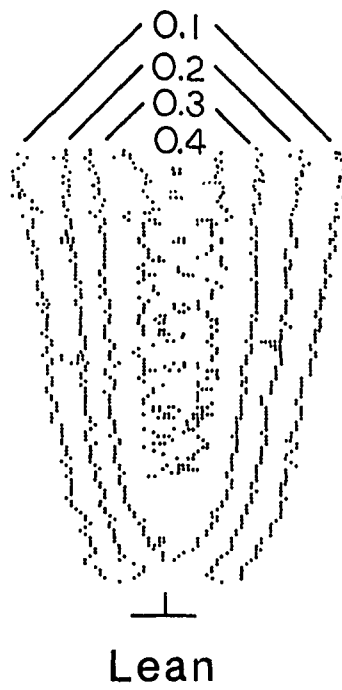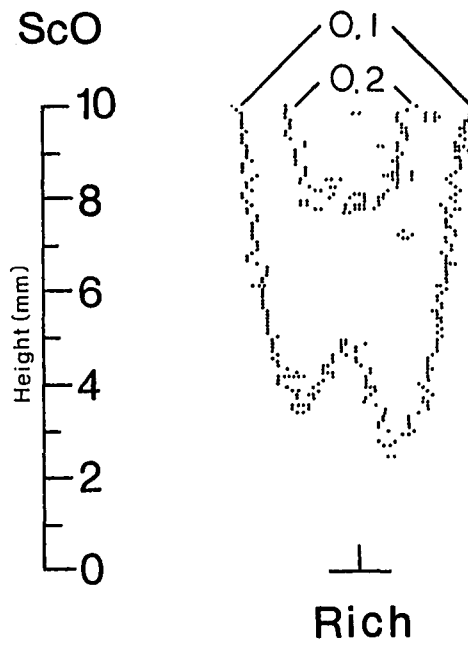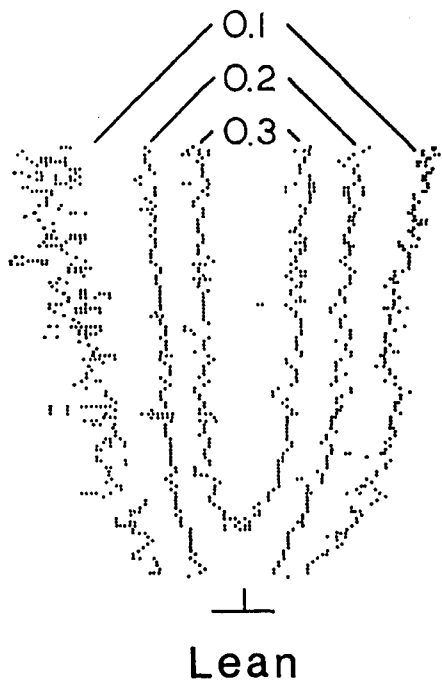of ScO and YO

Figure 19. Effect of added oxygen scavengers on the flame maps

of ScO and YO
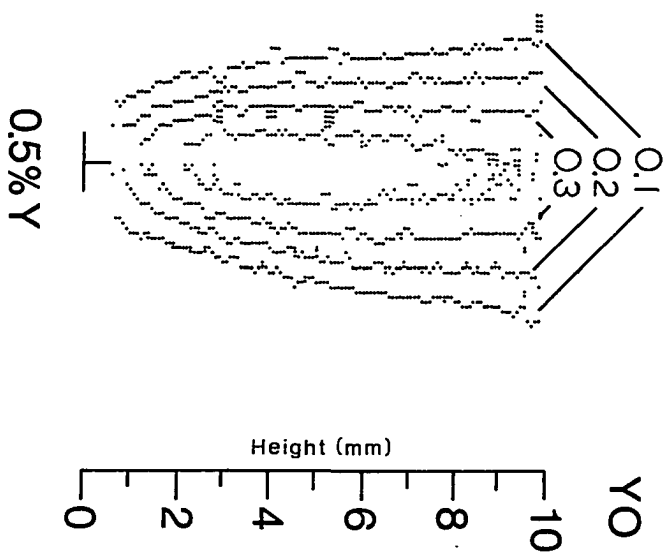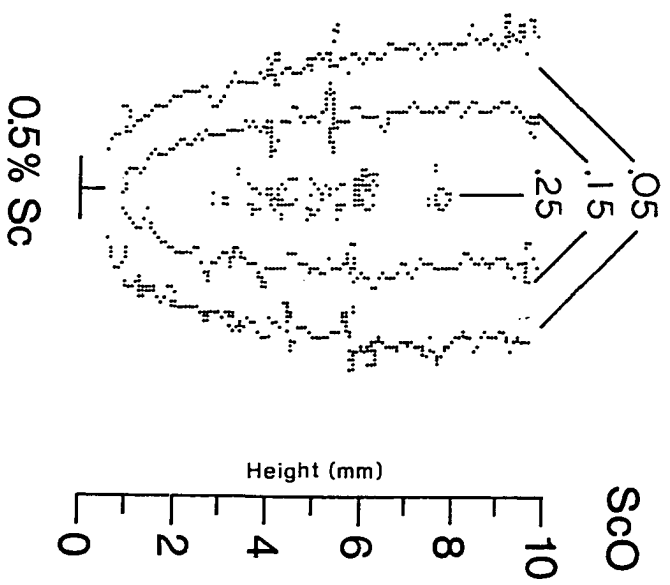
the right, the doped solutions were aspirated into the flame. It is obvious from Figure 19 that the expected effect was indeed observed. The two frames on the right in Figure 19 definitely show lower absorbances than do the two frames on the left.

A technique which is sometimes used to prevent the formation of metal monoxides or hydroxides in a flame is to complex the analyte with some organic complexing agent. These chelates form strong complexes with the metal atom preventing it from reacting with other species in the flame. Combustion of the organic chelate forms a localized fuel-rich environment around the metal atom, further inhibiting metal monoxide formation. This phenomenon is illustrated in Figure 20. The flame map on the left indicates the ScO distribution in a fuel-lean air-acetylene flame when aspirating a solution containing Sc. The map on the right illustrates the ScO distribution when a solution of Sc complexed with EDTA is aspirated into the same flame. One can see that there is little, if any, ScO present in this region of the flame when the Sc chelate is aspirated into the flame.

Another subject on which we will demonstrate our diagnostic system is the problem of molecular interference in atomic absorption spectroscopy. A good example of this phenomenon is the interference of CaOH absorption in atomic absorption measurements on barium at 5536 Å. This interference has been studied by Billings (133) and Koirtyohann and Pickett (134). Koirtyohann and Pickett report that the absorption observed from a 1% solution of CaCl is about the same as what would be expected from a 75 ppm solution of barium. The question now posed is

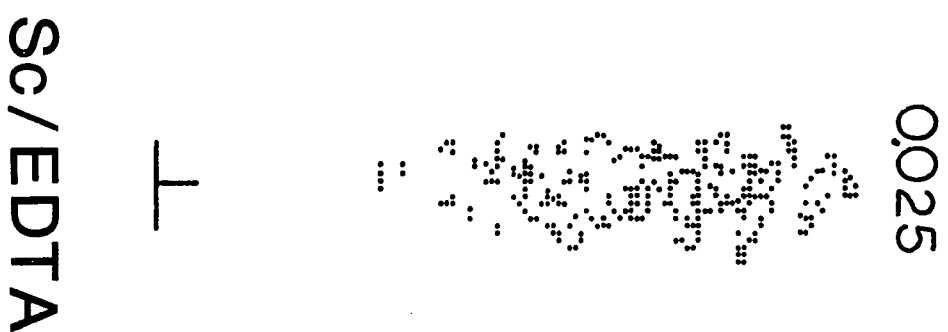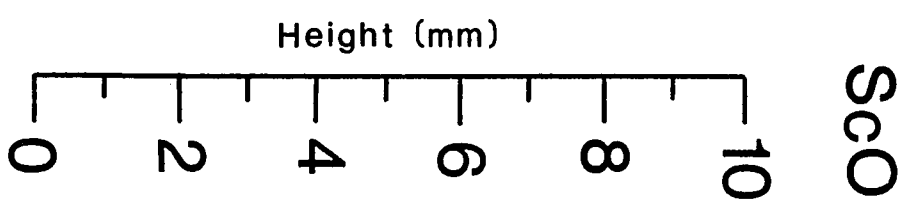Figure 20. Effect of a chelating agent on the flame absorbance map
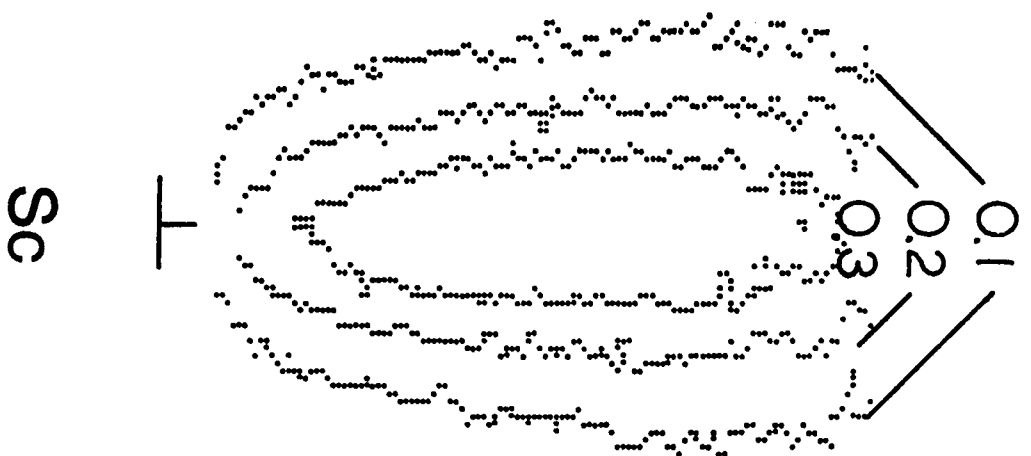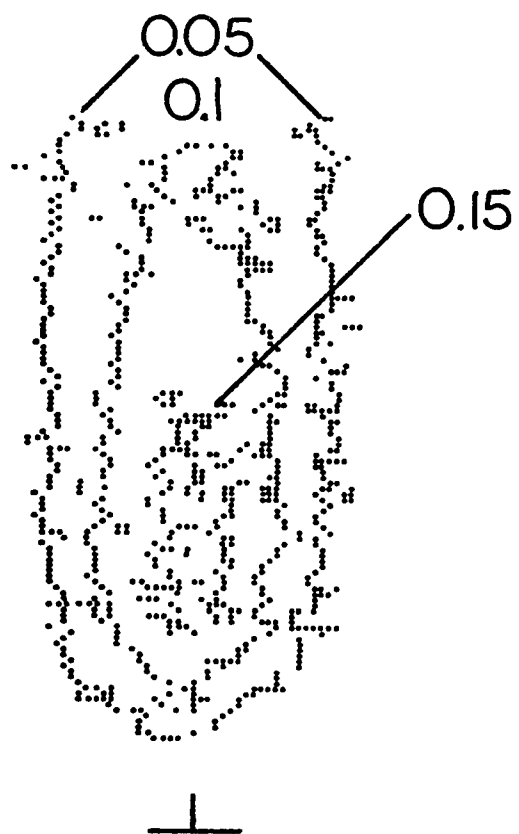
of ScO

Sc

0.1
0.2
0.3
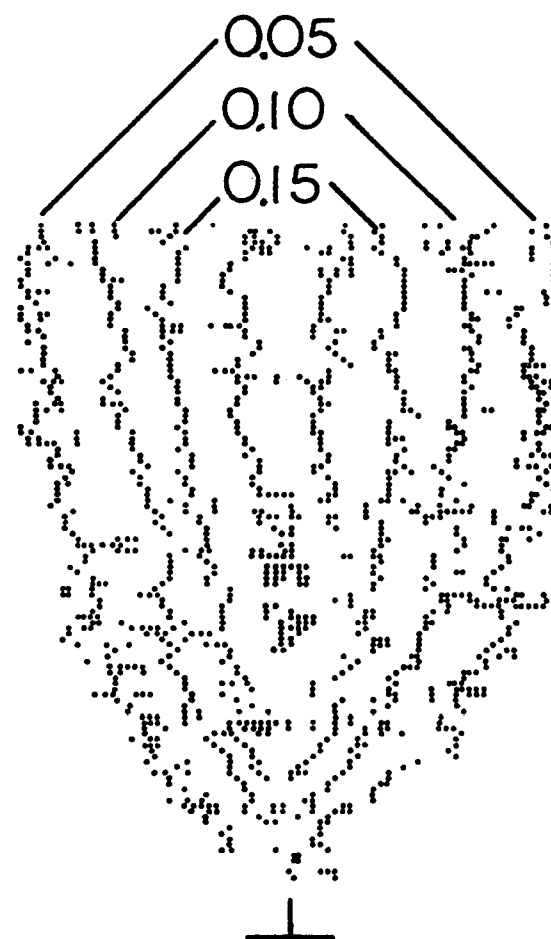
ScO

Height (mm)

10
8
6
4
2
0

Sc/EDTA

0.025

Figure 21. Absorbance maps of Ba and CaOH at 5536 Å in an air-
acetylene flame

5536Å

Ba

CaOH

Height (mm)

where in the flame does this relationship hold true. In order to deter-
mine if there is an optimum position in the flame to measure barium
absorption while minimizing the interference from CaOH absorption, we
obtained flame maps for both species in an air-acetylene flame. The CaOH
map was obtained by aspirating a 1% solution of CaOH into the flame and
the Ba map was obtained by aspirating a 75 ppm solution of BaCl. These
two flame maps are shown in Figure 21. From Figure 21, it appears that
the optimum position to look in the flame to minimize CaOH interference
is about 3-4 mm above the burner head. The region of maximum CaOH
absorption appears to be higher in the flame than is the region of
maximum Ba absorption. As reported, solutions of 1% Ca and 75 ppm Ba
have approximately equal absorbances. The absorbance values shown for Ba
in Figure 21 are probably lower than the actual absorbance values because
of the width of the laser output frequency.

Although systems such as the laminar flow slot burner can be easily
studied by our diagnostic system, they are steady state in nature and
thus do not take full advantage of its power. The real advantage of our
diagnostic technique over rastering techniques lies in the fact that we
are able to make simultaneous measurements from all points to be
measured. This is of particular advantage when studying transient
species. One such system to which we will apply our technique are vapor
plumes generated by laser evaporation. The measurement of plume for-
mation and decay has been undertaken to one extent or another by a
number of groups. Three basic techniques have been used for these
studies. They include atomic absorption (95,128), emission (135,136),
and photography (137,138).

Photography has the advantage, as does our diagnostic system, of being able to record data from all points in the plume simultaneously. The photographic studies, however, have taken pictures of the plume using the luminosity of the plume as the light source for the plume. A number of things contribute to this luminosity, including atomic and molecular emission as well as black-body radiation. Photographic detection therefore provides only information about the bulk of the plume, but provides no information about the distribution of specific species in the plume. Emission and atomic absorption studies have been done by probing one small region of the vapor plume at a time and rastering either the plume or light beam position. Although these techniques are element specific, they provide only an average picture of what is happening spatially in individual plumes.

In order to test the applicability of our diagnostic technique on vapor plume systems, we constructed a laser vaporization system as described in the experimental section of this chapter. Again, due to wavelength constraints imposed by our probe dye laser, we were somewhat limited as to the choice of elemental system to study. We choose to use sodium samples since the sodium D line absorption lies in a very efficient region for our probe laser, 5890 Å. For most of our studies, we used a fresh sodium target transferred to the sample chamber under nitrogen dry box conditions. In order to obtain sufficient illumination of the vidicon camera, a probe pulse of 50 μsec was required. This placed a 50 μsec time resolution limit on any of our measurements.

The first task was to determine the experimental conditions under-which plume formation could be monitored. Argon was used as an inert atmosphere over the sample. The argon pressure was varied from 10^{-1} torr to 1000 torr and plume absorption measurements were taken at a series of time delays following plume formation. An argon pressure of 500 torr was found to confine a structured plume to time delays of approximately 1.5 msec after plume formation.

Figure 22 shows a time lapse sequence of the formation of a sodium vapor plume (generated by a 0.1 J 800 nsec laser pulse) under a 500 torr argon atmosphere. The imaged area in each frame measures 10 x 13 mm. The contour gradient in these plumes is sufficiently steep that the individual contours must be shown in separate frames in order to resolve the contour levels. Contours in columns 1, 2, and 3 are drawn at absor-bance values of 0.05, 0.10, and 0.15, respectively. Contours in rows A, B, C, D, and E represent time delays of 0.2, 0.4, 0.6, 0.8, and 1.0 msec, respectively. Within a single row, all frames are taken from a single vapor plume. Each individual row, however, represents a new vapor plume.

Certain trends in plume formation can be seen in Figure 22. As one looks at longer and longer time delays, the region of maximum absorption moves farther and farther away from the sample surface (denoted by the heavy line) with the exception of row E. This anomaly is simply a function of experimental variation and was not observed in other sequences taken under the same conditions. Another effect that is seen in Figure 22 is that all the vapor plumes tend to adopt some sort of

Figure 22. Time lapse sequence of the formation of a sodium vapor
plume under a 500 torr Ar atmosphere

Column	Absorbance		Row	Time Delay
1	0.05		A	0.2 msec
2	0.10		B	0.4 msec
3	0.15		C	0.6 msec
			D	0.8 msec
			E	0.9 msec
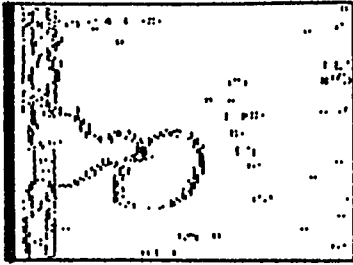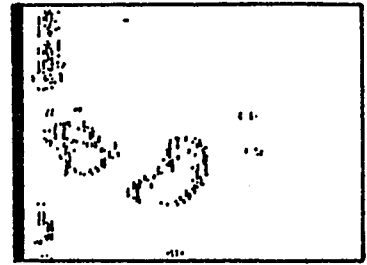
A 1   A 2   A 3
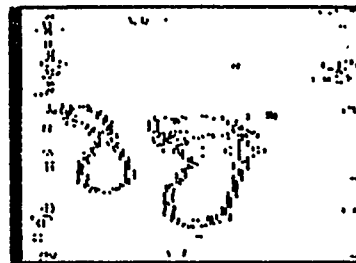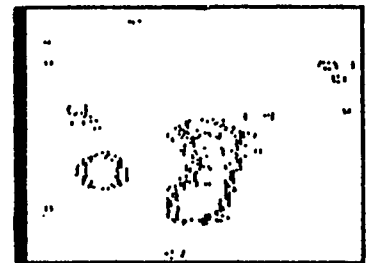
B 1   B 2   B 3
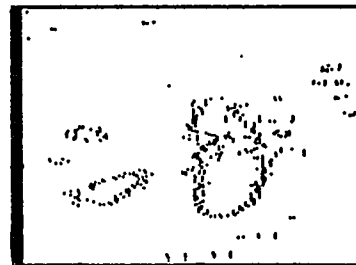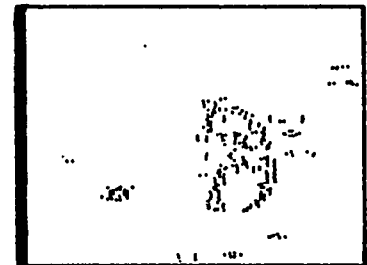
C 1   C 2   C 3
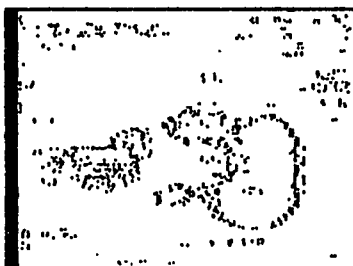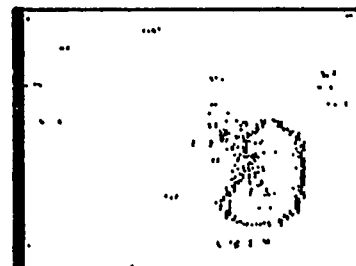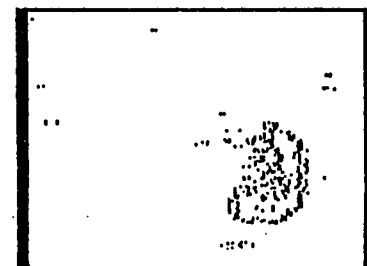
D 1   D 2   D 3
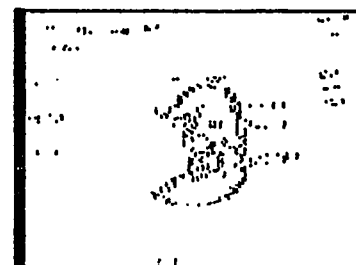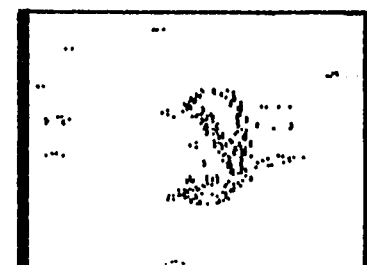
E 1   E 2   E 3

mushroom or filamented shape. Although certain average trends are
evident in Figure 22, it is obvious that there is a large amount of plume-
to-plume variation which may not be realized by conventional rastering
techniques. As one lowers the pressure of the argon buffer gas, the
plume is observed to be less confined and expand more rapidly. By
lowering the Ar pressure to 100 torr, a structured vapor plume could only
be measured to time delays of 0.3-0.4 msec as contrasted to delays of
greater than 1 msec for plumes formed at 500 torr. Figure 23 shows a
comparison of two representative vapor plumes, one created at 500 torr
and the other at 100 torr take 0.2 msec after the vaporization pulse.
One can see from this figure that the plume formed at 100 torr is some-
what larger and shows less structure than the plume formed at 500 torr.
Vapor plumes formed under vacuum conditions could not be mapped with our
system in its present configuration since the plume expands so rapidly
that all structure disappeared during the 50 µsec required to make a
measurement even with no additional delay.

It was noted in these studies that there was quite a bit of plume-
to-plume variation as different regions of the sodium sample were
vaporized. It was initially thought that the difficulty in obtaining a
uniform sodium surface was the cause of the problem. In an attempt to
solve this problem, we tried using a polished single crystal $Na_{0.7}WO_3$
sample in the hope that it would provide a more uniform plume. After
obtaining plume maps from this sample, it was found that this sample did
not provide any appreciable improvement over the fresh sodium sample. At
this point, it is believed that the most likely cause of the observed

Figure 23. Comparison of vapor plumes generated at 500 torr and 100 torr after 0.2 msec delay, absorbance level 0.05
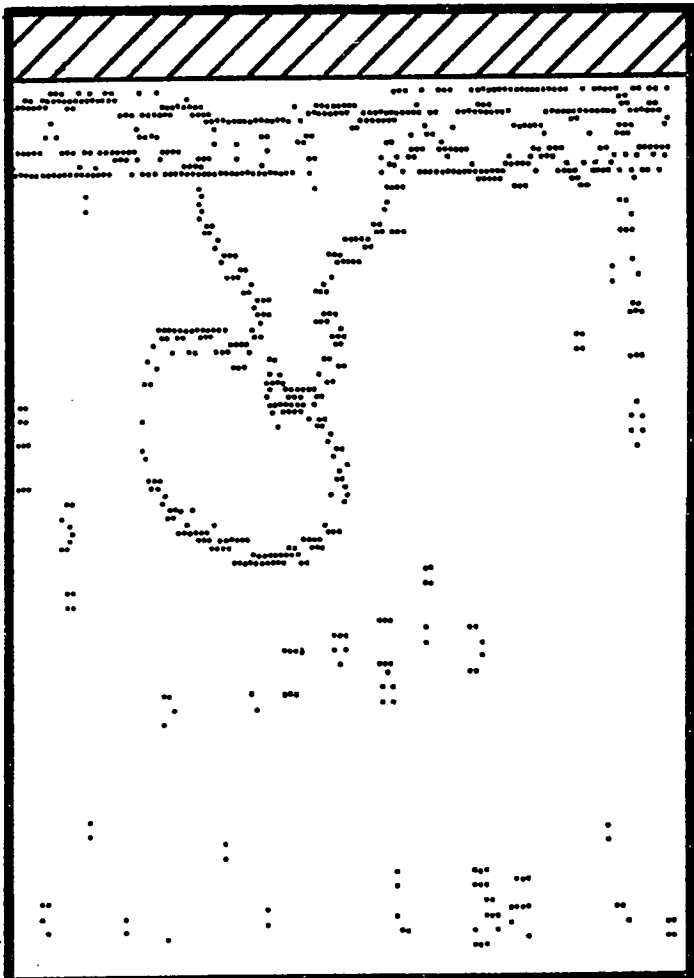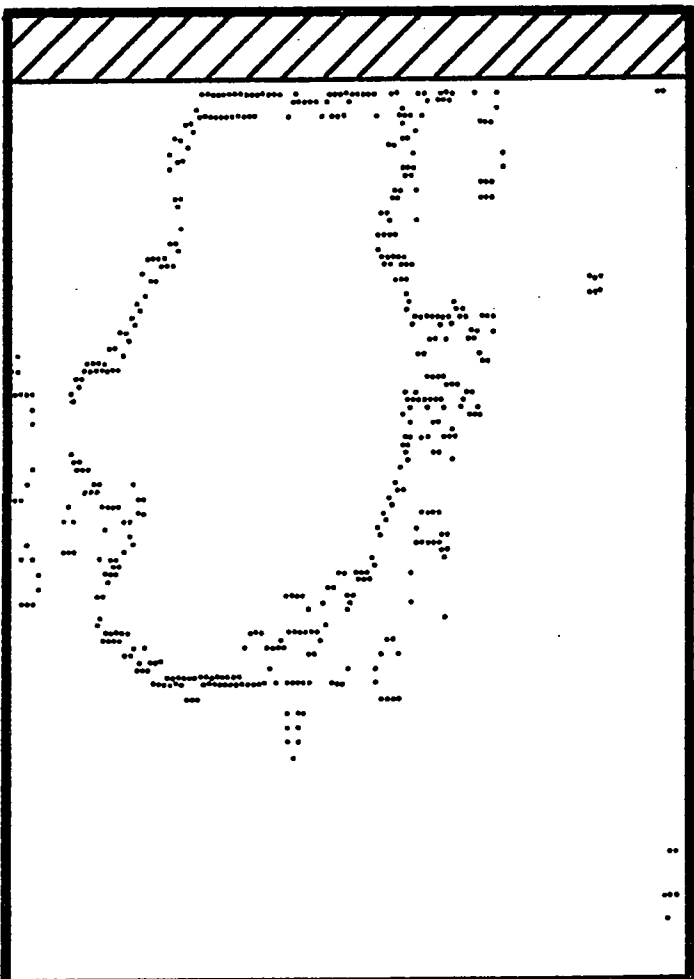
100 torr

500 torr

variation is a result of an irreproducible vaporization pulse. Although shot-to-shot power variations were on the order of only 5%, the multimode nature of the laser beam produces unpredictable effects on the focusing and hence vaporization properties of the laser pulse. For more reproducible plume formation, a TEM_{00} mode vaporization laser should probably be used. Although the scope of our plume mapping experiments was somewhat limited, we feel that we have shown that our diagnostic technique can provide a valuable means of studying these types of systems.

Throughout this chapter, we have commented on how slow a process source mapping by rastering techniques can be compared to our system. At this point it is useful to make a direct time comparison to see what kind of advantage we really hold. As a case in point, we will do the calculation on the time required to do a flame mapping experiment. Our digital image processor creates a 14,400 point image of the system. Since we are measuring absorbance I and I_0, measurements must be made for each point to be mapped resulting in a total of 28,800 points which must be measured. To achieve a total sampling time per point of 1 sec, our image processor must sum together 60 frames of data, this process requires a total data acquisition time of 30 seconds. To achieve the same total sampling time for each data point, the total data acquisition time by rastering techniques would be 8 hours.

Even though our diagnostic system performed quite well, there are a few changes which could be made to improve its performance and broaden its applicability. One of these improvements, the use of a TEM_{00} mode

vaporization laser, has already been mentioned. The use of a nitrogen or YAG pumped dye laser system as the probe would not only increase the time resolution attainable in transient system studies, but would also allow a much wider range of species to be studied because of their broader tuning range. Associated with a change to this type of probe laser, however, are possible problems with pulse-to-pulse variations which are minimal with the present cw or gated cw probe laser system.

There are several logical extensions to this work, the most obvious of which may perhaps be studies in turbulent combustion processes where the simultaneous nature of our detection would be useful. Other systems which come to mind include mapping of absorbing species in inductively coupled and DC plasma sources. All of the systems mentioned up to this point require absorption in the visible or ultraviolet regions of the spectra, but what about vibrational type measurements? Spectroscopic techniques such as inverse Raman and Raman-induced Kerr effect spectroscopy (RIKES) present the possibility at least of making spatially resolved Raman measurements in condensed phase systems, where application to vapor phase systems is questionable at this point.

Conclusion

In this chapter we have shown that the technique of simultaneous spatially resolved absorption spectroscopy, combining the use of a tunable dye laser as the primary light source and a vidicon camera as the two-dimensional detector, can be a powerful diagnostic tool for the study of a number of different physical systems. This technique is

faster than conventional and can reap more information from a single event than conventional rastering techniques. Examples of the power of this system displayed include studies on the distribution of atomic and molecular species in flames and atomic species in laser-generated vapor plumes. Suggestions for improvements on the system and further applications have been given.

CONCLUSIONS

In this dissertation, we have presented four examples of new laser-based spectroscopic techniques. In the first chapter, we demonstrated the possibility of obtaining Doppler free spectral of large organic molecules by an intracavity absorption technique. A new technique for determining absolute Raman cross-sections utilizing the inverse Raman effect was presented in the second chapter. This technique is free from many of the problems associated with conventional Raman cross-section measurements. In the third chapter, we demonstrated $D \leftarrow X$ resonance enhanced three-photon absorption of molecular iodine. This study allowed us to refine some of the spectral constants for the D state of this molecule. In the final chapter, we demonstrated the possibility of using simultaneous spatially resolved absorption spectroscopy as a diagnostic tool for the mapping of atomic and molecular species in physical systems.

Although laser-based spectroscopic techniques should not be viewed as a panacea, their application has provided valuable answers to previously unanswered questions.

REFERENCES

1. Shen, Y. R. <u>Rev. Mod. Phys.</u>, 1976, 48(1), 1.

2. Swofford, R. L.; Albrecht, A. C. <u>Ann. Rev. Phys. Chem.</u>, 1978, 29, 421.

3. Letokhov, V. S.; Chebotayev, V. P. "Nonlinear Laser Spectroscopy", Springer-Verlag: Berlin, 1976.

4. Shimoda, K. "High Resolution Laser Spectroscopy", Springer-Verlag: Berlin, 1976.

5. Goeppert-Mayer, M. <u>Ann. Phys.</u>, 1931, 9, 273.

6. Kaiser, W.; Garrett, C. <u>Phys. Rev. Lett.</u>, 1961, 7, 229.

7. Peticolas, W. L. <u>Ann. Rev. Phys. Chem.</u>, 1967, 18, 233.

8. McClain, W. M. <u>Acc. Chem. Res.</u>, 1974, 7(5), 129.

9. Hochstrasser, R. M.; Wessel, J. E.; Sung. H. N. <u>J. Chem. Phys.</u>, 1974, 60, 317.

10. Twarowski, A. J.; Kliger, D. S. <u>Chem. Phys.</u>, 1977, 20, 253.

11. Rentzepis, P. M.; Pao, Y. H. <u>J. Chem. Phys.</u>, 1966, 44, 2931.

12. Johnson, P. M. <u>J. Chem. Phys.</u>, 1975, 62, 45.

13. Johnson, P. M. <u>J. Chem. Phys.</u>, 1976, 64, 4143.

14. Goldsmith, J. E. M.; Ferguson, A. I.; Lawler, J. E.; Schawlow, A. L. <u>Opt. Lett.</u>, 1979, 4, 230.

15. Mahr, H. In "Quantum Electronics", Robin, H.; Tang, C. L., Eds.; Academic Press: New York, 1969, Chapter 4.

16. Gold, A. In "Quantum Optics", Glauber, R. J., Ed.; Academic Press: New York, 1969.

17. Lamb, W. E. <u>Phys. Rev.</u>, 1964, 134, A1429.

18. Szoke, A.; Javan, A. <u>Phys. Rev. Lett.</u>, 1963, 10, 521.

19. Eckstein, J. N.; Ferguson, A. I.; Hansch, T. W. <u>Phys. Rev. Lett.</u>, 1978, 40, 847.

20. Shimoda, K. <u>Appl. Phys.</u>, 1976, 9, 239.

21. Hänsch, T. W.; Harvey, K. C.; Meisel, G.; Schawlow, A. L. Optics Comm., 1974, 11, 50.

22. Oka, T. In "Laser Spectroscopy", Brewer, R. G.; Mooradian. A., Eds.; Plenum: New York, 1974.

23. Salour, M. M.; Cohen-Tannoudji, C. Phys. Rev. Lett., 1977, 38, 757.

24. Teets, R.; Eckstein, J.; Hänsch, T. W. Phys. Rev. Lett., 1977, 38, 760.

25. Wieman, C.; Hänsch, T. W. Phys. Rev. Lett., 1976, 36, 1170.

26. Teets, R.; Feinberg, R.; Hänsch, T. W.; Schawlow, A. L. Phys. Rev. Lett., 1976, 37, 683.

27. Khoo, I. C.; Yeung, E. S. Optics Comm., 1977, 22, 83.

28. Vasilenko, L. S.; Chebotaev, V. P.; Shishaev A. V. JETP Lett., 1970, 12, 113.

29. Roberts, D. E.; Fortson, E. N. Phys. Rev. Lett., 1973, 31, 1539.

30. Kelley, P. L.; Kildal, H.; Schlossberg, H. R. Chem. Phys. Lett., 1974, 27, 62.

31. Baraben, F.; Cognac, B.; Crynberg, G. Phys. Rev. Lett., 1974, 32, 643.

32. Levenson, M. D.; Bloembergen, N. Phys. Rev. Lett., 1974, 32, 645.

33. Hänsch, T. W.; Hervey, K. C.; Meisel, G.; Schawlow, A. L. Opt. Comm., 1974, 11, 50.

34. Bjorkholm, J. E.; Liao, P. F. Phys. Rev., 1976, A14, 751.

35. Flusberg, A.; Mossberg, T.; Hartman, S. R. Phys. Rev., 1976, A14, 2146.

36. Hänsch, T. W.; Lee, S. A.; Wallenstein, R.; Wienman, C. Phys. Rev. Lett., 1975, 34, 307.

37. Kowalski, J.; Neuman, R.; Suhr, H.; Winkler, K.; zu Putliz, G. Z. Physik, 1978, A287, 247.

38. Bloembergen, N.; Levenson, M. D. In "High Resolution Laser Spectroscopy", Shimoda, K., Ed.; Springer-Verlag: Berlin, 1976, Chapter 8.

39. Bischel, W. K.; Kelley, P. J.; Rhodes, C. K. Phys. Rev. Lett., 1975, 34, 300.

40. Bischel, W. K.; Kelley, P. J.; Rhodes, C. K. Phys. Rev., 1976, A13, 1817.

41. Woerdman, J. P. Chem. Phys. Lett., 1976, 43, 279.

42. Gelbwachs, J. A.; Jones, P. F.; Wessel, J. E. Appl. Phys. Lett., 1975, 27, 551.

43. Bernheim, R. A.; Kittrell, C.; Veirs, D. K. J. Chem. Phys., 1978, 69(3), 1308.

44. Chen, K.; Khoo, I. C.; Steenhoek, L. E.; Yeung, E. S. Optics Comm., 1977, 23, 90.

45. Gelbwachs, J. A.; Wessel, J. E. Opt. Eng., 1977, 16, 197.

46. Bosel, U.; Neusser, H. J.; Schlag, E W. Chem. Phys., 1976, 15, 167.

47. Nsieh, J. C.; Laor, U.; Ludwig, P. K. Chem. Phys. Lett., 1971, 10, 412.

48. Yeung, E. S. J. Molec. Spectrosc., 1974, 53, 379.

49. Hughes, L. J. Ph.D. Dissertation, Iowa State University, Ames, IA, 1979.

50. Tang, C. L.; Levin, K. Tenth International Quantum Electronics Conference, Atlanta, GA, 1978.

51. Van Duyne, R. P.; Jeanmaire, D. L.; Shriver, D. F. Anal. Chem., 1974, 46, 213.

52. Jones, W. J.; Stoicheff, B. P. Phys. Rev. Lett., 1964, 13(22), 657.

53. Duardo, J. A.; Johnson, F. M.; El-Sayed, M. A. Phys. Lett., 1966, 21(2), 168.

54. Gadow, P.; Lau, L.; Thuy, Ch. T.; Weigmann, H. S.; Werncke, W.; Lenz, K.; Peiffer, M. Optics Comm., 1971, 4, 226.

55. Mc Laren, R. A.; Stoicheff, B. P. Appl. Phys. Lett., 1970, 8, 168.

56. Tsunoda, Y. Jap. J. Appl. Phys., 1972, 11, 1293.

57. Alfano, R. R.; Shapiro, S. L. Chem. Phys. Lett., 1971, 8, 631.

58. Werncke, W.; Lau, A.; Pfeiffer, M.; Weigmann, H. J.; Hunsalz, G.; Lenz, K. Optics Comm., 1976, 16, 128.

59. Lin, S. H.; Reid, E. S.; Tredwell, C. J. Chem. Phys. Lett., 1974, 29, 389.

60. Strizhevskii, V. L.; Kondilenko, E. I. Optics and Spectry., 1970, 30, 127.

61. Von Holle, W. U.S. Ballistic Research Laboratories Memorandum Report, No. 2607, 1974.

62. Stone, J. J. Chem. Phys., 1978, 69, 4349.

63. Barrett, J. J.; Berry, M. J. Appl. Phys. Lett., 1979, 34, 144.

64. Heiman, D.; Hellwarth, R. W.; Levenson, M. D.; Martin, C. Phys. Rev. Lett., 1976, 36, 189.

65. Morris, M. D.; Wallan, D. J.; Ritz, G. P.; Haushalter, J. P. Anal. Chem., 1978, 58(13), 1796.

66. Hughes, L. J.; Steenhoek, L. E.; Yeung, E. S. Chem. Phys. Lett., 1978, 59(3), 413.

67. Mc Clung, F. G.; Weiner, D. J. Opt. Soc. Am., 1964, 54, 641.

68. Lotem, H.; Araujo, B. D. Phys. Rev., 1977, B16, 1711.

69. Regnier, R. P.; Taran, J. P. E. Appl. Phys. Lett., 1973, 23, 240.

70. Brandmuller, J.; Schrotter, H. W. Z. Phys., 1957, 149, 131.

71. Udagawa, Y.; Mikami, N.; Kaya, K.; Ito, M. J. Raman Spectrosc., 1973, 1, 341.

72. Skinner, J. G.; Nilsen, W. G. J. Opt. Soc. Am., 1968, 58, 113.

73. Fenner, W. R.; Hyatt, H. A.; Kellam, J. N.; Porto, S. P. S. J. Opt. Soc. Am., 1973, 63, 73.

74. Kato, Y.; Takuma, H. J. Opt. Soc. Am., 1971, 61, 347.

75. Swofford, R. L. Ph.D. Thesis, University of California, Berkeley, CA, 1973.

76. Owyoung, A.; Peercy, P. S. J. Appl. Phys., 1977, 48, 674.

77. Cowley, M. W.; Eisenthal, K. B.; Peticolas, W. L. Phys. Rev. Lett., 1967, 18, 531.

78. Yariv, A. "Quantum Electronics", 2nd ed.; Wiley: New York, 1975.

79. Zeigler, H. J.; Tannenwald, P. E.; Kern, S.; Herendeen R.
    Phys. Rev. Lett., 1973, 11, 419.

80. Bonch-Bruevich, A. M.; Khodovoi, V. A. Soviet Phys. Usp.,
    1965, 8, 1.

81. Mulliken, R. S. J. Chem. Phys., 1971, 55, 288.

82. Rousseau, D. L.; Williams, P. F. Phys. Rev. Lett., 1974, 33, 1368.

83. Danyluk, M. D.; King, G. W. Chem. Phys., 1977, 22, 59.

84. Williamson, A. D. Chem. Phys. Lett., 1979, 60, 451.

85. Sander, R. K.; Wilson, K. R. J. Chem. Phys., 1975, 63, 4242.

86. Petty, G.; Tai, C.; Dalby, F. W. Phys. Rev. Lett., 1975, 34, 1207.

87. Dalby, F. W.; Petty, G.; Pryce, M. K. L.; Tai, C. Can. J. Phys.,
    1977, 55, 1033.

88. Zandee, L.; Bernstein, R. B.; Lichtin, D. A. J. Chem. Phys., 1978,
    69, 3427.

89. Callear, A. B.; Metcalfe, M. P. Chem. Phys. Lett., 1976, 43, 197.

90. Tellinghuisen, J. Chem. Phys. Lett., 1974, 29, 359.

91. Herzberg, G. "Spectra of Diatomic Molecules", 2nd ed.;
    D. Van Nostrand: Princeton, NJ, 1950.

92. Faiasal, F. H. M.; Wallenstain, R.; Zacharias, H. Phys. Rev. Lett.,
    1977, 39, 1138.

93. Piepmeier, E. H.; Osten, D. E. Appl. Spectrosc., 1971, 25, 642.

94. Chromiak, J. Combust. Flame, 1972, 18, 429.

95. Manabe, R. M.; Piepmeier, E. H. Anal. Chem., 1979, 51, 2066.

96. Jones, D. G.; Mackie, J. C. Combust. Flame, 1976, 27, 143.

97. Pealat, M.; Bailly, R.; Taran, J. E. Optics Comm., 1977, 22, 91.

98. Castleman, K. R. "Digital Image Processing", Prentice-Hall:
    Englewood Cliffs, New Jersey, 1979.

99. Talmi, Y. Anal. Chem., 1975, 47, 697A.

100. Rosenfeld, A.; Kak, A. C. "Digital Picture Processing", Academic Press: New York, 1979.

101. Gonzalez, R. C.; Wintz, P. "Digital Image Processing", Addison-Wessley: Reading, Mass., 1977.

102. Rosenfeld, A. "Digital Picture Analysis", Springer-Verlag: Berlin, 1976.

103. Ingram, M.; Preston, K. Sci. Amer., 1970, 223, 72.

104. Howry, D. H. In "Ultrasound in Biology and Medicine", Kelley, E., Ed.; Waverly Press: Baltimore, 1970.

105. Payne, J. T.; McCullough, E. C. Applied Radiology, 1976, 103, 53.

106. Bernstein, R. IBM J. Res. Develop., 1976, 20, 40.

107. Stucki, P. In "Advances in Digital Image Processing", Stucki, P., Ed.; Plenum: New York, 1979, p 177.

108. Kruger, R. P. "Imaging Applications for Automated Industrial Inspection and Assemgly", Society of Photo-optical Instrumentation Engineers: Bellingham, Washington, 1979.

109. McCord, T. B.; Westphall, J. A. Appl. Opt., 1972, 11, 552.

110. Busch, K. W.; Howell, N. G.; Morrison, G. H. Anal. Chem., 1974, 46, 575.

111. Milano, M. J.; Pardu, H. L.; Cook, T. E ; Santini, R. E.; Margerum, D. W.; Raycheba, J. M. T. Anal. Chem., 1974, 46, 374.

112. Knapp, D. O.; Omenetto, L. P.; Plankey, F. W.; Wienfordner, J. O. Anal. Chem., 1974, 69, 455.

113. Jackson, K. W.; Aldous, K. M.; Mitchell, D. C. Spectrosc. Lett., 1973, 6, 1315.

114. Milano, M. J.; Pardu, H. L. Anal. Chem., 1975, 47, 25.

115. Magde, D.; Windsor, M. W. Chem. Phys. Lett., 1974, 27, 31.

116. Felkel, H. L.; Pardue, H. L. Anal. Chem., 1977, 8, 1112.

117. Felkel, H. L.; Pardue, H. L. Anal. Chem., 1978, 50, 602.

118. Johnson, D. W.; Callis, J. B.; Christian, G. D. Anal. Chem., 1977, 8, 747A.

119. Rann, C. S.; Hambly, A. N. Anal. Chem., 1965, 37, 879.

120. Chakrabarti, C. L.; Katyal, M.; Willis, D. E. Spectrochim. Acta, 1970, 25B, 629.

121. Fassel, V. A.; Cowley, T. G.; Kniseley, R. N. Spectrochim. Acta, 1968, 23B, 771.

122. Fassel, V. A.; Willis, J. B.; Fiorino, J. A. Spectrochim Acta, 1969, 24B, 157.

123. Scott, R. H.; Strasheim, A. Spectrochim. Acta, 1971, 26B, 707.

124. Giovannini, E.; Principato, G. B.; Rondelli, F. Anal. Chem., 1976, 48, 1517.

125. Kirchheim, R.; Nagorny, R.; Maier, K.; Töly, G. Anal. Chem., 1976, 48, 1505.

126. Sumino, K.; Yamamoto, R.; Fumikazu, H.; Kitamura, S.; Itoh, H. Anal. Chem., 1980, 52, 1064.

127. Ishizuka, T.; Uwanino, Y.; Sunahara, H. Anal. Chem., 1977, 49, 1339.

128. Vul'fson, E. K.; Karyakin, A. V.; Shidovski, A. I. Zh. Anal. Khim., 1973, 28, 1253.

129. Kantor, T.; Polos, L.; Fodor, P.; Pungor, E. Talanta, 1976, 23, 585.

130. Kwong, H. S.; Measures, R. M. Anal. Chem., 1979, 51, 428.

131. Conzemius, R. J.; Svec, H. J. Anal. Chem., 1978, 50, 1854.

132. Fiorino, J. A.; Kniseley, R. N.; Fassel, V. A. Spectrochim. Acta, 1968, 23B, 413.

133. Billings, G. K. Ph.D. Dissertation, Rice University, Houston, Texas, 1963.

134. Koirtyohann, S. R.; Pickett, E. E. Anal. Chem., 1966, 38, 585.

135. Krivchikova, E. P.; Taganov, K. I. Zh. Prikl. Spektrosk., 1973, 19, 601.

136. Treytl, W. J.; Marich, K. W.; Glick, D. Anal. Chem., 1975, 47, 1275.

137. Stupp, H. J.; Overhoff, Th. _Spectrochim. Acta_, 1975, 30B, 77.

138. Mikhnov, S. A.; Panteleev, V. V.; Strizhnev, V. S.; Yankovskii, A. A. _Zh. Prikl. Spektrosk._, 1971, 17, 394.

139. Milne, W. E. "Numerical Calculus", Princeton University Press: Princeton, New Jersey, 1949.

ACKNOWLEDGEMENTS

123

APPENDIX A: CIRCUIT DIAGRAMS AND DESCRIPTIONS

This Appendix contains circuit descriptions and diagrams for the image conversion interface (ICI), and associated pulse and delay generation circuits. The circuit diagrams will be shown and discussed in detail in order to facilitate modification or repair of the ICI.

Image Conversion Interface

Digitization format

The vidicon camera has a 525 line/frame, 30 frame/sec, 2:1 interlaced scanning format. The ICI digitizes only the odd-numbered lines of the frame. This gives vertical resolution of 240 picture elements. The ICI is capable of digitizing 60 points per line. In order to increase the effective horizontal resolution, every other line of data is staggered by one-half of a digitization cycle. The data acquisition format is shown in Figure Al where dashed lines represent nondigitized lines of data, solid lines represent digitized lines, and X's represent points of digitization. With the staggered data format, the ICI is capable of effective 120x120 pixel resolution.

Timing and control circuits

Since the vidicon camera is free running at the standard television raster rate of thirty frames per second, it is necessary for the ICI to recognize the start of a new frame of data. This is the first function of the timing and control circuit that will be discussed. The vidicon camera provides a horizontal blanking output signal which contains
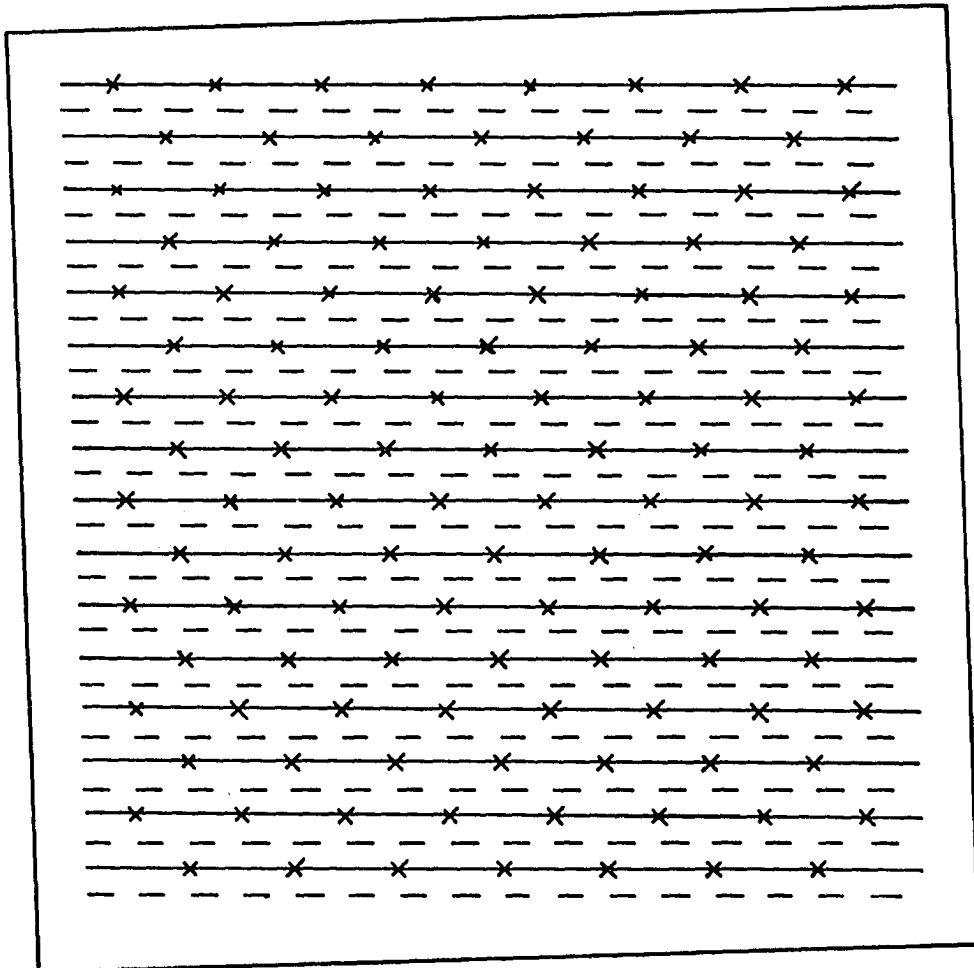
124

Figure A1. ICI digitization format

information defining the start of a new frame, and those segments of the video signal that contain valid information. The start of frame recognition circuit consists of three integrated circuits shown in Figure A2 as 28HZ, 28HY, and 28HX. To enable the ICI, a zero-going TTL pulse must be applied to ICI bus M. This enables 28HZ and clears 28HX.

The start of a new frame is characterized by a single 3 μsec zero-going pulse in the horizontal blanketing signal (line A Figure A3). The horizontal blanking signal triggers 28HZ on the falling edge of all zero-going pulses, producing a 10 μsec pulse which enables 28HY for this 10 μsec period. The output of 28HZ is shown in line B of Figure A3. The rising edge of pulses in the horizontal blanking signal triggers 28HY when enabled. Since 28HY is only enabled for 10 μsec periods, only zero-going pulses of less than 10 μsec in duration will trigger 28HY. The 3 μsec start of frame pulse is the only pulse which fits this criterion and is, therefore, the only pulse that will trigger 28HY (line C of Figure A3). Once triggered, 28HY produces a 35 nsec zero-going pulse which sets 28HZ enabling the rest of the ICI circuitry.

The second function of the timing and control circuitry is to control which portions of the frame of video information are to be digitized. This function is performed by the integrated circuits shown in Figure A2 as 28GV, 28GW, 28GX, 28GY, and 28GZ. Once the ICI has been enabled by the start of frame recognition circuit, output $\overline{Q1}$ of 28HY is held LOW (line C, Figure A3) and ORed with the horizontal blanking signal (line A, Figure A3) at 28HY. When both inputs of 28HY are held LOW, output Y1 will be HIGH indicating that valid video information is being

Figure A2. ICI timing and control circuit
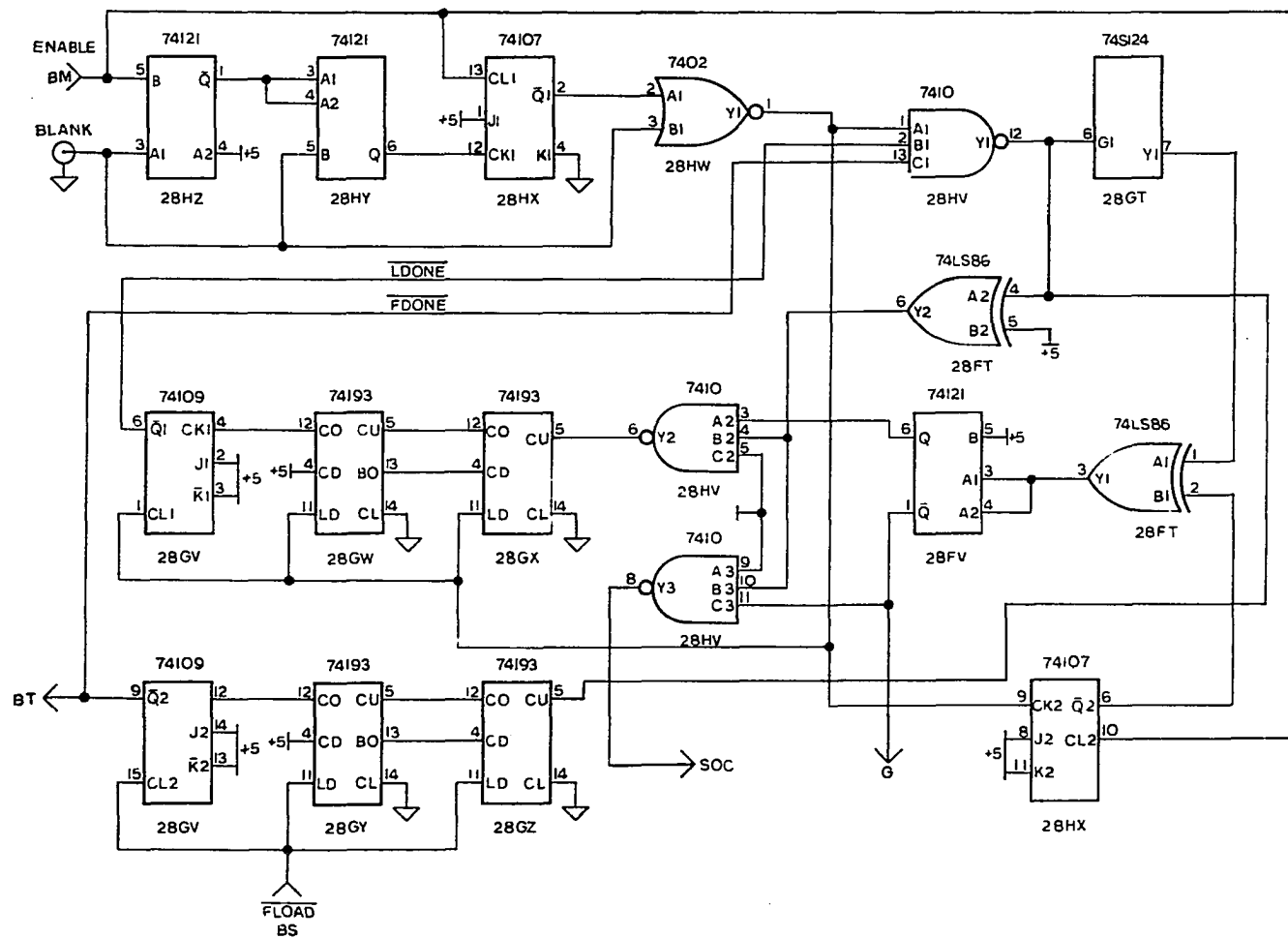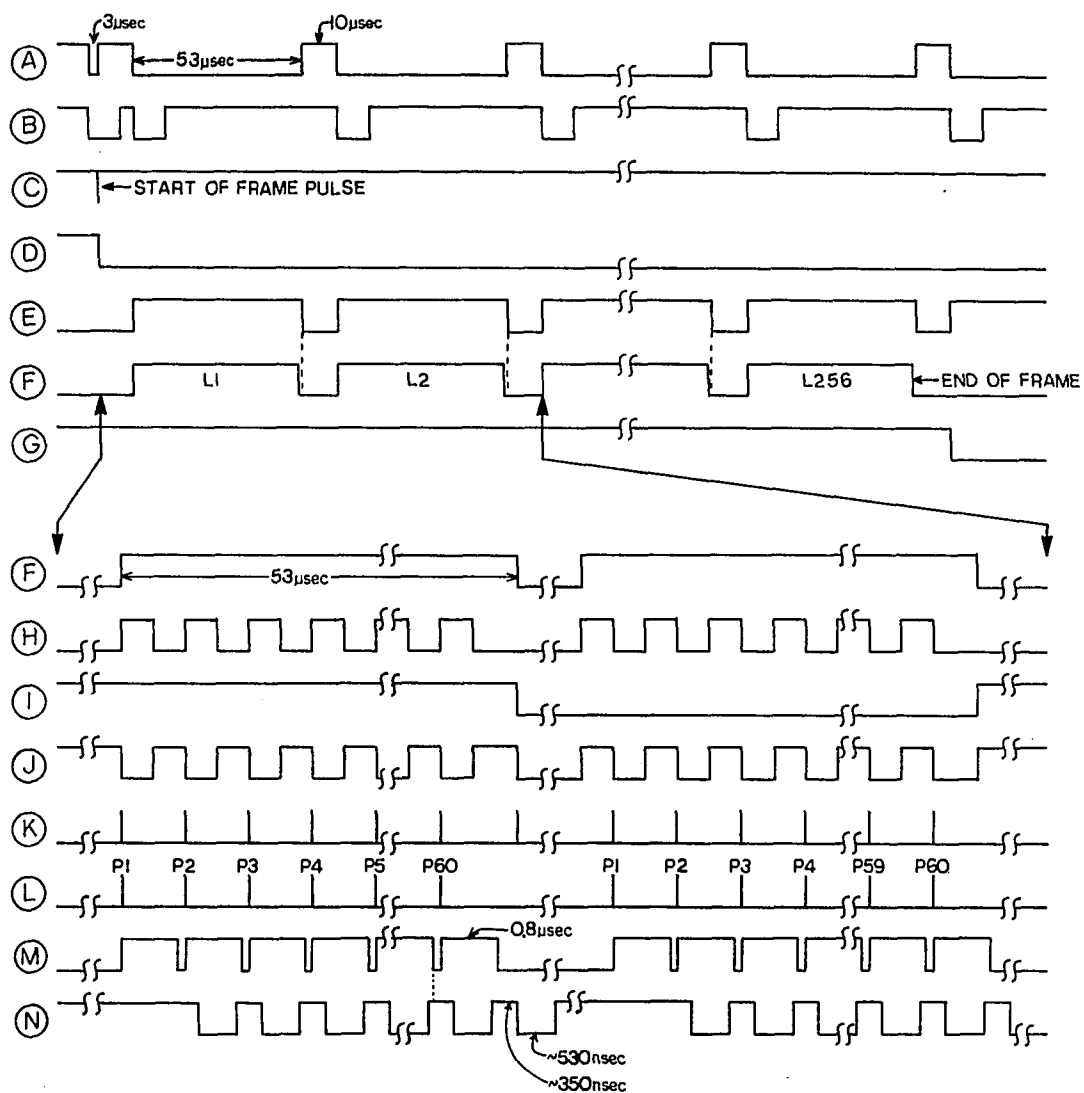
Figure A3.   ICI timing diagram

transmitted (line E, Figure A3). Yl of 28HW is ANDed with the outputs of the point and line counters, $\overline{LDONE}$ and $\overline{FDONE}$, respectively, at 28HV. When all three inputs of 28HV are HIGH, output Yl is held LOW and the clock circuit 28GT is enabled. The clock circuit will be disabled for any of the following reasons: invalid video present (Al LOW), point count finished (Bl LOW), or line count finished (Cl LOW).

The point and line count circuits are identical, each containing two four-bit binary counters and a $\overline{J}$-K flip-flop. Each of the circuits may be preset to a desired count state. The point count circuit (Figure A2, circuits 28GV, 28GW, 28GX) is preset at the beginning of each line of video information, and the line count circuit (Figure A2, circuits 28GV, 28GY, 28GZ) is preset at the beginning of each new frame of data. The point count circuit is advanced by Y2 of 28HV at the start of each analog to digital conversion until the desired number of points have been taken and the point count flip-flop disables the clock circuit by holding Bl of 28HV LOW. The clock is normally disabled just prior to the end of the line of video data as seen in lines E and F of Figure A3. The line count circuit is advanced at the end of each line of data by Yl of 28HV. When the appropriate number of lines have been digitized, the line count flip-flop disables 28HV by holding Cl of 28HV LOW (line G, Figure A3).

The final function of the timing and control circuitry is to determine when data conversion for each point should begin. In order to gain more horizontal resolution, the ICI uses a staggered data acquisition format as discussed earlier. Figure A3, line F, shows the data valid for two successive lines of data. Line H shows the output of the

clock circuit 28GT. The output of 28HX toggles on each line of data as shown in line I. In order to affect the offset described above, $\bar{Q}$ of 28HX (line I, Figure A3) and Y1 of 28GT (line H, Figure A3) are exclusive-ORed together at 28FT, resulting an output at Y1 of 28FT shown in Figure A3, line J. This output is used to trigger one-shot 28FV on the falling edge of the waveform, resulting in an output at Q shown in Figure A3 as line K. The outputs of 28FV are ANDed with Y2 of 28FT to remove unwanted pulses generated when 28HX toggles. The output of this AND gate is shown in Figure A3, line L, and is used as a start conversion signal.

Signal conversion circuit

The purpose of the signal conversion circuitry of the ICI is to convert the analog video signal from the vidicon camera to digital form so that it can be stored in the ICI for eventual storage and processing in the computer. There are three primary devices in the signal conversion circuit, including a sample and hold, an amplifier, and an analog-to-digital converter. The wiring diagram for the signal conversion circuit is shown in Figure A4.

In order to perform an analog-to-digital conversion on a rapidly changing analog signal, one must provide some means of temporary storage of the analog signal at the point at which one wishes to perform the signal conversion. This is the function of a sample and hold device. The ICI utilizes a Datel Model SHM-UH sample and hold module capable of holding a 5 VFS analog signal. The 0.0 to 0.7 volt video signal from the vidicon is fed into the analog input of the sample and hold. The

Figure A4. ICI signal conversion circuit
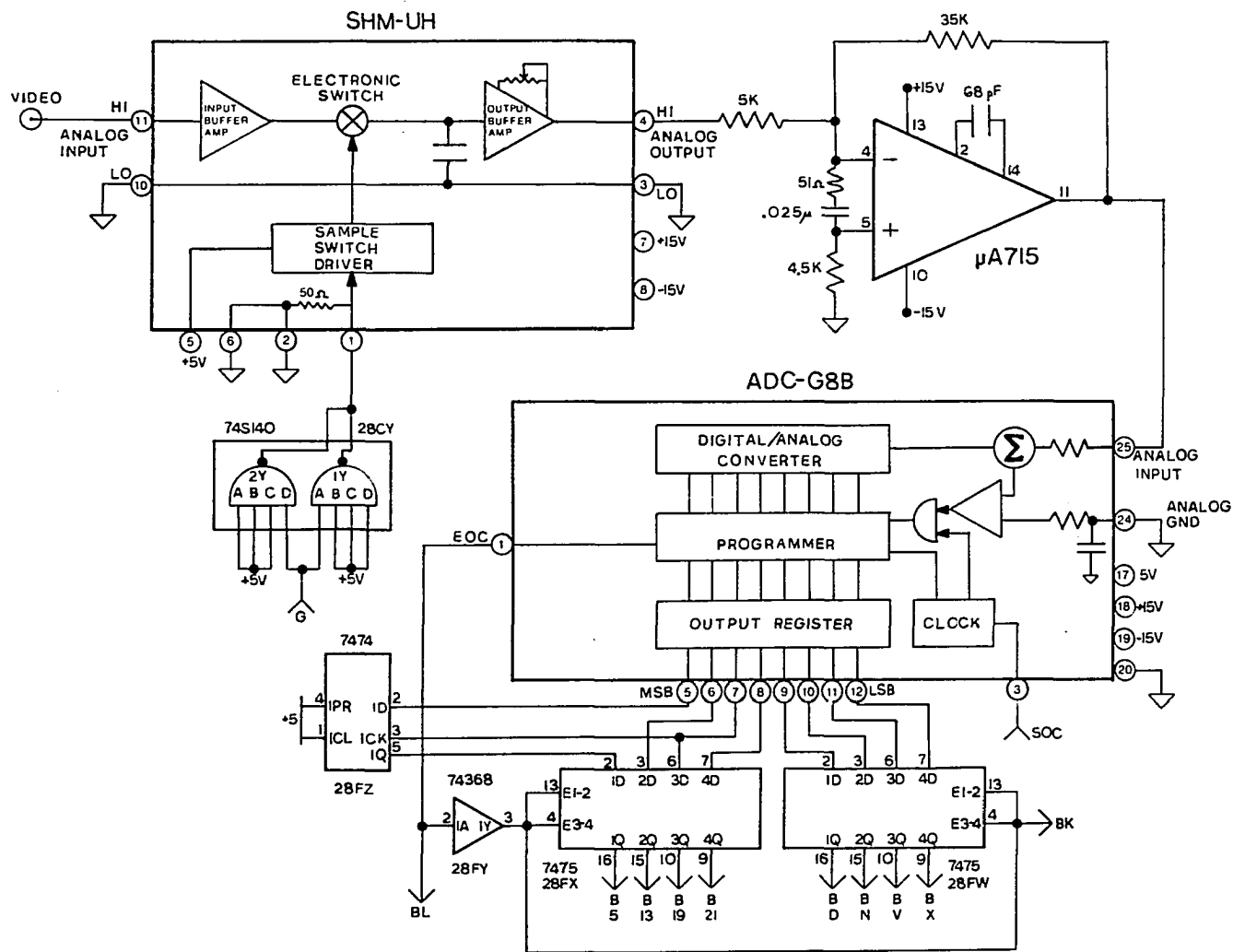
timing and control circuitry starts an analog-to-digital conversion by applying a 35 nsec zero going TTL pulse to buffer 28GY from $\bar{Q}$ of 28FV. This causes the sample and hold to track the video signal for the duration of the pulse and to hold the value of the input signal constant at the analog output upon completion of the pulse.

The analog amplifier is included in the signal conversion circuit to convert the 0.0 to 0.7 volt signal from the sample and hold to a 0.0 to -5.0 volt signal compatible with the analog to digital converter (ADC). The amplifier consists of a Fairchild uA715 high speed operational amplifier configured as an inverter with gain of seven. The output of the amplifier is connected to the analog input of the ADC.

Analog-to-digital conversion in the ICI is performed by a Datel Model ADC-G8B successive approximation type ADC. The converter has eight bits of resolution and a conversion time of 800 nsec. Conversion is initiated by the application of a 35 nsec positive going TTL pulse from Y3 of 28HV to pin 3 of the ADC (line L, Figure A3). The conversion is complete 800 nsec after the start of conversion as indicated by the end of conversion output of the ADC going LOW (line M, Figure A3). At this time, the data available at the output of the converter is a valid digital representation of the sampled analog signal. The end of conversion signal also serves to gate the latch circuits, 28FX and 28FW, which act as a one-word storage buffer for the data while it is being stored in the memory of the ICI.

Memory and address generation

The memory of the ICI contains 16K 8 bits of static random-access semiconductor memory (Texas Instruments TMS 4034 NL). This memory is configured as sixteen 1K 8 bit memory boards with only one board being enabled at a time. The wiring diagrams for the memory and address generating circuits are shown in Figures A5 and A6.

Address generation will be the first function of the memory and address generation circuits to be discussed. Since 1024 bits of information are stored in each of the individual memory chips, ten bits of address information are required to describe all of the memory locations. An additional four fits of address information are required to address the proper memory board. This address information is generated by a series of four four-bit binary counters: 20BW, 20BX, 20BY, 20BZ. These counters are cleared before the start of a new frame of data and before unloading the data buffer into the computer. The address is incremented after each analog of digital conversion by the end of conversion signal, or by the computer after transfer of a data point to the computer. The ten least significant bits of the counter output are used to address the memory chips via buffers 20AY and 20AZ. The four most significant bits of counter output are used to address 20DY, a 4-line to 16-line decoder/demultiplexer which serves to enable one memory board at a time.

The second function of the memory and address generating circuitry to be discussed is memory timing. The timing diagram for the memory write cycle is shown in line K of Figure A3. Prior to an address change

Figure A5.   ICI memory and data output buffer circuits

Figure A6. ICI address generation circuit
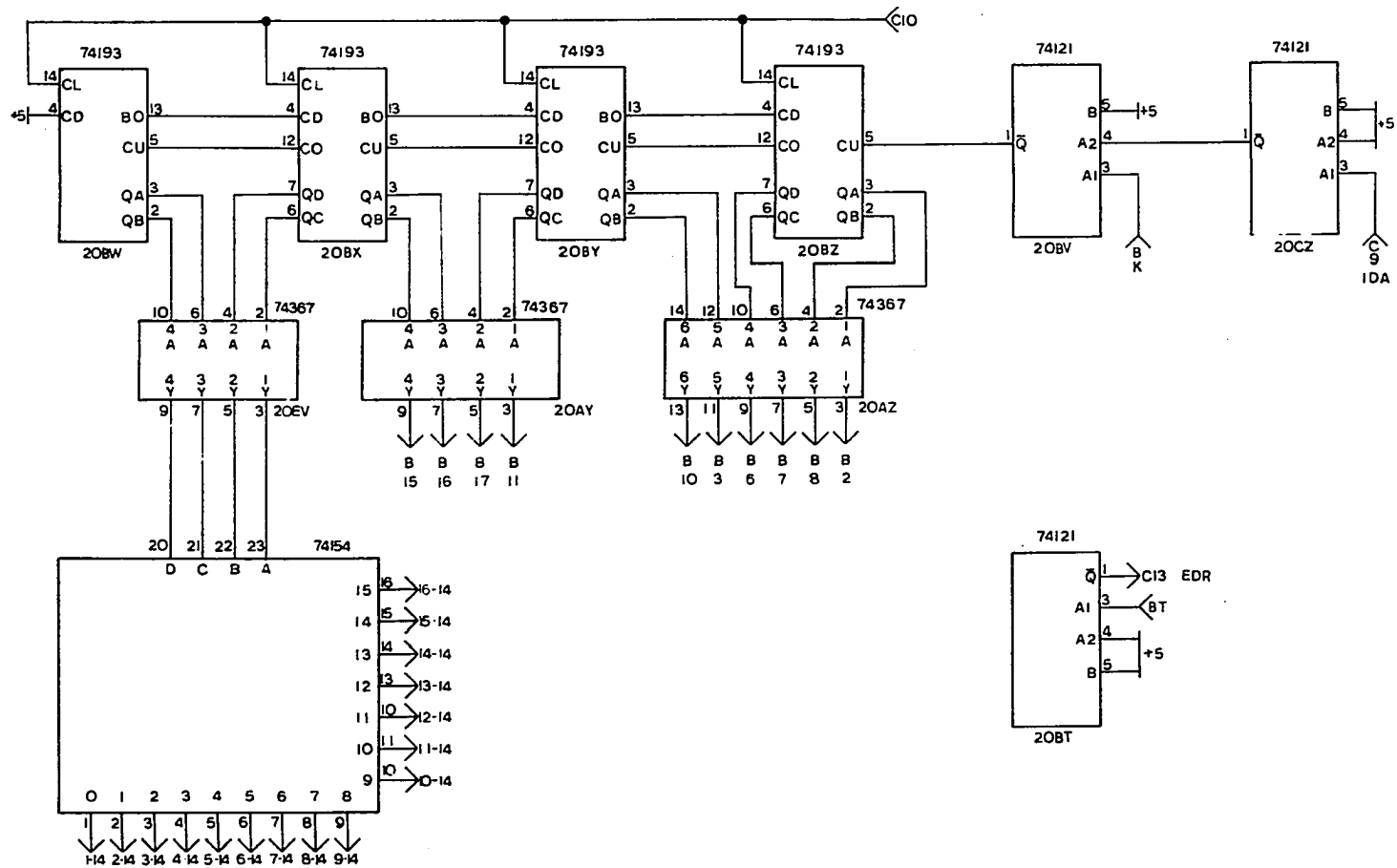
in the write mode the R/$\overline{W}$ input must be in the read state (HIGH). This eliminates the possibility of writing data into an unwanted location. After the change of address, the R/$\overline{W}$ input remains HIGH for a period of 300 nsec as governed by one-shot 20DW. After this address set up time, the R/$\overline{W}$ input is held LOW for a write period of 530 nsec, as governed by one-shot 20CV, after which it returns to the HIGH state for a minimum address hold time of 50 nsec before the address is incremented. During the read cycle, the R/$\overline{W}$ input is held in the HIGH state at all times. The output of the memory is buffered by 20AV, 20AW, 20EX, and 20EY to invert the signal and make it compatible with the computer logic, negative TTL.

ICI bus system

The ICI contains a 44-line internal data bus and a 16-line transfer bus for communication with the PDP-11 computer. Internal bus lines are denoted by a 'B' prefix and the computer-ICI bus lines are denoted by a 'C' prefix (e.g., BM or C11). Table A1 lists the configuration of the internal bus and Table A2 lists the configuration of the computer-ICI bus.

Table A1. ICI internal bus assignments

Bus	Function	Bus	Function
BX	D1 in	B10	A5
BV	D2 in	B11	A6
BN	D3 in	B17	A7
BD	D4 in	B16	A8
B21	D5 in	B15	A9
B19	D6 in	B9	R/$\overline{W}$
B13	D7 in	B14	CE
B5	D8 in	BF	Video In
BY	D1 out	BH	Analog GRD
BW	D2 out	BJ	HORZ. Blank
BP	D3 out	B1	+5 V supply
BE	D4 out	BA	+5 V supply
B20	D5 out	B22	GRD
B18	D6 out	BZ	GRD
B12	D7 out	BB	+15 V supply
B4	D8 out	BC	-15 V supply
B2	A0	BK	End of conversion
B8	A1	BL	End of conversion
B7	A2	BM	Interface enable
B6	A3	BS	Line count load
B3	A4	BT	Ext. data ready

Table A2. Computer-ICI bus assignments

Bus	Function[a]
C1	0 in (data in LSB)
C2	1 in (data in)
C3	2 in (data in)
C4	3 in (data in)
C5	4 in (data in)
C6	5 in (data in)
C7	6 in (data in)
C8	7 in (data in MSB)
C9	Internal data accept (IDA)
C10	0 out (Address clear)
C11	1 out (Data buffer inhibit)
C13	External data ready (EDR)
C17	3 out (Interface enable)
C18	4 out (Line count load)
C23	Ground
C24	Ground

[a]In and out relative to the computer.

Pulse and Delay Generator

The function of the pulse and delay generator when used in conjunction with the ICI is to trigger the vaporization laser and the Bragg cell. The pulse and delay generator shown in Figure A7 is enabled by a pulse from the computer which sets the 74107 flip-flop. The next frame to be digitized is preceded 16 msec by a pulse in the vertical blanking signal from the vidicon camera. This pulse triggers two 74121 one-shots. The output pulse from one of the one-shots defines the time delay between the vaporization pulse and the probe pulse. The other defines the position in time of the probe pulse. These two one-shots in turn trigger two additional one-shots which fire the vaporization laser, enable the ICI, and gate the Bragg cell. Figure A8 is a calibration curve for the delay circuit, and Figure 9 is a calibration curve for the width of the Bragg cell gate.

Figure A7. Pulse and delay generator circuit
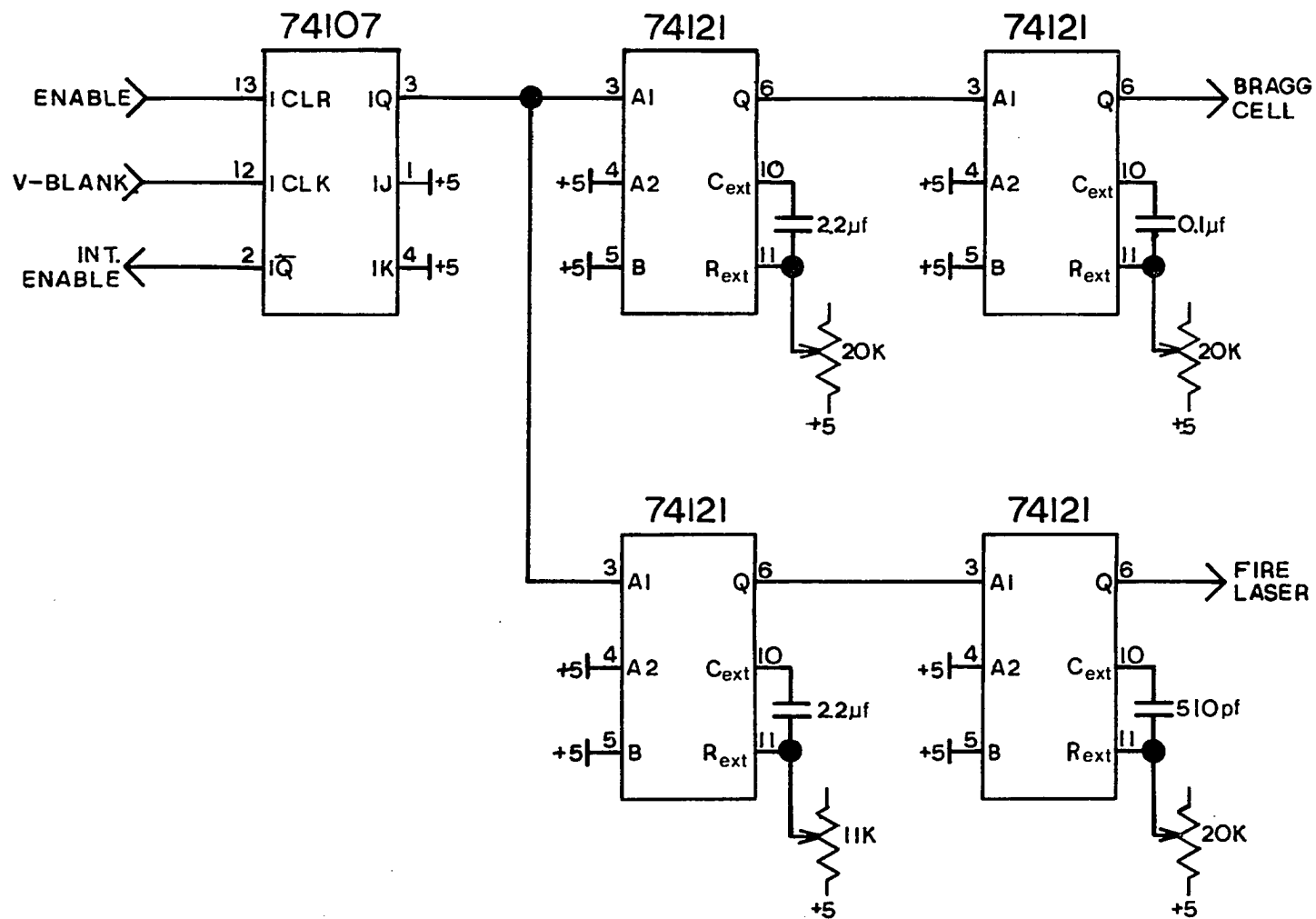
Figure A8. Delay calibration curve for pulse and delay circuit
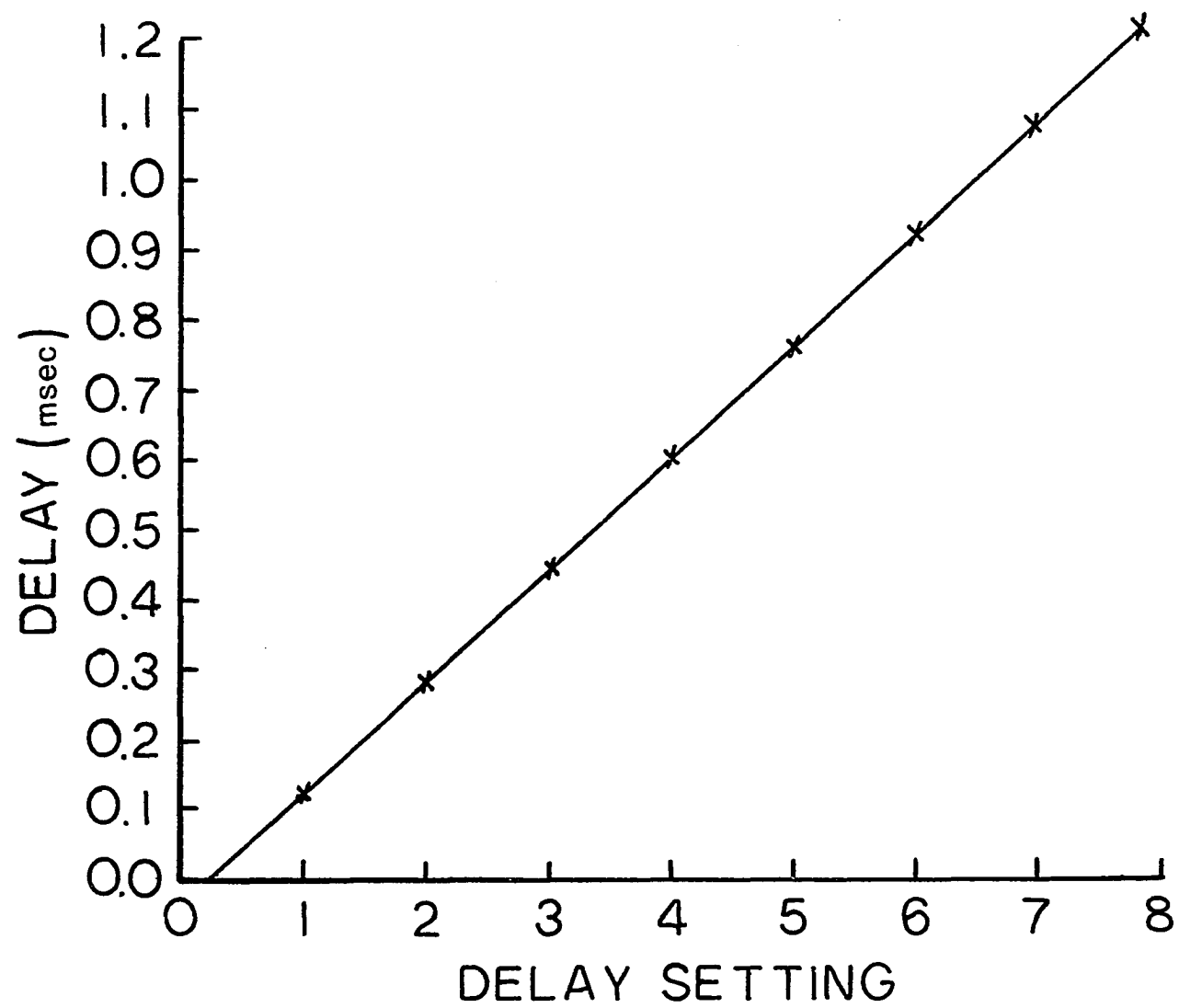
Figure A9. Probe pulse width calibration plot for the pulse and delay circuit
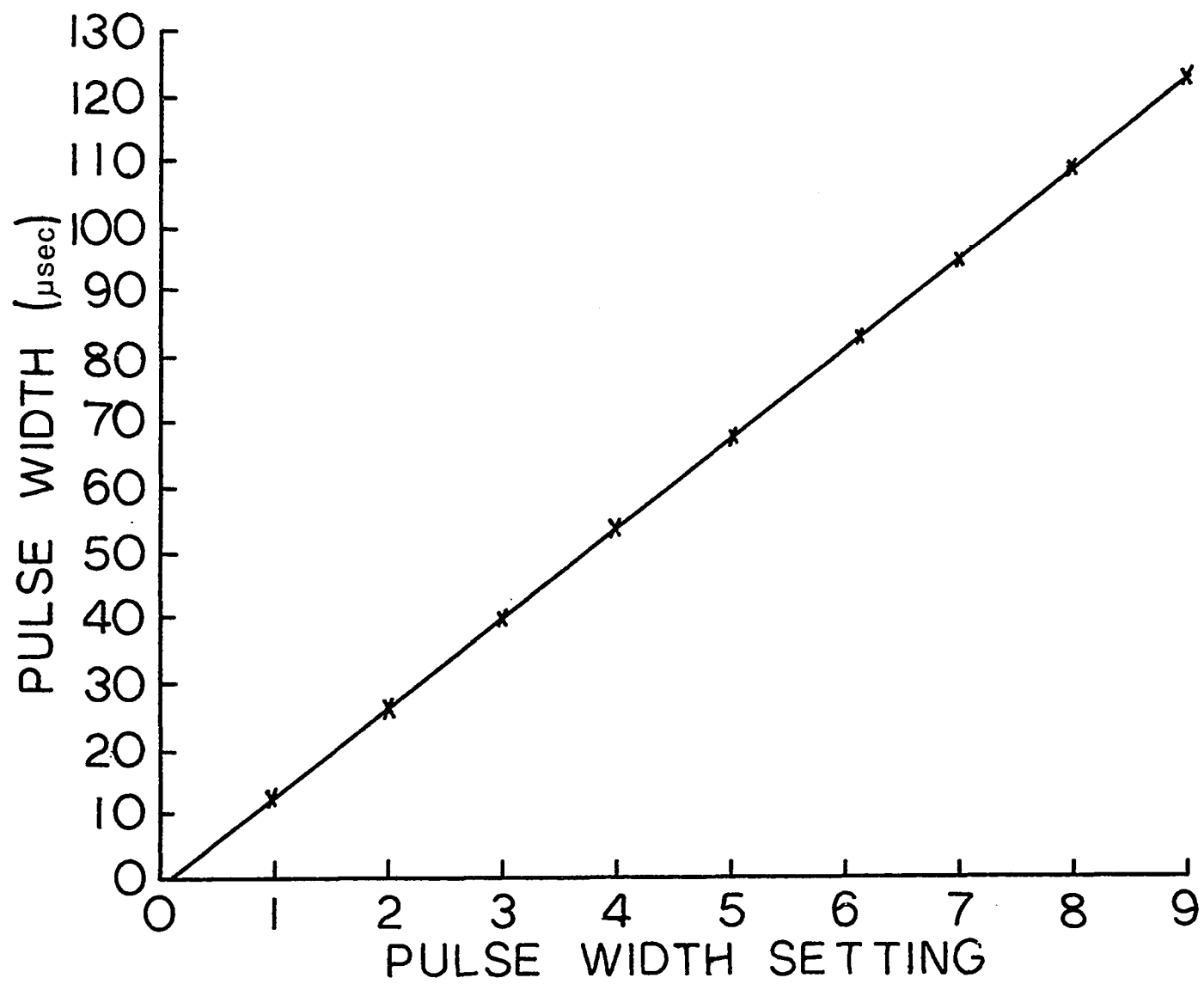
APPENDIX B: COMPUTER PROGRAMS

This Appendix contains descriptions and source file listings of computer programs used in the experiments discussed in Part II of this dissertation. Operating instructions for these programs are included with all user responses being underlined.

Program PTAKE

PTAKE is a FORTRAN language program which is used to control the operation of the ICI. PTAKE determines the number of frames to be digitized and then calls subroutine VIDMAC, a MACRO program which digitizes the video data and transfers it to the computer for storage. A source file listing of PTAKE and VIDMAC are given on the following pages.

To operate:

```
.RUN PTAKE <CR>
ENTER # OF FRAMES TO BE TAKEN 1<=N<=128
*50 <CR>
*DEV:FILE.EXT=<CR>
STOP --
```

```
C         ********** PROGRAM PTAKE **********
C
C
C
C         THIS PROGRAM ALLOWS THE OPERATOR TO CHOOSE
C         THE NUMBER OF FRAMES WHICH ARE TO BE TAKEN
C
C
C
          WRITE (5,10)
10        FORMAT(' ENTER # OF FRAMES TO BE TAKEN 1<=N<=128',/)
          READ (5,20) N
20        FORMAT(I3)
          CALL VIDMAC(N)
30        CONTINUE
          STOP
          END
          .GLOBL VIDMAC
          .MCALL ..V2..,.REGDEF
          ..V2..
          .REGDEF
          .MCALL .EXIT,.CSIGEN,.CLOSE,.WRITW
          STATUS=170410
          IBUFF=170412
          OBUFF=170414
;
;
VIDMAC:        TST      (R5)+
        MOV      @(R5)+,R2
        .CSIGEN #DSPACE,#DEXT
VID:    MOV      #15360.,R0
        MOV      #ARRAY,R1               ;LOAD LOC OF ARRAY
LOOP1:MOV        #000001,(R1)+           ;CLR ARRAY
        DEC      R0                      ;DEC COUNTER
        BNE      LOOP1
;
;
LOOP2:MOV        #15360.,R0              ;SET POINT COUNTER
        MOV      #ARRAY,R1               ;LOAD LOC OF ARRAY
        CLR      STATUS                  ;CLR STATUS REG
        MOV      #177774,OBUFF           ;CLR & RESET
        CLR      STATUS                  ;CLR STATUS REG
        MOV      #177745,OBUFF           ;ENABLE INTERFACE
;
;
LOOP:   TSTB     STATUS                  ;TEST FOR DATA READY
        BPL      LOOP
        CLR      STATUS
        BIC      #000001,OBUFF
```

```
        BIS       #000001,OBUFF
        BIS       #000002,OBUFF
;
;
LOOP3:CLR         STATUS                    ;CLR STATUS REG
        BIS       #000002,STATUS            ;READ INPUT BUFFER
        ADD       IBUFF,(R1)+               ;SUM TO MEMORY
        DEC       R0                        ;DEC POINT COUNTER
        BNE       LOOP3
        DEC       R2                        ;DEC FRAME COUNTER
        BNE       LOOP2
        MOV       #ARRAY,R2
        MOV       #-64.,R3
;
;
LOOP4:MOV         R3,R4
        ADD       #64.,R4
;
;
        .WRITW    #AREA,#0,R2,#240.,R4
        ADD       #480.,R2
        INC       R3
        BNE       LOOP4
        .CLOSE    #0
        .EXIT
AREA:   .WORD     0,0,0,0,0
DEXT:   .RAD50/              DAT/
;
;
        ARRAY:    .BLKW 15360.
        DSPACE=.
        RTS       PC
        .END
```

Programs PCON and FCON

PCON and FCON are FORTRAN language programs used to convert the I and I_0 intensity files generated with PTAKE into an absorbance file. The file created contains absorbance times 10^3. Although PCON and FCON serve the same purpose, PCON may be used only for single exposure files while FCON may be used for single as well as multiple exposure files. It is advantageous to use PCON whenever possible since its execution time is much less than that of FCON. Source file listings of PCON and FCON are given on the following pages.

To operate:

.RUN PCON <CR>

OUTPUT FILE = IFILE, IZFILE

*DEV:ABSFILE.EXT=DEV:IFILE.EXT,DEV:IZFILE.EXT <CR>

STOP --

.RUN FCON <CR>

OUTPUT FILE = IFILE, IZFILE

*DEV:ABSFILE.EXT=DEV:IFILE.EXT,DEV:IZFILE.EXT <CR>

STOP --

```
C          ********* PROGRAM PCON *********
C
C
C          THIS PROGRAM READS IN TWO DATA FILES CORRESPONDING TO
C          I AND IZERO, IT THEN CONVERTS THEM TO AN OUTPUT FILE
C          IN ABSORBANCE UNITS
C
C
C
           REAL*4 LOGT(256)
           INTEGER*2 IBUFF(240),IZBUFF(240), SPEC(39),OBUFF(240)
           REAL*4 EXT(2)
           DATA EXT/6RDATDAT,6RDATDAT/
C
C          CREATE LOG TABLE
C
           DO 10 N=1,256
10         LOGT(N)=ALOG10(FLOAT(N))
15         WRITE(5,20)
20         FORMAT(' OUTPUT FILE=IFILE,IZFILE',//)
30         IF(ICSI(SPEC,EXT,,,0).NE.0)GO TO 30
C
C          ALLOCATE CHANNELS
C
           ICHAN=IGETC()
           IZCHAN=IGETC()
           JCHAN=IGETC()
C
C          FETCH DEVICE HANDLERS
C
           IF(IFETCH(SPEC(16)).NE.0) STOP    ' BAD FETCH'
           IF(IFETCH(SPEC(20)).NE.0) STOP    ' BAD FETCH'
           IF(IFETCH(SPEC(1)).NE.0) STOP     ' BAD FETCH'
C
C          CREATE OR OPEN FILES FOR I/O
C
           IF(IENTER(JCHAN,SPEC(1),-1).LT.0) STOP ' ENTER FAIL'
           IF(LOOKUP(ICHAN,SPEC(16)).LT.0)STOP    'BAD LOOKUP1'
           IF(LOOKUP(IZCHAN,SPEC(20)).LT.0)STOP   ' BAD LOOKUP2'
C
C          READ INPUT FILES
C
           DO 50 J=1,60
           K=J-1
           IF (IREADW(240,IBUFF,K,ICHAN).LT.0)STOP ' BAD READ'
           IF (IREADW(240,IZBUFF,K,IZCHAN).LT.0)STOP' BAD READ'
```

```
C
C       CALCULATE ABSORBANCE
C
        DO 40 L=1,240
        IF((IZBUFF(L).GT.256).OR.(IZBUFF(L).LT.1))IZBUFF(L)=1
        IF((IBUFF(L).GT.256).OR.(IBUFF(L).LT.1)) IBUFF(L)=1
        X=(LOGT(IZBUFF(L))-LOGT(IBUFF(L)))*1000.
40      OBUFF(L)=IFIX(X)
C
C       WRITE OUTPUT FILE
C
50      IF (IWRITW(240,OBUFF,K,JCHAN).LT.0)STOP' BAD WRITE'
        CALL CLOSEC(ICHAN)
        CALL CLOSEC(IZCHAN)
        CALL CLOSEC(JCHAN)
        CALL IFREEC(ICHAN)
        CALL IFREEC(IZCHAN)
        CALL IFREEC(JCHAN)
        GO TO 15
        STOP
        END
```

```
C          ********** PROGRAM FCON **********
C
C
C          THIS PROGRAM READS IN TWO DATA FILES CORRESPONDING TO
C          I AND IZERO, IT THEN CONVERTS THEM TO AN OUTPUT FILE
C          IN ABSORBANCE UNITS
C
C
C
C
           INTEGER*2 IBUFF(240),IZBUFF(240), SPEC(39),OBUFF(240)
           REAL*4 EXT(2)
           DATA EXT/6RDATDAT,6RDATDAT/
15         WRITE(5,20)
20         FORMAT(' OUTPUT FILE=IFILE,IZFILE',//)
30         IF(ICSI(SPEC,EXT,,,0).NE.0)GO TO 30
C
C          ALLOCATE CHANNELS
C
           ICHAN=IGETC()
           IZCHAN=IGETC()
           JCHAN=IGETC()
C
C          FETCH DEVICE HANDLERS
C
           IF(IFETCH(SPEC(16)).NE.0) STOP      ' BAD FETCH'
           IF(IFETCH(SPEC(20)).NE.0) STOP      ' BAD FETCH'
           IF(IFETCH(SPEC(1)).NE.0) STOP       ' BAD FETCH'
C
C          CREATE OR OPEN FILES FOR I/O
C
           IF(IENTER(JCHAN,SPEC(1),-1).LT.0) STOP ' ENTER FAIL'
           IF(LOOKUP(ICHAN,SPEC(16)).LT.0)STOP     'BAD LOOKUP1'
           IF(LOOKUP(IZCHAN,SPEC(20)).LT.0)STOP    ' BAD LOOKUP2'
C
C          READ INPUT FILES
C
           DO 50 J=1,60
           K=J-1
           IF (IREADW(240,IBUFF,K,ICHAN).LT.0)STOP ' BAD READ'
           IF (IREADW(240,IZBUFF,K,IZCHAN).LT.0)STOP' BAD READ'
C
C          CALCULATE ABSORBANCE
C
           DO 40 L=1,240
           X=ALOG10(FLOAT(IZBUFF(L))/FLOAT(IBUFF(L)))
40         OBUFF(L)=IFIX(X*1000)
```

```
C
C
C       WRITE OUTPUT FILE
C
50      IF (IWRITW(240,OBUFF,K,JCHAN).LT.0)STOP' BAD WRITE'
        CALL CLOSEC(ICHAN)
        CALL CLOSEC(IZCHAN)
        CALL CLOSEC(JCHAN)
        CALL IFREEC(ICHAN)
        CALL IFREEC(IZCHAN)
        CALL IFREEC(JCHAN)
        GO TO 15
        STOP
        END
```

Program PSMO

PSMO is a FORTRAN language program which performs a 5-15 point two-dimensional smooth of an absorbance file generated by PCON or FCON. PSMO is effective for removal of noise spikes without changing the general shape of the absorbance contours. Subroutine SMOOTH which performs the actual smoothing function is based upon a third-degree polynomial least squares approximation algorithem (139). Source file listings of PSMO and SMOOTH are given in the following pages.

To operate:

    .RUN PSMO <CR>

    OUTPUT FILE = INPUT FILE

    *DEV:OFILE.EXT=DEV:IFILE.EXT <CR>

    *5 <CR>

    STOP --

```
C         ********** PROGRAM PSMO **********
C
C
C
C         THIS PROGRAM READS IN AN ABSORBANCE FILE
C         AND PERFORMS AN N POINT TWO-DIMENSIONAL
C         SMOOTH OF THE DATA
C
C
C
          INTEGER*2 SPEC(39),IBUFF(240),DATBUF(240,60)
          INTEGER*2 NBUFF(150),SBUFF(150),OBUFF(240)
          REAL*4 EXT(2)
          COMMON NBUFF,SBUFF
          DATA EXT/6RDATDAT,6RDATDAT/
          WRITE(5,120)
120       FORMAT(' =IFILE')
130       IF (ICSI(SPEC,EXT,,,0).NE.0)GO TO 130
C
C         ALLOCATE CHANNELS
C
          JCHAN=IGETC()
          ICHAN=IGETC()
C
C         FETCH DEVICE HANDLERS
C
          IF(IFETCH(SPEC(1)).NE.0) STOP    ' BAD FETCH'
          IF(IFETCH(SPEC(16)).NE.0)STOP    ' BAD FETCH'
C
C         CREATE OR OPEN FILES FOR I/O
C
          IF(IENTER(JCHAN,SPEC(1),-1).LT.0) STOP ' ENTER FAIL'
          IF(LOOKUP(ICHAN,SPEC(16)).LT.0)STOP ' BAD LOOKUP'
          READ (5,140) NPTS
140       FORMAT(I2)
          DO 170 J=1,60
          K=J-1
          IF (IREADW(240,IBUFF,K,ICHAN).LT.0)STOP   ' BAD READ'
          DO 170 N=1,4
          DO 170 M=1,60
170       DATBUF(K*4+N,M)=IBUFF((N-1)*60+M)
          DO 210 J=1,240
          DO 200 K=1,60
200       NBUFF(K)=DATBUF(J,K)
          CALL SMOOTH (60,NPTS)
          DO 210 K=1,60
210       DATBUF(J,K)=SBUFF(K)
          DO 330 J=1,60
```

```
         DO 300 K=1,240,2
300      NBUFF((K+1)/2)=DATBUF(K,J)
         CALL SMOOTH (60,NPTS)
         DO 310 K=1,240,2
310      DATBUF(K,J)=SBUFF((K+1)/2)
         DO 320 K=2,240,2
320      NBUFF(K/2)=DATBUF(K,J)
         CALL SMOOTH (60,NPTS)
         DO 330 K=2,240,2
330      DATBUFF(K,J)=SBUFF(K/2)
         DO 410 N=1,60
         DO 400 M=1,4
         DO 400 L=1,60
400      OBUFF((M-1)*60+L)=DATBUF((N-1)*4+M,L)
410      IF(IWRITW(240,OBUFF,N-1,JCHAN).LT.0)STOP     ' BAD WRITE'
         CALL CLOSEC(JCHAN)
         STOP
         END
```

```
C         ********** SUBROUTINE SMOOTH **********
C
C
C
C         THIS SUBROUTINE PERFORMS AN N POINT SMOOTH
C         WHEN CALLED BY PROGRAM PSMO
C
C
C
C
          SUBROUTINE SMOOTH (N,M)
          DIMENSION YY(150)
          INTEGER*2 DATA(150),D(150),Y(150),C(6,16)
          COMMON DATA,Y
          DATA C/
         1-3,-2,-21,-36,-11,-78,12,3,14,9,0,-13,
         217,6,39,44,9,42,12,7,54,69,16,87,
         3-3,6,59,84,21,122,0,3,54,89,24,147,
         40,-2,39,84,25,162,0,0,14,69,24,167,
         50,0,-21,44,21,162,0,0,0,9,16,147,
         60,0,0,-36,9,122,0,0,0,0,0,87,
         70,0,0,0,-11,42,0,0,0,0,0,-13,
         80,0,0,0,0,-78,35,21,231,429,143,1105/
          J=M/2
          L=J+1
          LL=J-1
          DO 1 K=1,J
    1     D(K)=0
          DO 2 K=1,J
    2     D(K+J+N)=0
          DO 3 K=1,N
    3     D(K+J)=DATA(K)
          DO 5 K=L,N+L
          YY(K-J)=0
          DO 4 KK=1,M
    4     YY(K-J)=YY(K-J)+FLOAT(C(LL,KK))*FLOAT(D(K-J+KK))
          YY(K-J)=YY(K-J)/C(LL,16)
    5     Y(K-J)=IFIX(YY(K-J))
          RETURN
          END
```

Programs PGRPH and PSPOT

PGRPH and PSPOT are FORTRAN language programs used to plot absorbance contours on an X-Y recorder or an oscilloscope, respectively. After entering the input file information, the operator must input the contour level to be plotted. This is entered as an integer number equal to absorbance times 10^3. Source file listings of PGRPH and PSPOT are given on the following pages.

To operate:

.RUN PGRPH <CR>

=IFILE.EXT

*DEV:IFILE.EXT <CR>

*100 <CR>

STOP --

.RUN PSPOT <CR>

=IFILE.EXT

*DEV:IFILE.EXT <CR>

*100 <CR>

STOP --

```
C          ********** PROGRAM PGRFH **********
C
C
C
C          THIS PROGRAM READS IN AN ABSORBANCE FILE
C          AND DISPLAYS ISOABSORBANCE CONTOURS ON AN
C          X-Y PLOTTER
C
C
C
           INTEGER*2 SPEC(39),IBUFF(240),DATBUF(240,60)
           REAL*4 EXT(2)
           DATA EXT/6RDATDAT,6RDATDAT/
           WRITE(5,120)
120        FORMAT(' =IFILE')
130        IF (ICSI(SPEC,EXT,,,0).NE.0)GO TO 130
C
C          ALLOCATE CHANNEL
C
           ICHAN=IGETC()
C
C          FETCH DEVICE HANDLERS
C
           IF(IFETCH(SPEC(16)).NE.0)STOP   ' BAD FETCH'
C
C          OPEN FILE FOR INPUT
C
           IF(LOOKUP(ICHAN,SPEC(16)).LT.0)STOP ' BAD LOOKUP'
           DO 170 J=1,60
           K=J-1
           IF (IREADW(240,IBUFF,K,ICHAN).LT.0)STOP   ' BAD READ'
           DO 170 N=1,4
           DO 170 M=1,60
170        DATBUF(K*4+N,M)=IBUFF((N-1)*60+M)
150        WRITE (5,160)
160        FORMAT(' CONTOUR LEVEL?')
           READ (5,180)LEVEL
180        FORMAT(I5)
           CALL REL (0,0)
           DO 300 J=1,240,2
           CALL LED(J,'I6')
           DO 200 K=1,58
           IZ=8
           IF((DATBUF(J,K).LT.LEVEL).AND.(DATBUF(J,K+1).GE.
          1LEVEL)) CALL MARK(J,K,IZ)
200        IF((DATBUF(J,K).GE.LEVEL).AND.(DATBUF(J,K+1).LT.
          1LEVEL)) CALL MARK(J,K,IZ)
```

```
      DO 300 K=1,58
      IZ=0
      JJ=J+1
      IF((DATBUF(JJ,K).LT.LEVEL).AND.(DATBUF(JJ,K+1).GE.
     1LEVEL)) CALL MARK(JJ,K,IZ)
300   IF((DATBUF(JJ,K).GE.LEVEL).AND.(DATBUF(JJ,K+1).LT.
     1LEVEL)) CALL MARK(JJ,K,IZ)
      GO TO 150
      STOP
      END
C
C
      SUBROUTINE MARK(IY,IX,IZ)
      CALL XYDAC(2048+IZ+16*IX,2048+3*IY)
      ICMF=0
      CALL SETR(4,0,500.,ICMF)
      CALL LWAIT(ICMF,0)
      CALL REL (0,1)
      ICMF=0
      CALL SETR(4,0,200.,ICMF)
      CALL LWAIT(ICMF,0)
      CALL REL (0,0)
      ICMF=0
      CALL SETR(4,0,100.,ICMF)
      CALL LWAIT(ICMF,0)
      RETURN
      END
C
C
      SUBROUTINE WAIT(A)
      ICMF=0
      CALL SETR(4,0,A,ICMF)
      CALL LWAIT(ICMF,0)
      RETURN
      END
```

```
C         ********** PROGRAM PSPOT **********
C
C
C
C         THIS PROGRAM READS IN AN ABSORBANCE FILE
C         AND DISPLAYS ISOABSORBANCE CONTOURS ON
C         AN OSCILLOSCOPE
C
C
C
          INTEGER*2 SPEC(39),IBUFF(240),DATBUF(240,60)
          REAL*4 EXT(2)
          DATA EXT/6RDATDAT,6RDATDAT/
          WRITE(5,120)
120       FORMAT(' =IFILE')
130       IF (ICSI(SPEC,EXT,,,0).NE.0)GO TO 130
C
C         ALLOCATE CHANNEL
C
          ICHAN=IGETC()
C
C         FETCH DEVICE HANDLERS
C
          IF(IFETCH(SPEC(16)).NE.0)STOP  ' BAD FETCH'
C
C         OPEN INPUT FILE
C
          IF(LOOKUP(ICHAN,SPEC(16)).LT.0)STOP ' BAD LOOKUP'
          DO 170 J=1,60
          K=J-1
          IF (IREADW(240,IBUFF,K,ICHAN).LT.0)STOP  ' BAD READ'
          DO 170 N=1,4
          DO 170 M=1,60
170       DATBUF(K*4+N,M)=IBUFF((N-1)*60+M)
150       WRITE (5,160)
160       FORMAT(' CONTOUR LEVEL?')
          READ (5,180)LEVEL
180       FORMAT(I5)
          CALL REL (0,1)
          CALL WAIT (10.)
          CALL XYDAC (2048,2048)
          CALL WAIT (10.)
          CALL REL (0,0)
          DO 800 N=2048,3016
          CALL XYDAC(N,2048)
800       CALL WAIT(1.)
          DO 810 N=2048,2768
          CALL XYDAC(3016,N)
810       CALL WAIT (1.)
          DO 820 N=1,963
```

```
            CALL XYDAC(3016-N,2768)
820     CALL WAIT (1.)
        DO 830 N=1,720
        CALL XYDAC(2048,2768-N)
830     CALL WAIT (1.)
        CALL REL (0,1)
        DO 300 J=1,240,2
        CALL LED(J,'I6')
        DO 200 K=1,58
        IZ=8
        CALL MARK (J,K,IZ)
        IF((DATBUF(J,K).LT.LEVEL).AND.(DATBUF(J,K+1).GE.
       1LEVEL)) CALL INTEN
200     IF((DATBUF(J,K).GE.LEVEL).AND.(DATBUF(J,K+1).LT.
       1LEVEL)) CALL INTEN
        DO 300 K=1,58
        IZ=0
        JJ=J+1
        CALL MARK(JJ,K,IZ)
        IF((DATBUF(JJ,K).LT.LEVEL).AND.(DATBUF(JJ,K+1).GE.
       1LEVEL)) CALL INTEN
300     IF((DATBUF(JJ,K).GE.LEVEL).AND.(DATBUF(JJ,K+1).LT.
       1LEVEL)) CALL INTEN
        CALL XYDAC (0,0)
        GO TO 150
        STOP
        END
C
C
        SUBROUTINE MARK(IY,IX,IZ)
        CALL XYDAC(2048+IZ+16*IX,2048+3*IY)
        RETURN
        END
C
C
        SUBROUTINE WAIT(A)
        ICMF=0
        CALL SETR(4,0,A,ICMF)
        CALL LWAIT(ICMF,0)
        RETURN
        END
C
C
        SUBROUTINE INTEN
        CALL REL(0,0)
        CALL WAIT(10.)
        CALL REL (0,1)
        CALL WAIT(10.)
        RETURN
        END
```

```
C        ********* PROGRAM FRAME **********
C
C
C        THIS PROGRAM IS USED IN CONJUNCTION WITH
C        PSPOT.   THE PURPOSE OF THIS PROGRAM IS TO
C        DISPLAY A CONTINIOUS FRAME TO THE OSCILLOSCOPE
C        SO THAT THE CONTROLS MAY BE SET TO GIVE
C        PROPER ASPECT RATIO AND CENTERING
C
C
         CALL REL (0,0)
700      DO 800 N=2048,3016
800      CALL XYDAC(N,2048)
         DO 810 N=2048,2768
810      CALL XYDAC(3016,N)
         DO 820 N=1,968
820      CALL XYDAC(3016-N,2768)
         DO 830 N=1,720
830      CALL XYDAC(2048,2768-N)
         GO TO 700
         STOP
         END
```